A DISTRIBUTED, PHYSICALLY-BASED, RAINFALL-RUNOFF MODEL INCORPORATING TOPOGRAPHY FOR REAL-TIME FLOOD FORECASTING

by

MARIZA C. CABRAL

RAFAEL L. BRAS

DAVID TARBOTON

DARA ENTEKHABI

RALPH M. PARSONS LABORATORY
HYDROLOGY AND WATER RESOURCE SYSTEMS

Report Number 332

October, 1990

BARKER ENGINEERING LIBRARY

MIT

DEPARTMENT

OF

CIVIL

ENGINEERING

●

SCHOOL OF ENGINEERING
MASSACHUSETTS INSTITUTE OF TECHNOLOGY
Cambridge, Massachusetts 02139

A DISTRIBUTED, PHYSICALLY–BASED, RAINFALL–RUNOFF MODEL INCORPORATING TOPOGRAPHY FOR REAL–TIME FLOOD FORECASTING

by

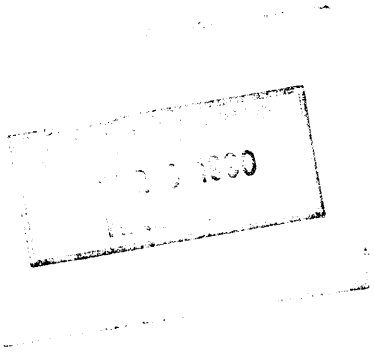Mariza C. Cabral
Rafael L. Bras
David Tarboton
Dara Entekhabi

RALPH M. PARSONS LABORATORY

HYDROLOGY AND WATER RESOURCE SYSTEMS

Report Number 332

OCTOBER 1990

ABSTRACT

We present a distributed, physically—based model of runoff generation in a catchment, for operational use in flood forecasting. The model accounts for both the infiltration—excess and saturation—excess mechanisms of runoff production, and for lateral subsurface flows. The effect of local terrain slope on subsurface flows and the development of areas of saturated soil is accounted for. The model uses spatial discretization into rectangular elements which correspond to the grid of a Digital Elevation Map. Each basin element consists of a soil column in which hydraulic conductivity decreases with depth, in the form of an exponential function. Spatial discretization allows for distributed terrain slope, soil parameters, moisture conditions, and rainfall inputs. Time discretization allows for consideration of time—variable rainfall rates.

The model uses the kinematic approximation of infiltration and subsurface flows, which are assumed to occur only within the porous soil matrix. The kinematic model of infiltration is used to show how decreasing conductivity with depth may result in the development of a zone of perched saturation during a rainstorm, and that the flow in the perched saturated zone is diverted laterally if the terrain is inclined. A simplified computational procedure is introduced that allows flow transfer among elements. Inter—element flow transfers are used to predict the position of the permanent water—table in each element at the time of initiation of the rainfall event and the extent of the area of saturated soils. Moisture transfer between elements during the storm is also considered. The model is extended to consider anisotropic soils, and we show that higher lateral than vertical conductivity results in increased lateral diversion of flow.

The model was applied to the Sieve catchment in Italy and used to reproduce hydrographs for 12 recorded rainstorms. Given that pre—storm baseflow was not available for any of the 12 storms, three different water—table positions were considered for each storm, low average and high, corresponding to steady—state equilibrium with the baseflow values that have a 90% and 10% probability of being exceeded in the month in question. The observed hydrographs for the various storms were, generally, in the area comprised between the "dry" and "wet" predicted hydrographs, or did not fall far from this area. Given the scarcity of data available for the Sieve, we consider model predictions to be quite encouraging.

3

ACKNOWLEDGMENTS

Table of Contents

List of Figures

11

13

14

probability of 50%) in the month of December,
R_i = 0.0300 mm/hr. 152

16

18

List of Tables

Chapter 1

INTRODUCTION

1.A. STATEMENT OF THE PROBLEM

The history of physically-based modeling of runoff generation, no more than 30 years old, has been characterized by an enormously wide range of approaches and levels of complexity. While part of the explanation for this variety lies in the multiplicity and complexity of the physical processes themselves, much of the history of these models has been shaped by the gradual development of computational capabilities and data sources, and the continuous attempt to make the best possible use of the new resources.

One of the major difficulties in understanding and quantifying runoff generation in river basins stems from the presence of spatial variability in topography, geology, soil type, vegetation, etc., and in water fluxes, such as rainfall, infiltration and evapotranspiration. The accelerated growth of remotely-sensed distributed data, including satellite readings of terrain topography, soil type, soil use, vegetational coverage, geology, soil moisture status, and radar estimates of rainfall rates, brings enormous promise to hydrologic science and runoff forecasting in particular.

Such distributed data are rapidly becoming widespread and easily available over vast regions of the World. In particular, Digital Elevation Maps (DEMs) are already available for most of the U.S. territory, and other regions of the World. Weather radar provides high temporal and spatial resolution estimates of rainfall-rates and benefits rainfall prediction enormously through detection of storm-system development. Near-full coverage of the U.S. and Western Europe by weather radar networks is under implementation. Therefore, there is a challenge to develop new model formulations which are capable of making best use of the distributed data available.

The availability of Digital Elevation Maps (DEMs) have led to the generation of algorithms for estimation of topographic variables such as terrain slopes and exposure, and to more involved ones aiming at the derivation of river-channel networks from a number of assumptions (e. g. Tarboton, 1989). Through terrain slopes, the runoff model is able to incorporate the effects of topography, which have long been recognized as important in runoff generation. Computer-derived channel networks have revealed a generally good correspondence with map-digitized networks, and represent a convenient alternative to them for use in distributed rainfall-runoff models.

Weather radar offers unprecedented perspectives to flood forecasting, in two major ways. First, it provides rainfall rate estimates with high spatial and temporal resolutions. While such estimates may not have the precision of raingage point measurements, they provide the information on spatial distribution of rainfall that is crucial to accurate streamflow forecasting. Radar makes millions of measurements per minute with a resolution in the order of one kilometer, and its readings

are immediately available. Second, rainfall prediction benefits enormously from radar data. Readings at successive time steps reveal storm-system development and movement. The more advanced *Doppler* technology radar offers additional advantages as a result of its ability to detect direction and speed of object movement in a single reading. A color-code map of air-mass directions and speeds can be produced on a computer screen in real time, to be promptly interpreted. The weather forecaster can thus detect rainstorm development and movement, and identify the particular color patterns that are signatures of tornado development.

Although physical arguments favour an understanding of hillslope hydrology on the basis of flow strips, remotely sensed data are generally available for grid squares. Both DEMs and radar estimates of rainfall are made available for grid squares. Growth of Geographic Information Systems data bases also promise to provide soil-type maps in digital form, from which parameter values, such of saturated hydraulic conductivity, may be derived. Therefore, there seems to be an advantage to developing rainfall-runoff models structured to make use of distributed data provided for grid squares. From a computational point of view, spatial discretization into grid squares rather than flow strips or irregular elements facilitates element reference through coordinate values, algorithm structure, and data storage in a simple matrix form. Also, algorithms written for square elements are easily transferrable for application in different catchments.

We present a model framework that incorporates a variety of distributed data characterizing terrain morphology, soil parameters, and rainfall inputs, in the form of grid squares. Terrain morphology is

obtained from DEMs, soil parameters are obtained from digitized maps of soil type, and rainfall rate may be provided by radar readings or by a network of telemetering raingages. The model attempts to describe the various physical processes of runoff generation on the hillslope that are currently accepted, namely saturation-excess runoff, infiltration-excess runoff, interflow, and return flow.

I.B REVIEW OF LITERATURE

A few models have been presented which seek full numerical solutions to the governing equations of subsurface and overland flow. While such models have contributed to our understanding of runoff production processes at the hillslope scale, their data and computational requirements precludes their application at the catchment scale. One of the most complete of such models is that of Freeze (1971), which simulates transient subsurface flow in an integrated saturated-unsaturated flow system. The governing equations are (1) the two-dimensional equation for Darcian flow and (2) the Saint-Venant equation for overland flow. The Darcian flow equation uses values of conductivity and hydraulic potential measured in the field. Soil conditions of heterogeneity and anisotropy may be considered by the model. Both infiltration-excess (Hortonian) and saturation-excess runoff generation are predicted by this model. The model admits any generalized configuration of all pertinent boundary conditions, namely flow divides, position of impermeable bedrock, stream outflow and rainfall input. This model has been applied to a hillslope flow

26

strip in the Reynolds Creek Watershed, Idaho (Stephenson, G.R. and Freeze, R.A., 1974). Model predictions of water-table position, hydraulic head patterns, and generated runoff compared well with field measurements on a hillslope flow strip, giving support to the model's construction. However, and in spite of the small scale of application and the large data collection efforts, the model's intense requirements for field data restricted the use of some of its capabilities such as consideration of soil anisotropy, hysteresis, and of streamflow boundary conditions.

Model application at the catchment scale requires introduction of approximations to reduce data and computational requirements. A generalized approximation, supported by field evidence, considers unsaturated subsurface flows to be vertical and saturated flows to be parallel to the terrain surface. Saturated flows are usually treated as a single layer, which reduces the problem to a series of coupled one-dimensional equations (of similar form to the Saint-Venant equations for overland flow). One model that considers such simplifications is the "Système Hydrologique Européen (SHE)" (Beven, K. *et al.*, 1980; Abbot, M.B. *et al.*, 1986a,b; Bathurst, 1986a,b), developed through the combined efforts of the Institute of Hydrology (U.K.), the SOGREAH, and the Danish Hydraulic Institute. Some models that include these simplifications use the kinematic approximation to model downslope saturated flow. Examples are the model of Beven (1981, 1982) and the model of Hurley and Pantelis (1985).

Some runoff models emphasize saturation-excess over infiltration-excess runoff generation. In predicting saturation-excess runoff, the position of the water-table is of concern. Several researchers have demonstrated that water-table position is strongly associated with terrain

morphology. Aside from any effect due to random heterogeneity of soil properties, there is a general tendency for lateral increase in moisture content in the downslope direction that results from the increasing size of the upstream hillslope area contributing subsurface flows, especially in areas of convergent topography. If the upstream drained area is sufficiently large, the lower parts of the hillslopes may be completely saturated, or water-logged. The significance of these saturated zones is well appreciated in disciplines that include engineering, soil conservation, forestry, agriculture, and hydrology because of their enormous effect on soil strength, erosion, secondary salinization, and storm runoff. Field studies that have validated the importance of topography in determining the position and extent of saturated areas include the pioneering work by Dunne and Black (1970a,b), and the studies by Anderson and Burt (1977, 1978) and Beven (1978).

Given the association between topography and water-table position, many models that emphasize saturation-excess runoff generation account for topographic variables explicitly. Dunne and Black (1970) were the first to demonstrate how areas of saturated soil occur most readily in convergent, concave areas, and that these areas expand and contract during rain storms. Similar patterns have been demonstrated for subsurface flows by Anderson and Burt (1978), although Anderson and Kneale (1982) have shown that in areas of low slope there is not such a close relationship between saturation and surface morphology. Engman and Rogowski (1974) combined infiltration equations with mapped soil properties to forecast saturated areas. Troendle (Troendle, 1985; Hewlett and Troendle, 1975) has developed a series of related models which use a two-dimensional numerical solution for saturated and unsaturated water

movement along a flow strip. Where surface elements near the slope base become saturated, the saturated area is added to the effective channel area receiving direct precipitation and the remainder of the hillside upslope is redivided into elements, with their highest density close to the edge of the saturated area. The model is designed to give its most accurate forecasts for the margins of the saturated area, which then generates overland flow. The model assumes that no Hortonian overland flow occurs. The model gave good agreement for a 0.38 Km^2 mountain catchment in West Virginia. Application to the 0.24 Km^2 Whitefall watershed near Athens, Georgia was less successful.

The generalized unavailability of field data with the detail required for physically-based modeling has generated strong motivation for development of conceptual models. Two conceptual models have been proposed which consider catchment morphology to predict areas of saturated soils. A central assumption of these models is the hypothetical condition of equilibrium of the groundwater storage with recharge. One model is TOPMODEL of Beven *et al.* (Beven and Kirkby, 1979; Beven and Wood, 1983; Beven et al., 1984; Horberger et al., 1985), which considers an exponential decrease of soil hydraulic conductivity with depth, from which results an exponential form for the relation between transmissivity and water table depth. The model has been extended by Beven (1986a,b) to allow distributed soil parameters and to include prediction of infiltration-excess runoff. TOPMODEL was able to give moderately good forecasts over both storm and inter-storm periods in most applications. The other model, by O'Loughlin and Moore (O'Loughlin, 1981, 1986; Moore et al., 1986) can consider arbitrary variations of hydraulic conductivity with depth. Each of these two models involves a *topographic index* for a large number of points

in the catchment, and the two indices are basically very similar to each other.

The topographic index introduced in TOPMODEL, $\ln(a/\tan(\beta))$, where a is the area drained per unit contour length and $\tan(\beta)$ is the slope of the ground surface at the location, has been found by Beven and Kirkby to compare favorably with observed patterns of surface saturation. Beven and Kirkby developed a hydrological forecasting model combining a dynamic contributing area model based on $\ln(a/\tan(\beta))$, the channel network topology, and a simple lumped parameter basin routing model. The model parameters were physically based in the sense that they may be determined directly by measurement. Using only estimated and measured parameter values the model made satisfactory predictions of catchment response.

O'Loughlin (1981) derived criteria for the existence of saturated areas on draining hillslopes in natural catchments, based on the correlation between seepage face and contributing area. These criteria were expressed in terms of a topographic index h(x), which turns out to be almost identical to $\ln(a/\tan(\beta))$. Based on the analysis of hillslopes of different shapes (parallel, converging, and diverging), O'Loughlin showed that the contributing areas are largest in the convergent zones and smallest in the divergent zones. Also, the uphill boundary of the contributing area on a convergent hillslope was shown to be much more stable than that on a plane or divergent hillslope. This means that in drier conditions, the seepage face on a plane hillslope may shrink back to the stream edge while on a convergent slope the contributing area tends to persist. Earlier, Kirkby and Chorley (1967) had shown theoretically that the largest contributions to runoff came from hillslopes which are concave

in section and convergent in plan. These predictions have been qualitatively confirmed by the observations of Dunne (1978) and others in the field.

1.C MODEL CONCEPTUALIZATION

We present a model of runoff production for real-time streamflow forecasting which considers spatially distributed soil parameters, terrain slope, and rainfall inputs. The model is physically based and accounts for both infiltration-excess (Horton type) and saturation-excess (Dunne type) mechanisms of runoff production. The kinematic approximation is used to model subsurface flows, and to predict infiltration and lateral groundwater flows. The effect of local terrain slope upon lateral subsurface flows is accounted for. Local slope is obtained from a Digital Elevation Map (DEM) of the catchment, which is provided in the form of elevation values taken at regularly-spaced points of a rectangular grid. All runoff generated is routed over the hillslope to a channel and along the channel network to the outlet, and contributes to the predicted hydrograph. Routing considers two velocity parameters that are spatially uniform and constant in time; a velocity of flow travel over hillslopes, and a velocity of travel in the channel network.

To account for spatial variability of parameters and variables, the basin is subdivided into identical rectangular elements, or *pixels* (contraction of the term *picture element*). The use of rectangular elements has considerable advantages regarding computational efficiency and data

31

storage. The elements are taken to correspond to the DEM grid. The grid size of the DEM is generally comparable to the resolution of digitized soil maps and of radar rainfall measurements, so that distributed information is preserved by this element size. Terrain slope for each element is obtained from the DEM. The network of stream channels may be digitized from a terrain map or may be approximated by a network estimated automatically from the DEM, through well established algorithms (Tarboton, 1989). Automatically-generated river networks have in general compared favorably with mapped blue lines.

Figure 1.1 represents an example of the spatial discretization of a river basin corresponding to a DEM in a rectangular (in this example it is square) grid.

I.D OUTLINE

This work is organized into four main chapters, followed by a concluding chapter and an appendix including the computer codes used.

Chapter 2 describes the model of infiltration, which is based in the kinematic approximation. The chapter is divided into three sections. Section 2.A provides a review of the kinematic model of infiltration in a homogeneous, isotropic soil, following the presentation by Charbeneau (1984). Section 2.B presents an analysis of kinematic infiltration in a vertically heterogeneous sloped soil, where hydraulic conductivity decreases exponentially with depth. Section 2.C introduces a conceptual
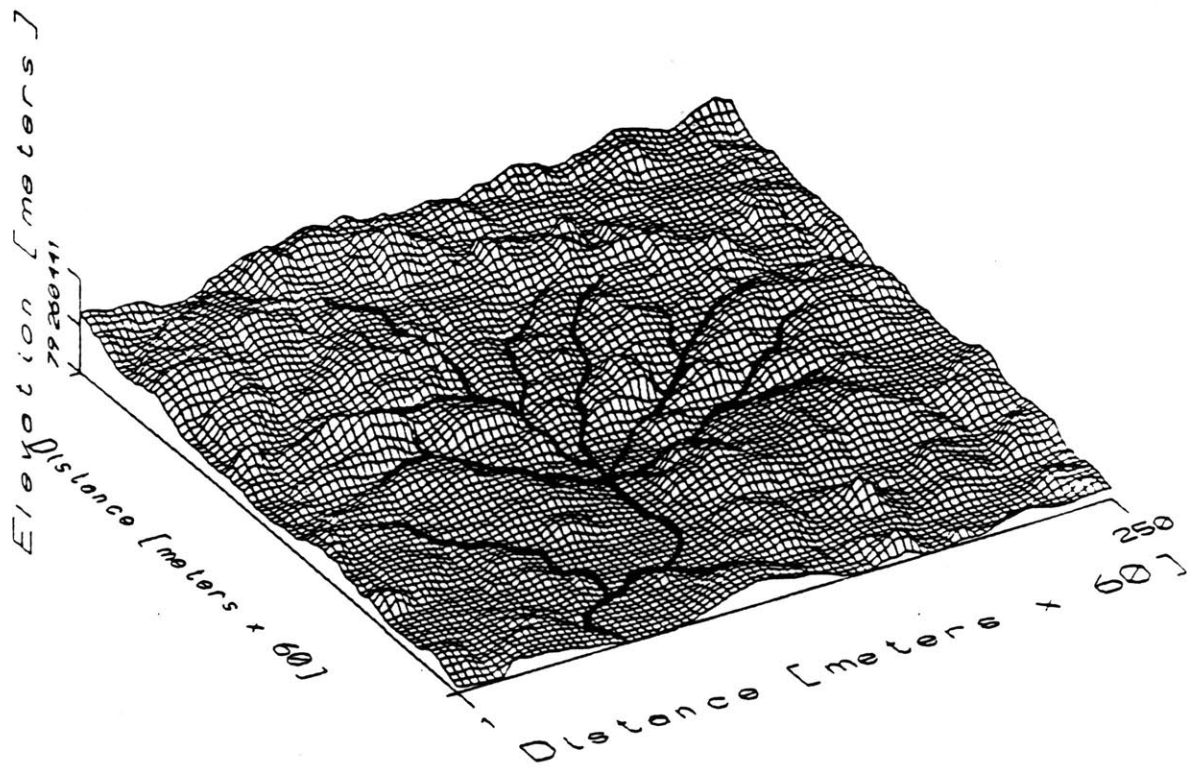
FIGURE 1.1: Discretization of a river basin into rectangular elements corresponding to the pixels of the DEM.

approximation to the a complex moisture profile which allows computational simplicity in the treatment of variable rainfall rates.

Chapter 3 describes the conceptualization of the rainfall-runoff model at the basin scale. The chapter is divided into six sections. Section 3.A discusses spatial discretization and describes computations in one element. Section 3.B discusses the computational procedure that accomplishes element coupling through lateral flows. Section 3.D treats model initialization with an estimated water-table and unsaturated moisture profile above the water-table. Section 3.E describes the flow routing computation. Finally, Section 3.F investigates model sensitivity to soil parameters, initial conditions and rainfall inputs.

Chapter 4 presents model predictions for a series of observed rainfall events in the Arno River basin in Tuscany, Italy.

Chapter 5 summarizes the important conclusions, discusses model limitations and provides suggestions for future work.

Chapter 2

MODEL OF INFILTRATION

In this Chapter we present the model of infiltration which will be used in the rainfall-runoff model. The infiltration model is based on the kinematic theory of infiltration which provides a simplified description of gravity-dominated moisture flow. The model incorporates additional approximations in the treatment of time-varying rainfall rates.

Kinematic infiltration has been studied by various researchers dealing with a homogeneous, isotropic soil (v.g., Smith and Hebbert, 1983, and Charbeneau, 1984). In Section 2.A we review the assumptions of the kinematic model of infiltration and the derivation of an equation of evolution of the depth of the wetting front in a homogeneous, isotropic soil. Most natural soils, however, have decreasing permeability with depth. In Section 2.B we apply the kinematic assumption to infiltration in a vertically heterogeneous soil where conductivity decreases exponentially with depth. We consider both unsaturated and saturated infiltration on a hillslope with areally uniform conditions of soil type, slope, and rainfall rate. Spatial uniformity permits the use of a one-dimensional continuity equation. The analysis clarifies the influence of slope, soil parameters, and rainfall rate on infiltration and the generation of infiltration-excess runoff and interflow. In Section 2.C, a conceptual approximation to the soil moisture profile is introduced that allows for computational simplicity in the treatment of time-varying rainfall rates.

2.A THEORY OF THE KINEMATIC MODEL OF INFILTRATION

This section presents the kinematic theory of infiltration for one-dimensional vertical flow in a homogeneous, isotropic soil. The theory of kinematic waves was developed by Lighthill and Whitham (1955) for estimating the propagation of flood waves. Wave motion follows both kinematic and dynamic laws, and its complete description therefore includes both advective and dissipative terms. The kinematic model of wave motion considers only the advective component of flow, neglecting the second-order spatial derivatives that describe dispersive transport. In an analogous fashion, the kinematic model of infiltration relies on reducing the moisture flow equation to its gravitational component, i.e., the pore pressure gradient component of flow is neglected.

The familiar Darcy's equation for one-dimensional, vertical unsaturated flow (where z is positive downward), is:

$$q_z(\theta) = K(\theta) \cdot \left(1 - \frac{\partial \psi(\theta)}{\partial z} \right) \tag{2.1}$$

where θ is the volumetric soil moisture content;
$q_z(\theta)$ is the downward unsaturated flow;
$K(\theta)$ is the *unsaturated hydraulic conductivity*;
and $\psi(\theta)$ is the pore pressure.

The first term in the parenthesis represents the gradient of positional, or gravitational potential. The second term in the parenthesis is the gradient of pore pressure. The gravitational flux component, $K(\theta)$,

depends only on moisture content, and is the advective term in the equation. The flux induced by the pressure gradient or *capillary* flux, $-K(\theta) \cdot (\partial \psi(\theta)/\partial z)$, depends not only on mass concentration but also on its spatial gradient, and is the diffusive term.

The kinematic model reduces Equation (2.1) to

$$q_z(\theta) = K(\theta) \tag{2.2}$$

The continuity equation for one-dimensional vertical flow is

$$\frac{\partial \theta}{\partial t} + \frac{\partial q_z(\theta)}{\partial z} = 0 \tag{2.3}$$

Substitution of the Kinematic Flow Equation (2.2) in the Continuity Equation (2.3) leads to

$$\frac{\partial \theta}{\partial t} + \frac{dK(\theta)}{d\theta} \cdot \frac{\partial \theta}{\partial z} = 0 \tag{2.4}$$

Solving (2.4) for $dK(\theta)/d\theta$ with θ constant we obtain

$$\frac{dK(\theta)}{d\theta} = \frac{\partial \theta}{\partial t} \cdot \frac{\partial z}{\partial \theta} = \frac{dz}{dt} \bigg|_{\theta \text{ constant}} \tag{2.5}$$

Provided that $\theta(z,t)$ is continuous throughout the z-t space, Equation (2.5) states that the *mobility* of a point of constant θ in the soil moisture profile is given by $dK(\theta)/d\theta$. Integrating (2.5) yields the expression which is the basis of the method of *characteristic solutions* to (2.3),

$$z(\theta) = \frac{dK(\theta)}{d\theta} \cdot (t - \tau) \qquad\qquad (2.6)$$

where τ is the time of initiation of rainfall

Most empirical models of the K-θ relation are either exponential or power-law relations with the exponent greater than or equal to 3.0. Thus, $dK(\theta)/d\theta$ increases with θ, i.e. the mobility is greater for higher θ values. This leads to the important conclusion that because moisture content decreases with depth at the wetting front, a kinematic front steepens with time. Reversely, in a "drainage wave" the moisture content increases with depth, and the profile is self-spreading.

The steepening nature of the kinematic wetting front eventually leads to a discontinuity in the moisture profile. Charbeneau (1984), following Whitham (1974), derives an expression for the depth at which the moisture gradient becomes infinite.

The moisture profile of the true front is continuous with depth. The sharpening tendency of the kinematic component of flow is counteracted by the spreading effect of the diffusive component. The equilibrium shape of the front depends on the importance of diffusion in the particular soil. Figure 2.1 represents a true wetting front and its kinematic approximation.

Equation (2.4) does not apply to a discontinuous profile since neither $\partial\theta/\partial t$ nor $\partial\theta/\partial z$ are continuous at the front. Instead, we will derive an expression for the advance of the kinematic front based on continuity considerations. From continuity, the sharp kinematic wave must have the
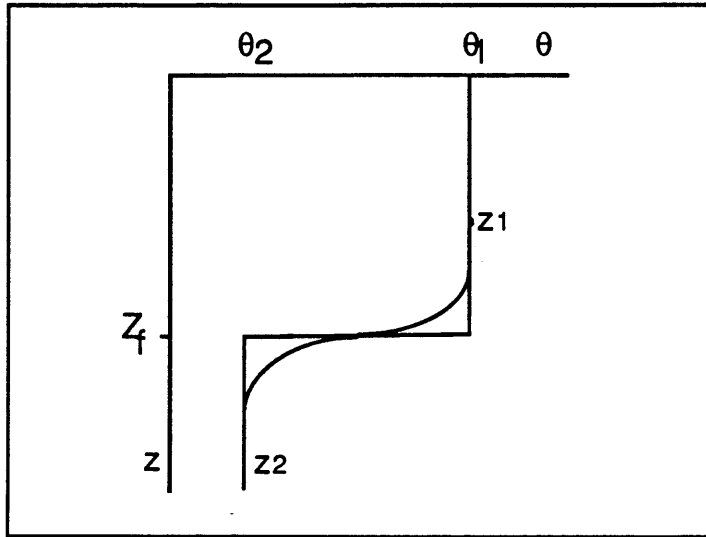
FIGURE 2.1: Wetting fronts as defined by the full model and the kinematic model of infiltration.

same moisture volume as the smooth wave which it approximates. Therefore, the depth of the kinematic front, Z_f, must satisfy

$$\int_{z_1}^{z_2} \theta \cdot dz = (z_2 - Z_f) \cdot \theta_2 + (Z_f - z_1) \cdot \theta_1 \qquad (2.7)$$

Integrating the Continuity Equation (2.3) over depth, we obtain

$$\frac{d}{dt}\int_{z_1}^{z_2} \theta \cdot dz + \frac{\partial}{\partial z}\int_{z_1}^{z_2} q_z(\theta) \cdot dz = 0 \qquad (2.8)$$

Substituting the kinematic flow Equation (2.2),

$$\frac{d}{dt}\int_{z_1}^{z_2} \theta \cdot dz + K(\theta) \Big|_{z_1}^{z_2} = 0 \qquad (2.9)$$

Replacing the integral in (2.9) by (2.7) and differentiating with respect to time we obtain

$$\frac{dZ_f}{dt} = \frac{K(\theta_1) - K(\theta_2)}{\theta_1 - \theta_2} \qquad (2.10)$$

Integration of (2.10) yields

$$Z_f = \left(\frac{K(\theta_1) - K(\theta_2)}{\theta_1 - \theta_2}\right) \cdot (t - \tau) \qquad (2.11)$$

where τ is the time of initiation of rainfall.

Note that given the equal volume of water in the true front and the kinematic front (Equation (2.7)), the rate of advance of the true wetting front equals that of the kinematic front, given in (2.9). For our purposes, the mean position of the wetting front, not its shape, is of concern.

2.B KINEMATIC INFILTRATION IN A VERTICALLY HETEROGENEOUS SLOPED SOIL

In this section, we consider infiltration in an isotropic hillslope soil where saturated hydraulic conductivity decreases exponentially with depth, under areally uniform soil parameters and slope. The analysis is extended to anisotropic soils in Appendix A. Rainfall rate, R, is considered to be constant in space and time. The coordinate directions and angles required by our analysis are defined in Figure-caption 2.2.

i) Soil parameterization and moisture initialization

Saturated hydraulic conductivity decreases exponentially with depth measured from the surface in the vertical direction i.e., in the z direction.
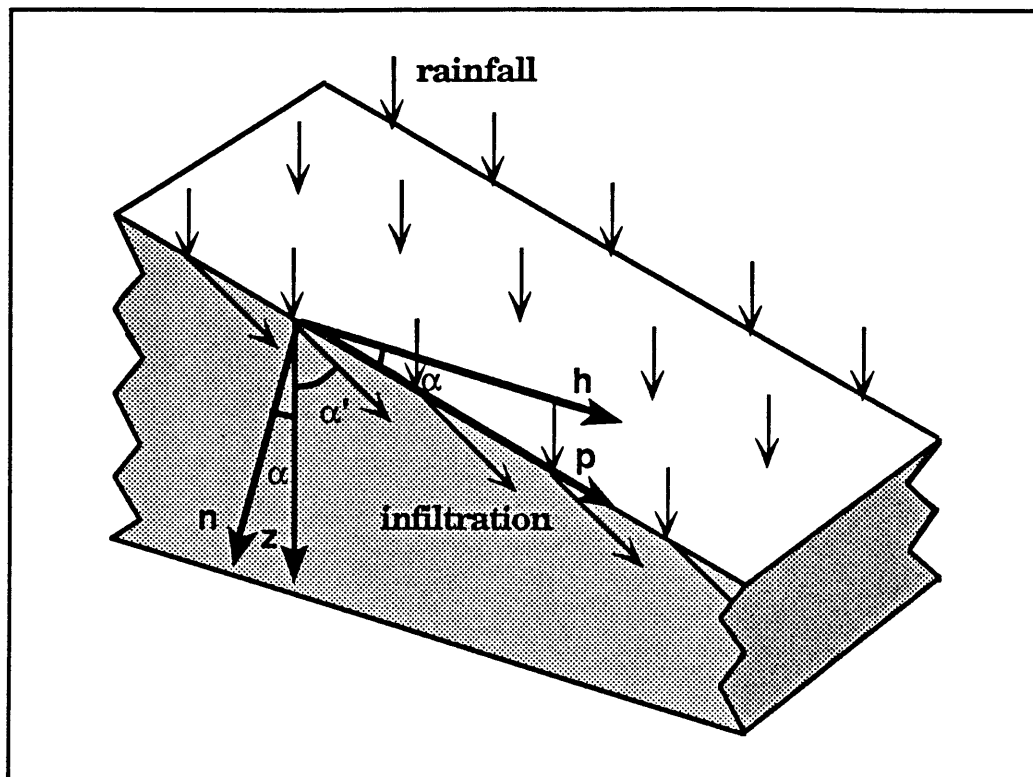
FIGURE 2.2: Representation of the coordinate directions on a hillslope of constant slope, $\tan(\alpha)$. Axis p is parallel to the hillslope surface and points in the direction of maximum slope. Axis n is normal to the hillslope surface. Axis h is the projection of axis p on the horizontal plane. Axis z is in the vertical direction. Infiltration may be at an angle α' with respect to the vertical direction, as represented.

$$K_s(z) = K_0 \cdot e^{-f \cdot z} \tag{2.12}$$

where $K_s(z)$ is the saturated hydraulic conductivity at depth z;
K_0 is the surface saturated hydraulic conductivity;
and f is a parameter with dimensions L^{-1}.

The Brooks-Corey (Brooks and Corey, 1964) parameterization of unsaturated hydraulic conductivity will be used,

$$K(\theta) = K_s \cdot \left(\frac{\theta - \theta_r}{\theta_s - \theta_r} \right)^\varepsilon \tag{2.13}$$

where $K(\theta)$ is the hydraulic conductivity at moisture content θ;
K_s is the saturated hydraulic conductivity;
θ_s is the saturated moisture content;
θ_r is the residual moisture content, defined as the value below which moisture cannot be extracted by capillary forces; and
ε is a pore size distribution index.

A correlation normally exists between each of the parameters θ_r, θ_s, and ε and the saturated hydraulic conductivity. For saturated conductivity varying with depth, these parameters should correspondingly be functions of depth. Not knowing those functions, and for simplicity, we consider parameters θ_r, θ_s, and ε to be constant with depth.

Substituting (2.12) into (2.13), we obtain

$$K(\theta,z) = K_0 \cdot e^{-f \cdot z} \cdot \left(\frac{\theta - \theta_r}{\theta_s - \theta_r} \right)^\varepsilon \tag{2.14}$$

It is assumed that prior to the initiation of rainfall the soil had a constant recharge rate, R_i. The initial moisture profile will be computed

43

from this infiltration rate. Estimation of R_i will be dealt with in Section 3.C.

ii) Unsaturated infiltration

If the rainfall rate is less than the surface saturated conductivity (i.e., $R<K_0$), then infiltration occurs initially under unsaturated conditions. For the kinematic approximation, flow is in the direction of the gravitational potential gradient i.e., it is vertical. Therefore, we have for unsaturated infiltration, $q_z(\theta,z) = K_z(\theta,z) = R$ (for $z < Z_f$). However, soil parameterization (2.12) implies that any rainfall rate R below the surface saturated conductivity has a corresponding critical depth, $Z^*(R)$, in the soil profile for which the saturated conductivity equals R, i.e.,

$$z< Z^* ; \qquad K_s(z) > R$$
$$z = Z^* ; \qquad K_s(z) = R$$
$$z > Z^* ; \qquad K_s(z) < R$$

Letting $z=Z^*(R)$ in (2.12) and solving for $Z^*(R)$, we obtain

$$Z^*(R) = \frac{1}{f} \cdot \ln\left(\frac{K_0}{R}\right) \qquad (2.15)$$

44

The wetting front is unsaturated for $Z_f < Z^*(R)$ and saturated for $Z_f > Z^*(R)$. Saturated infiltration is the subject of section iii). Substituting $K(\theta,z) = R$ into (2.14) and solving for $\theta(R,z)$, we obtain

$$\theta(R,z) = \left(\frac{R}{K_0}\right)^{\frac{1}{\epsilon}} \cdot e^{\frac{f}{\epsilon} \cdot z} \cdot (\theta_s - \theta_r) + \theta_r \quad , \text{ for } z < Z_f \text{ with } Z_f < Z^*(R) \qquad (2.16)$$

Equation (2.16) shows that the moisture content above the wetting front increases exponentially with depth. Figure 2.3 represents moisture profiles for different rainfall rates.

Since unsaturated flow is vertical, the one-dimensional flow continuity equation applies. The derivation of the expression of evolution for Z_f is analogous to that for unsaturated flow in a homogeneous soil presented in 2.A. Integrating (2.3) in z ,

$$\frac{d}{dt}\int_{z_1}^{z_2} \theta \cdot dz \; + q_z \left. (\theta,z) \right|_{z_1}^{z_2} = 0$$

or

$$\frac{d}{dt}\int_{z_1}^{z_2} \theta \cdot dz \; + R - R_i = 0 \qquad (2.17)$$

Through substitution of (2.16), the integral of moisture in (2.17) is given by
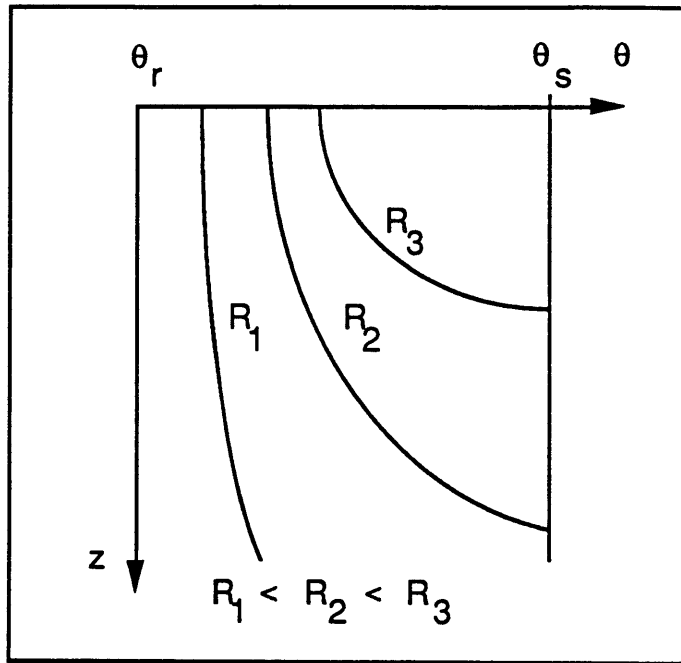
FIGURE 2.3: Moisture profiles for various rainfall rates lower than the soil surface saturated conductivity, for a soil where hydraulic conductivity decreases exponentially with depth.

$$\int_{z_1}^{z_2} \theta \cdot dz = \int_{z_1}^{Z_f} \theta(R,z) \cdot dz + \int_{Z_f}^{z_2} \theta(R_i,z) \cdot dz$$

$$= \left(\frac{R}{K_0}\right)^{\frac{1}{\varepsilon}} \cdot (\theta_s - \theta_r) \cdot \left(\frac{\varepsilon}{f}\right) \cdot (e^{\frac{f}{\varepsilon} \cdot Z_f} - e^{\frac{f}{\varepsilon} \cdot z_1}) + \theta_r \cdot (Z_f - z_1) +$$

$$\left(\frac{R_i}{K_0}\right)^{\frac{1}{\varepsilon}} \cdot (\theta_s - \theta_r) \cdot \left(\frac{\varepsilon}{f}\right) \cdot (e^{\frac{f}{\varepsilon} \cdot z_2} - e^{\frac{f}{\varepsilon} \cdot Z_f}) + \theta_r \cdot (Z_f - z_1) \qquad (2.18)$$

Differentiation of (2.18) with respect to time yields the first term in (2.17),

$$\frac{d}{dt} \int_{z_1}^{z_2} \theta \cdot dz = \frac{dZ_f}{dt} \cdot \left[\left(\frac{R}{K_0}\right)^{\frac{1}{\varepsilon}} \cdot (\theta_s - \theta_r) \cdot e^{\frac{f}{\varepsilon} \cdot Z_f} + \theta_r \right] -$$

$$\frac{dZ_f}{dt} \cdot \left[\left(\frac{R_i}{K_0}\right)^{\frac{1}{\varepsilon}} \cdot (\theta_s - \theta_r) \cdot e^{\frac{f}{\varepsilon} \cdot Z_f} + \theta_r \right]$$

$$= \frac{dZ_f}{dt} \cdot [\theta(R,Z_f) - \theta(R_i,Z_f)] \qquad (2.19)$$

Substituting (2.19) into (2.17) and solving for dZ_f/dt yields

$$\frac{dZ_f}{dt} = \frac{R - R_i}{\theta(R,Z_f) - \theta(R_i,Z_f)} \qquad (2.20)$$

47

iii) Saturated infiltration

The wetting front is saturated in two cases; 1) when the rainfall rate is higher than the surface saturated conductivity, or 2) when the wetting front has penetrated beyond the critical depth $Z^*(R)$. In the first case, the entire wetted soil (i.e., from the surface to Z_f) is saturated. In the second case, as the front reaches $Z^*(R)$, discharge can only be less than recharge from above, and moisture progressively accumulates above the wetting front. A zone of perched saturation develops and grows upward from $Z^*(R)$, as well as downward as the front progresses. Here we introduce a new variable, Z_t, defined as Z_f minus the depth of the zone of perched saturation. If there is a zone of perched saturation, this definition corresponds to the vertical distance from the top of the zone of saturation to the soil surface. If the whole wetted soil is unsaturated ($Z_f < Z^*(R)$), then Z_t equals Z_f. An equation of evolution for Z_t, as well as for Z_f, will be derived below. Figure 2.4 represents the progression of the wetting front in time, showing the development of a zone of saturation, and the upward evolution of Z_t.

The flow *at the wetting front* is in the direction of the gravitational potential gradient, i.e. it is vertical. Neglecting pressure gradients we have,

$$q_z(Z_f) = K_s(Z_f) = K_0 \cdot e^{-f Z_f} \quad , \text{ for } Z_f \geq Z^*(R) \qquad (2.21)$$

Above the wetting front ($z < Z_f$), the saturated conductivity is higher than at the wetting front, but flow is constrained by continuity. Thus, the
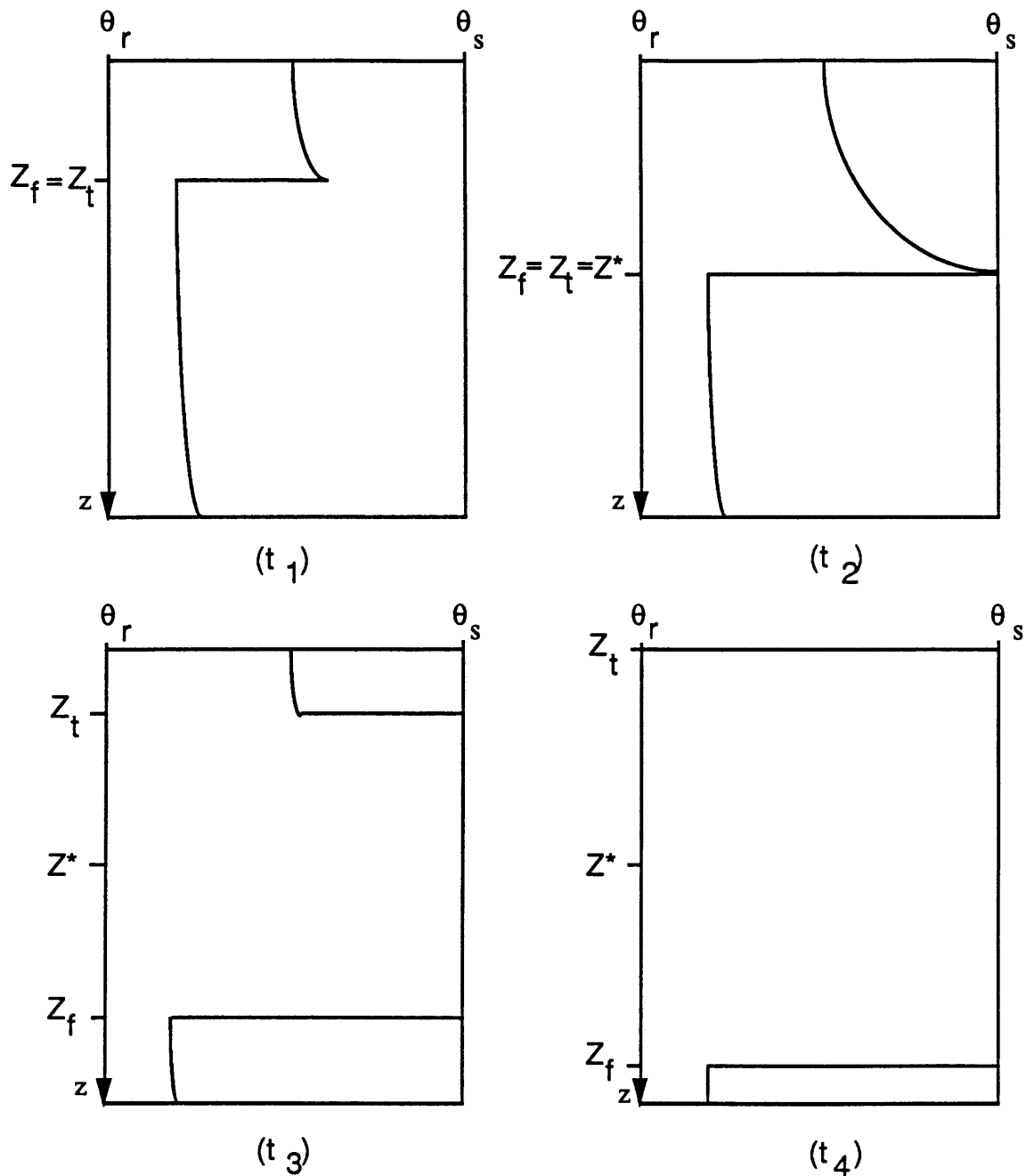
FIGURE 2.4: Evolution of the moisture profile over four consecutive time steps, t_1 through t_4, under constant rainfall rate, R. At time t_1 the wetting front is unsaturated. At time t_2, Z_f reaches the critical depth $Z^*(R)$ for which we have $K_s(Z^*) = R$. From time t_2 on, a zone of saturation develops and grows. At time t_4, the top of the zone of saturation reaches the soil surface, i. e. we have $Z_t = 0$.

flow above the wetting front is deflected laterally and is at an angle, $\alpha'(z)$, with the *vertical* direction. The flow deflection angle with respect to the *normal* direction, i.e. angle $(\alpha+\alpha'(z))$ in Figure 2.5, is related to conductivity, $K_s(z)$, through the law of refraction (see e.g. Freeze and Cherry, 1979, pp 172-3);

$$\frac{K_s(z_1)}{K_s(z_2)} = \frac{\tan(\alpha+\alpha'(z_1))}{\tan(\alpha+\alpha'(z_2))} \quad , \text{ for } Z_t \le z_1, z_2 \le Z_f \tag{2.22}$$

The boundary condition at the wetting front is

$$K_s(Z_f) = K_0 \cdot e^{-f \cdot Z_f}, \quad \alpha'(Z_f) = 0 \tag{2.23}$$

Substitution of (2.23) into (2.22) yields

$$\frac{K_s(z)}{K_s(Z_f)} = \frac{\tan(\alpha+\alpha'(z))}{\tan(\alpha)} \tag{2.24}$$

Substituting (2.12) and solving (2.24) for $\alpha'(z)$,

$$\alpha'(z) = \tan^{-1}[\, e^{f \cdot (Z_f-z)} \cdot \tan(\alpha) \,] - \alpha \tag{2.25}$$

Equation (2.25) shows that the angle of flow with respect to the vertical direction increases upward from Z_f to the top of the perched saturation zone (depth Z_t). Figure 2.6 represents angle $\alpha'(z)$ over depth within the zone of saturation, given f, Z_t and three different values of Z_f. Since $\alpha'(z)$ decreases with depth, the flow lines within the zone of saturation are curved, as represented schematically in Figure 2.7.
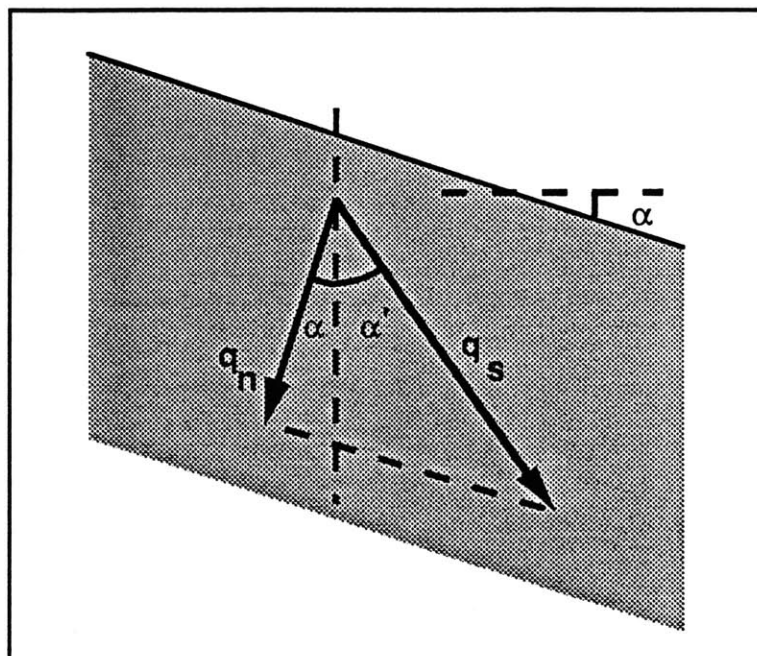
FIGURE 2.5: Representation of the flow vector, q_s, and the component of flow in the normal direction, q_n. The angle of flow with respect to the normal direction is $(\alpha + \alpha'(z))$.
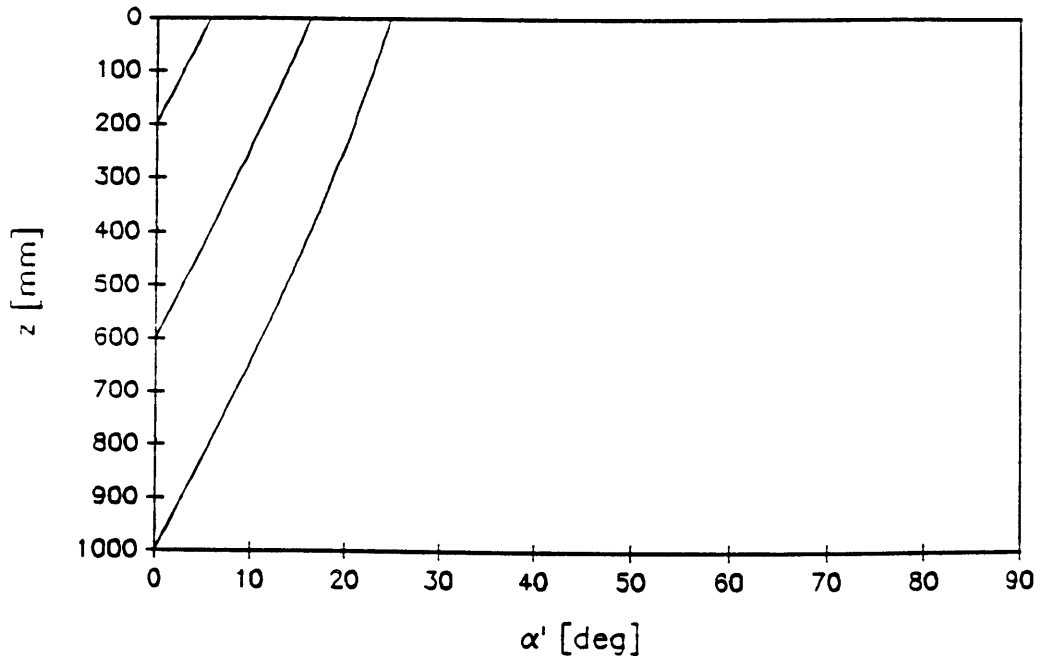
FIGURE 2.6: Profile of $\alpha'(z)$ over the saturated depth, with $Z_t = 0$ mm, $f = 10^{-3}$ mm^{-1}, and $\alpha = 45°$, for three wetting front depths, $Z_f = 200$ mm, $Z_f = 600$ mm and $Z_f = 1000$ mm.
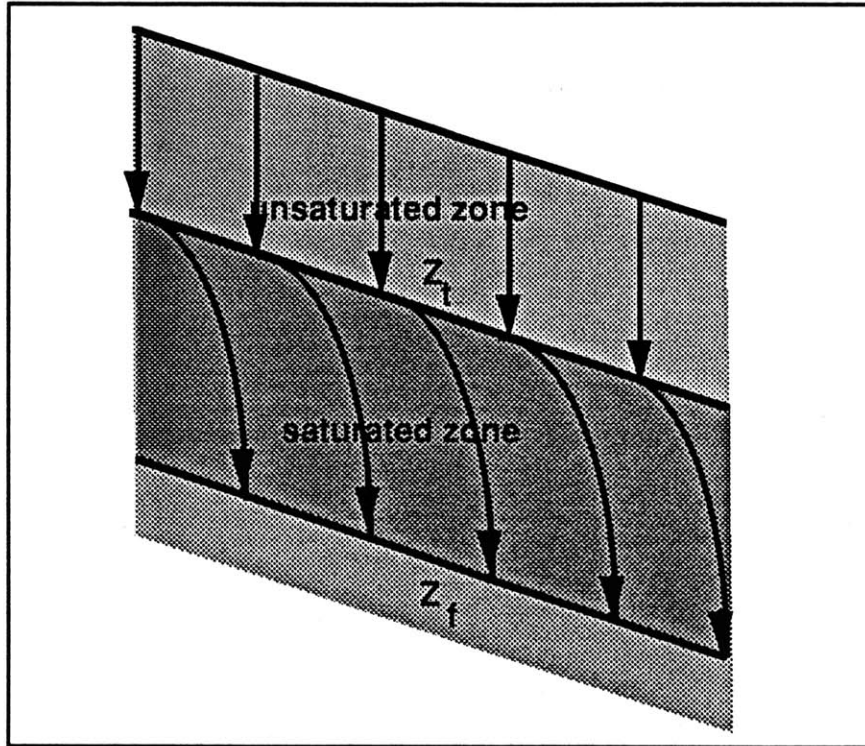
FIGURE 2.7: Flow lines in the unsaturated and saturated zones of the wetted soil. Flow is vertical in the unsaturated zone. In the saturated zone, decreasing permeability with depth causes deflection of flow. Flow deflection decreases with depth and flow is vertical at the wetting front. For large (Z_f-Z_t) or large f values, flow near the top of the saturation zone (i. e. at depth Z_t) is nearly parallel to terrain slope.

Figure 2.8 represents $\alpha'(Z_t)$ as a function of terrain inclination angle α, for two different values of f and given values of Z_f and Z_t. We see that for large f values, the angle approaches $\alpha'(z) = 90^\circ - \alpha$, that is, flow becomes closely parallel to the terrain surface.

At a depth z within the zone of saturation, flow has both a vertical and a horizontal component, $q_z(z)$ and $q_h(z)$, such that,

$$\tan(\alpha'(z)) = \frac{q_h(z)}{q_z(z)} \quad , \text{for } Z_t \leq z \leq Z_f \tag{2.26}$$

Given that the soil is isotropic, the ratio between the horizontal and vertical components of flow equals the ratio between the hydraulic gradients in these two directions, $J_h(z)$ and $J_z(z)$. Thus, from (2.26),

$$\tan(\alpha'(z)) = \frac{J_h(z)}{J_z(z)} \quad , \text{for } Z_t \leq z \leq Z_f \tag{2.27}$$

The vertical gradient of hydraulic potential is

$$J_z(z) \equiv -\frac{\partial \Phi(z,h)}{\partial z} = -\frac{\partial}{\partial z}\left[e(z,h) + \frac{P(z)}{\gamma} \right] = 1 - \frac{1}{\gamma} \cdot \frac{dP(z)}{dz} \tag{2.28}$$

where $\Phi(z,h)$ is the total gravitational potential at location (z,h);
e(z,h) is the elevation potential at location (z,h);
and $P(z)/\gamma$ is the pressure potential induced by gravity at depth z.

The horizontal gradient of hydraulic potential is

$$J_h(z) \equiv -\frac{\partial \Phi(z,h)}{\partial h} = -\frac{\partial}{\partial h}\left[e(z,h) + \frac{P(z)}{\gamma} \right] = -\frac{1}{\gamma} \cdot \frac{\partial P(z)}{\partial h}$$
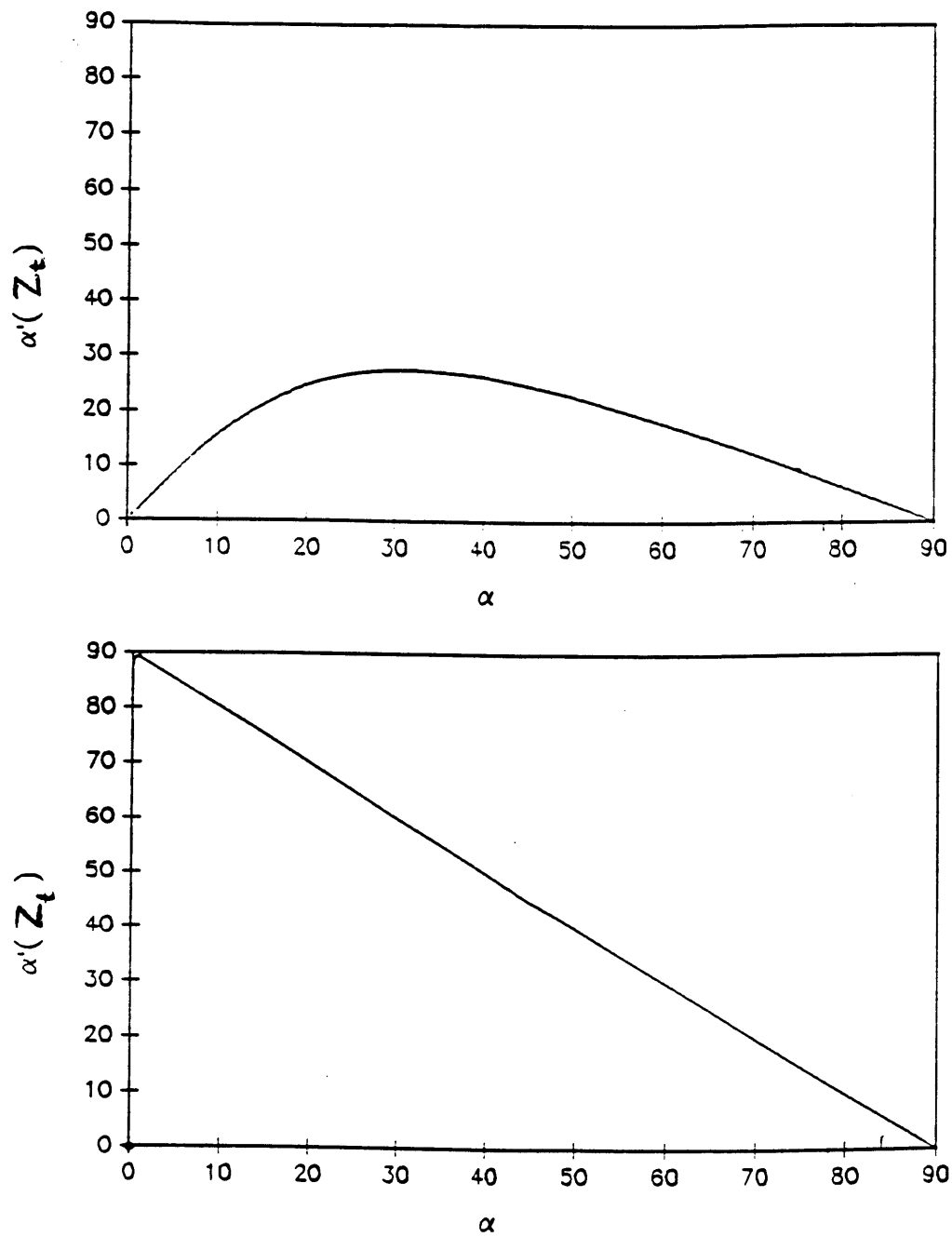
FIGURE 2.8: Angle of flow at the top of the zone of saturation, $\alpha'(Z_t)$, as a function of terrain inclination angle α, with $Z_t = 0$ mm, $Z_f = 1000$ mm, and (a) $f = 10^{-3}$ mm^{-1}; and (b) $f = 10^{-2}$ mm^{-1}.

$$= -\frac{1}{\gamma} \cdot \frac{\partial z}{\partial h} \cdot \frac{dP(z)}{dz} = \tan(\alpha) \cdot \frac{1}{\gamma} \cdot \frac{dP(z)}{dz} \qquad (2.29)$$

Thus, we have

$$J_h(z) = (1 - J_z(z)) \cdot \tan(\alpha) \qquad (2.30)$$

Solving (2.27) for $J_h(z)$,

$$J_h(z) = \tan(\alpha'(z)) \cdot J_z(z) \qquad (2.31)$$

Equating (2.30) and (2.31) we obtain $J_z(z)$ and the vertical component of flow;

$$J_z(z) = \frac{\tan(\alpha)}{\tan(\alpha) + \tan(\alpha'(z))} \; ; \qquad q_z(z) = J_z(z) \cdot K_0 \cdot e^{-f \cdot z} \qquad (2.32)$$

Substituting (2.32) into (2.31) we obtain $J_h(z)$ and the horizontal component of flow;

$$J_h(z) = \frac{\tan(\alpha) \cdot \tan(\alpha'(z))}{\tan(\alpha) + \tan(\alpha'(z))} \; ; \qquad q_h(z) = J_h(z) \cdot K_0 \cdot e^{-f \cdot z} \qquad (2.33)$$

Figures 2.9 and 2.10 represent the vertical and horizontal gradients over depth within the zone of saturation, for given f, Z_t and three different values of Z_f. Figures 2.11 and 2.12 represent $J_z(Z_t)$ and $J_h(Z_t)$ as a function of terrain inclination α, for given f, Z_t and Z_f. We see that $J_h(Z_t)$ has a maximum at $\alpha = 45^o$. This indicates that maximum lateral flow occurs with $\alpha = 45^o$.
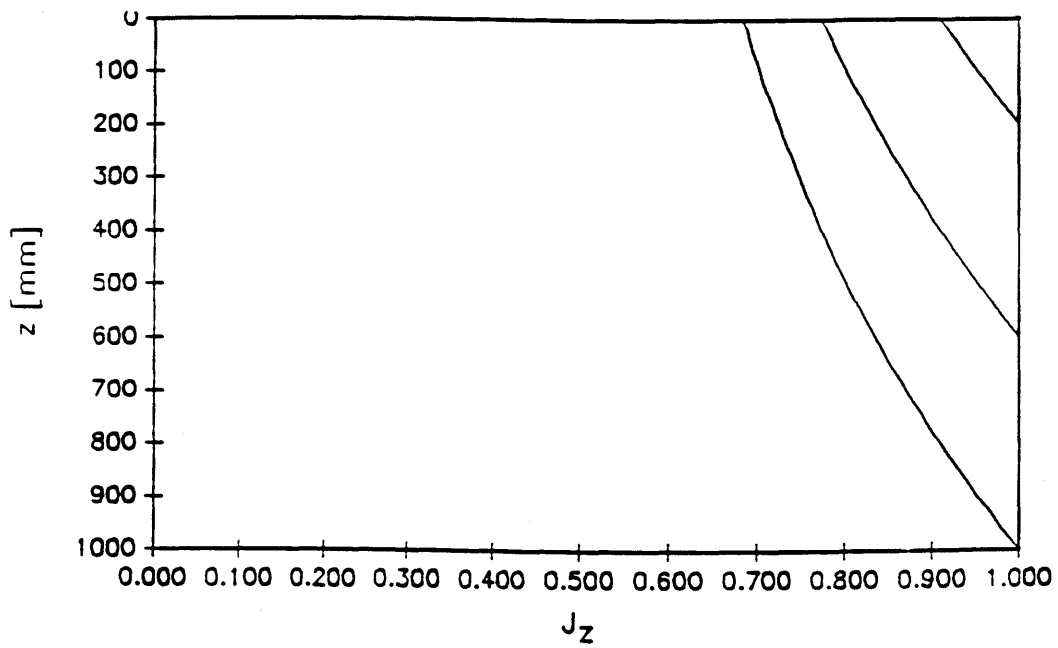
FIGURE 2.9: Profile of $J_z(z)$ over the saturated depth, with Z_t = 0 mm, f = 10^{-3} mm^{-1}, and α = 45°, for three wetting front depths, Z_f = 200 mm, Z_f = 600 mm and Z_f = 1000 mm.
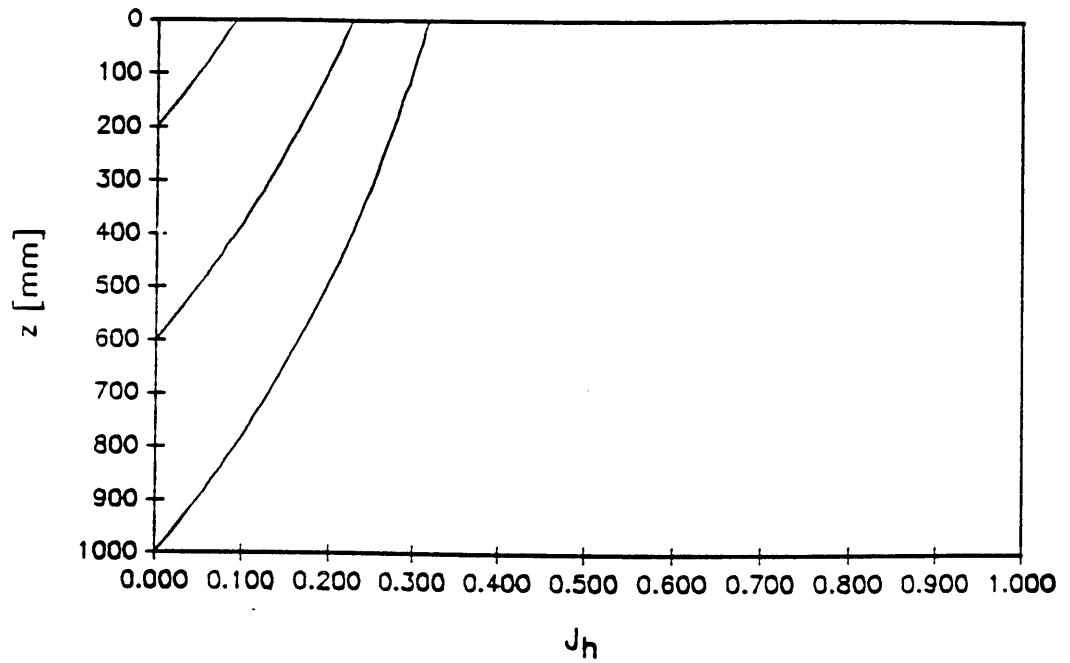
FIGURE 2.10: Profile of $J_h(z)$ over the saturated depth, with $Z_t = 0$ mm, $f = 10^{-3}$ mm^{-1}, and $\alpha = 45°$, for three wetting front depths, $Z_f = 200$ mm, $Z_f = 600$ mm and $Z_f = 1000$ mm.
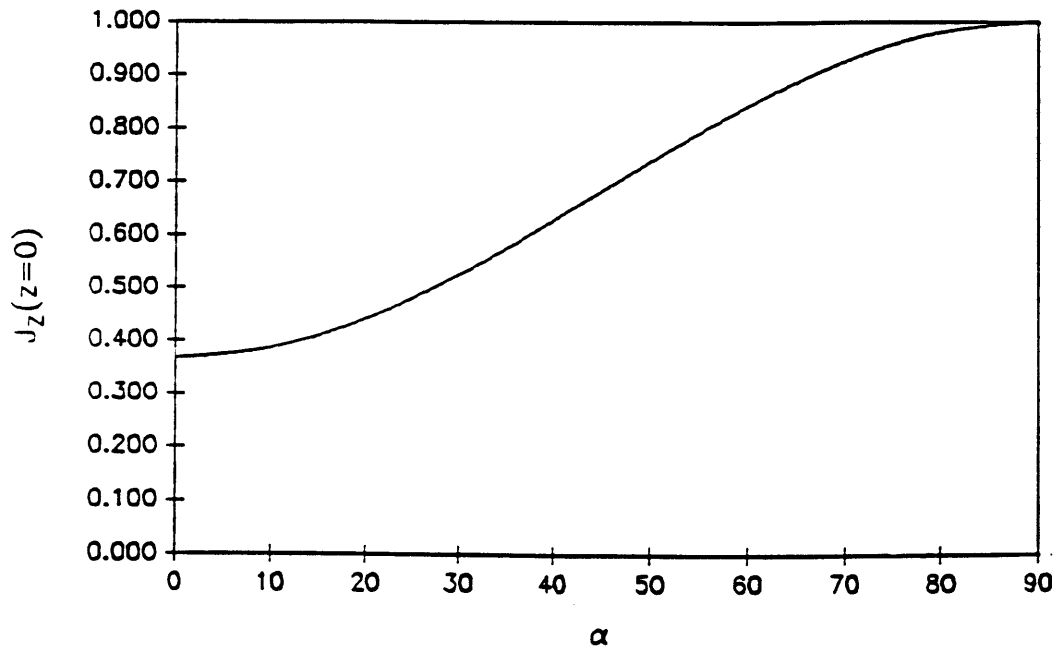
FIGURE 2.11: Vertical gradient of hydraulic potential at the top of the zone of saturation, $J_z(Z_t)$, as a function of terrain inclination angle α, with $Z_t = 0$ mm, $Z_f = 1000$ mm, and $f = 10^{-3}$ mm^{-1}.
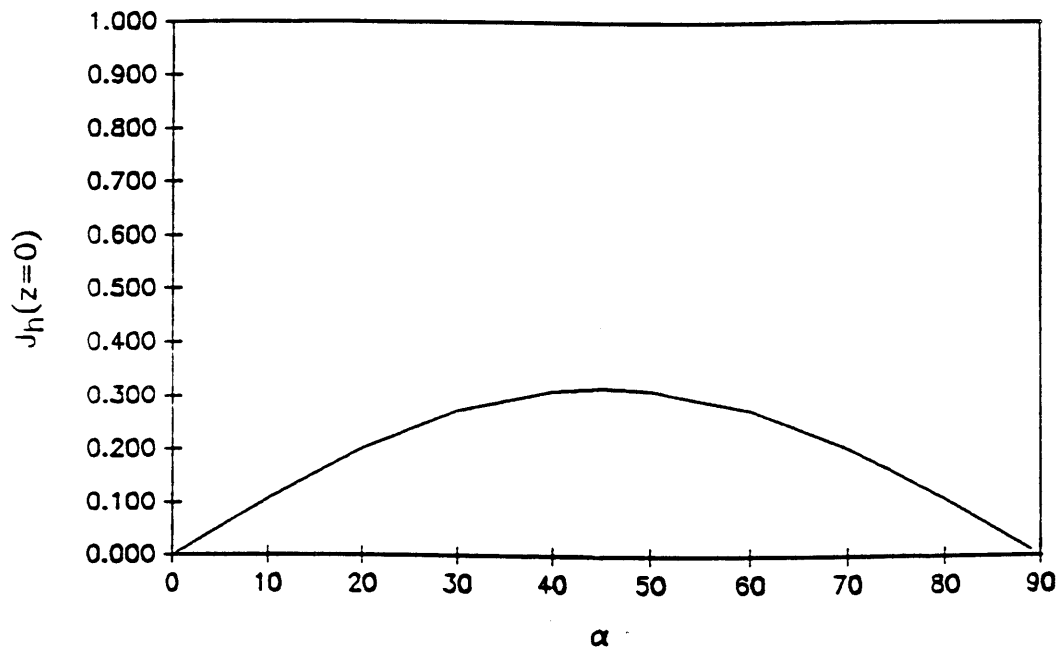
FIGURE 2.12: Horizontal gradient of hydraulic potential at the top of the zone of saturation, $J_h(Z_t)$, as a function of terrain inclination angle α, with $Z_t = 0$ mm, $Z_f = 1000$ mm, and $f = 10^{-3}$ mm^{-1}.

The flow continuity equation must now be written in two dimensions. As we will see, it is more convenient to write the continuity equation for the orthogonal components of flow in the n and p directions than for the z and h directions. The continuity equation is

$$\frac{\partial\theta}{\partial t} + \frac{\partial q_n(z)}{\partial n} + \frac{\partial q_p(z)}{\partial p} = 0 \qquad (2.34)$$

Integration of (2.34) over z (with $Z_t < z_1 < Z_f$ and $z_2 > Z_f$) leads to

$$\frac{d}{dt}\int_{z_1}^{z_2}\theta{\cdot}dz + \frac{\partial}{\partial n}\int_{z_1}^{z_2}q_n(z){\cdot}dz + \frac{\partial}{\partial p}\int_{z_1}^{z_2}q_p(z){\cdot}dz = 0 \qquad (2.35)$$

Applying the chain rule,

$$\frac{d}{dt}\int_{z_1}^{z_2}\theta{\cdot}dz + \frac{\partial z}{\partial n}{\cdot}\frac{\partial}{\partial z}\int_{z_1}^{z_2}q_n(z){\cdot}dz + \frac{\partial z}{\partial p}{\cdot}\frac{\partial}{\partial z}\int_{z_1}^{z_2}q_p(z){\cdot}dz = 0 \qquad (2.36)$$

As we have $\partial z/\partial p = 0$, the last term in (2.36) is zero, and the equation reduces to the one-dimensional form (with $\partial z/\partial n = 1/\cos(\alpha)$),

$$\frac{d}{dt}\int_{z_1}^{z_2}\theta{\cdot}dz + \frac{1}{\cos(\alpha)}{\cdot}q_n(z)\Big|_{z_1}^{z_2} = 0 \qquad (2.37)$$

Within the zone of saturation, we have $\theta(z) = \theta_s$ and $\partial\theta/\partial z = 0$. Since z is constant along direction p, we have $\partial q_p(z)/\partial p = 0$. Therefore, the Continuity Equation (2.34) gives $\partial q_n(z)/\partial n = 0$ within the saturated zone.

Thus, $q_n(z)$ is constant in the saturated zone, i.e., $q_n(z) = q_n(Z_f)$ for $Z_t \leq z \leq Z_f$. Substituting $q_n(Z_f)$ for $q_n(z_1)$ in (2.37), we obtain

$$\frac{d}{dt}\int_{z_1}^{z_2} \theta \cdot dz \ + \frac{1}{\cos(\alpha)} \cdot [q_n(z_2) - q_n(Z_f)] = 0 \tag{2.38}$$

From geometrical considerations, the normal component of vertical flow is $q_n(z) = \cos(\alpha) \cdot q_z(z)$, and (2.38) can be written as

$$\frac{d}{dt}\int_{z_1}^{z_2} \theta \cdot dz \ + [q_z(z_2) - q_z(Z_f)] = 0$$

or

$$\frac{d}{dt}\int_{z_1}^{z_2} \theta \cdot dz \ + [R_i - K_0 \cdot e^{-f Z_f}] = 0 \tag{2.39}$$

where R_i is the initial infiltration rate. The procedure for estimating R_i is described in Section 3.D.

Through substitution of Equation (2.16) for $\theta(R_i, z)$, the integral of moisture in (2.39) is

$$\int_{z_1}^{z_2} \theta \cdot dz = \int_{z_1}^{Z_f} \theta_s \cdot dz + \int_{Z_f}^{z_2} \theta(R_i, z) \cdot dz$$

$$= \theta_s \cdot (Z_f - z_1) + \left[\left(\frac{R_i}{K_0} \right)^{\frac{1}{\varepsilon}} \cdot (\theta_s - \theta_r) \cdot \left(\frac{\varepsilon}{f} \right) \cdot (e^{\frac{f}{\varepsilon} \cdot z_2} - e^{\frac{f}{\varepsilon} \cdot Z_f}) + \theta_r \cdot (z_2 - Z_f) \right] \tag{2.40}$$

Differentiating (2.40) with respect to time,

$$\frac{d}{dt}\int_{z_1}^{z_2}\theta\cdot dz = \frac{dZ_f}{dt}\cdot\left[\theta_s - \left(\frac{R_i}{K_0}\right)^{\frac{1}{\epsilon}}\cdot(\theta_s-\theta_r)\cdot e^{\frac{f}{\epsilon}\cdot Z_f} - \theta_r\right]$$

$$= \frac{dZ_f}{dt}\cdot(\theta_s-\theta(R_i,Z_f)) \tag{2.41}$$

Substituting (2.41) into (2.39) and solving for dZ_f/dt, we obtain

$$\frac{dZ_f}{dt} = \frac{K_0\cdot e^{-f\cdot Z_f} - R_i}{\theta_s - \theta(R_i,Z_f)} \tag{2.42}$$

Derivation of the equation of evolution for Z_t is done in entirely analogous manner to the derivation of the equation of evolution for Z_f. Integration of Equation (2.34) over z again leads to Equation (2.37), but now with z_1 and z_2 defined by $z_1 < Z_t < z_2 < Z_f$. We saw that $q_n(z)$ is constant for $Z_t \leq z \leq Z_f$. Substituting $q_n(Z_f)$ for $q_n(z_2)$ in (2.37), we obtain

$$\frac{d}{dt}\int_{z_1}^{z_2}\theta\cdot dz + \frac{1}{\cos(\alpha)}\cdot[q_n(Z_f) - q_n(z_1)] = 0 \tag{2.43}$$

Flow is vertical at z_1 (since it is unsaturated and we are neglecting pore pressure); and is also vertical at the wetting front. Therefore, the component of flow in the n direction is obtained geometrically from the flow as $q_n(z) = \cos(\alpha)\cdot q_z(z)$, and (2.43) becomes

$$\frac{d}{dt}\int_{z_1}^{z_2}\theta\cdot dz + [q_z(Z_f) - q_z(z_1)] = 0$$

or

$$\frac{d}{dt}\int_{z_1}^{z_2} \theta \cdot dz \; + [K_0 \cdot e^{-f \cdot Z_f} - R] = 0$$

$$(2.44)$$

The integral of moisture in (2.44) is

$$\int_{z_1}^{z_2} \theta(R,z) \cdot dz = \theta_s \cdot (z_2 - Z_t) + \int_{z_1}^{Z_t}\left[\left(\frac{R}{K_0}\right)^{\frac{1}{\varepsilon}} \cdot (\theta_s - \theta_r) \cdot e^{\frac{f}{\varepsilon} \cdot z} + \theta_r \right] \cdot dz$$

$$= \theta_s \cdot (z_2 - Z_t) + \left(\frac{R}{K_0}\right)^{\frac{1}{\varepsilon}} \cdot (\theta_s - \theta_r) \cdot \left(\frac{\varepsilon}{f}\right) \cdot (e^{\frac{f}{\varepsilon} \cdot Z_t} - e^{\frac{f}{\varepsilon} \cdot z_1}) + \theta_r \cdot (Z_t - z_1) \quad (2.45)$$

Differentiating (2.45) with respect to time,

$$\frac{d}{dt}\int_{z_1}^{z_2} \theta \cdot dz = \frac{dZ_t}{dt} \cdot \left[\left(\frac{R}{K_0}\right)^{\frac{1}{\varepsilon}} \cdot (\theta_s - \theta_r) \cdot e^{\frac{f}{\varepsilon} \cdot z} + \theta_r - \theta_s \right]$$

$$= \frac{dZ_t}{dt} \cdot (\theta(R, Z_t) - \theta_s)$$

$$(2.46)$$

Substituting (2.46) into (2.44) and solving for dZ_t/dt yields

$$\frac{dZ_t}{dt} = \frac{K_0 \cdot e^{-f \cdot Z_f} - R}{\theta_s - \theta(R, Z_t)}$$

$$(2.47)$$

Since we have $R > K_0 \cdot e^{-f \cdot Zf}$, the time differential of Z_t is negative, i.e., Z_t approaches the terrain surface. Eventually, Z_t will reach the surface ($Z_t = 0$), and from then on we must have

$$Z_t = 0 \; ; \qquad \frac{dZ_t}{dt} = 0$$

$$(2.48)$$

For $Z_t = 0$, compatibility of (2.47) with (2.48) requires that $R = K_0.e^{-f.Zf}$, with R now representing the rate of infiltration. Therefore, when Z_t reaches zero, the rate of infiltration drops from the rainfall rate to the saturated conductivity at the wetting front. Designating the rate of infiltration by R_{inf} and the rate of runoff by R_r,

$$R_{inf} = \begin{cases} \text{Before ponding } (Z_t > 0): & R \\ \text{After ponding } (Z_t = 0): & K_0.e^{-f.Zf} \end{cases}$$

$$R_r = R - R_{inf} \tag{2.49}$$

2.C VARIABLE RAINFALL RATES

During a rainstorm, the rainfall rate at any location varies in time. This variation can be approximated by a succession of short time intervals of steady rainfall rate. At the start of each time interval, a new wave of moisture leaves the surface and propagates downward in the soil profile. The vertical moisture profile can therefore be conceptualized as a succession of waves. Figures 2.13 and 2.14 represent complex moisture profiles for a soil where conductivity decreases exponentially with depth. If a rainfall rate R_1 is succeeded by a higher rainfall rate R_2, the moisture profile will initially resemble the schematic representation of Figure 2.13. If instead we have R_2 being less than R_1, then the moisture profile will resemble that in Figure 2.14.
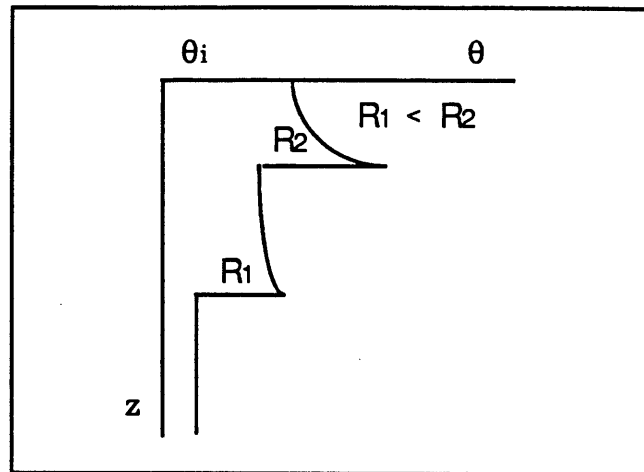
FIGURE 2.13: Moisture profile after a step increase in rainfall rate for a soil where conductivity decreases exponentially with depth.
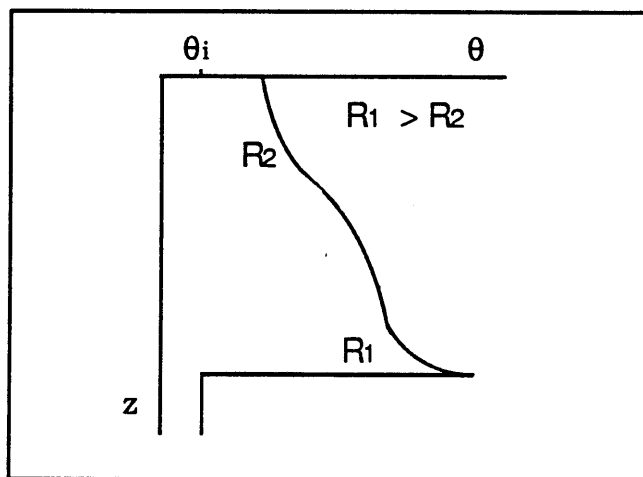
FIGURE 2.14: Moisture profile after a step decrease in rainfall rate for a soil where conductivity decreases exponentially with depth.

Modeling of this process of successive moisture waves, propagating at different velocities, overruning each other or spreading apart, would require keeping track of multiple state variables, each representing the depth Z_{f_i} of each wave i. Charbeneau (1984) presents solutions for the soil moisture profile for a succession of time intervals of different rainfall rates. However, both memory and computational requirements to carry out such computations would be prohibitive. For simplicity, a conceptual approximation is introduced to the vertical moisture profile. The complex profile of succeeding waves is approximated by a single-wave profile that contains the same volume of moisture.

The single-wave approximation requires introducing a *third state variable*, representing the uniform rate of vertical flow that corresponds to the single wave approximation. The new variable is designated R_e, and can be conceptualized as representing an *"equivalent"* steady rainfall rate in the sense that the kinematic wave that corresponds to rate R_e *contains the same volume* as the true, complex profile. (Note that R_e generally does not coincide with the average rainfall rate, given the non-linearity of the K-θ relation.)

We can derive an expression for R_e from the moisture storage in the soil. R_e is a function of the volume of moisture stored in the soil above depth Z_t i. e., in the unsaturated zone of the wetted soil. The moisture volume per unit area (dimension L) above the wetting front is M_t (for "total" moisture). The moisture volume per unit area above Z_t is M_u (for "unsaturated" moisture). M_u is obtained from M_t by subtraction of the moisture volume in the saturated zone between depths Z_f and Z_t. (Note that if the front is unsaturated, we have $Z_t = Z_f$ and $M_u = M_t$.) Thus,

$$M_t = \int_0^{Z_f} \theta(z) \cdot dz \qquad (2.50)$$

$$M_u = \int_0^{Z_t} \theta(z) \cdot dz \qquad (2.51)$$

$$M_u = M_t - \theta_s \cdot (Z_f - Z_t) \qquad (2.52)$$

By definition of R_e, the single-wave approximation $\theta(R_e, z)$ contains the same volume of moisture as the complex true moisture profile $\theta(z)$. Therefore, we may replace $\theta(R_e, z)$ for $\theta(z)$ in the above integrals. Expression (2.51) becomes:

$$\int_0^{Z_t} \theta(R_e, Z_t) \cdot dz = M_u \qquad (2.53)$$

This integral can be solved for R_e analytically upon substitution of the expression for $\theta(R_e, z)$. The expression for $\theta(R, z)$ is given in (2.16). Letting $R = R_e$, and substituting (2.16) into (2.53) we obtain

$$\int_0^{Z_t} \left[\left(\frac{R_e}{K_0} \right)^{\frac{1}{\varepsilon}} \cdot (\theta_s - \theta_r) \cdot e^{\frac{f}{\varepsilon} \cdot z} + \theta_r \right] \cdot dz = M_u \qquad (2.54)$$

Solving for R_e,

$$R_e = K_0 \cdot \left(\frac{M_u - \theta_r \cdot Z_t}{(\theta_s - \theta_r) \cdot \left(\frac{\varepsilon}{f} \right) \cdot (e^{\frac{f}{\varepsilon} \cdot Z_t} - 1)} \right)^{\varepsilon} \qquad (2.55)$$

68

Note that if Z_t is at the surface i. e., if the full depth of wetted soil is saturated, there is no unsaturated moisture profile to approximate (M_u = 0). In this case, we define R_e = R. The expressions derived above for R_e apply for Z_t >0.

Chapter 3

THE RAINFALL-RUNOFF MODEL AT THE BASIN SCALE

In this Chapter we present a rainfall-runoff model to be used for flood prediction at the basin scale. The rainfall-runoff model considers the soils in the basin to be represented by the parameterization of hydraulic conductivity given in Equation (2.12), and uses the kinematic model of infiltration presented in Chapter 2.

In Chapter 2 we considered infiltration under idealized spatial uniformity of all parameters and variables. Over a catchment as well as at the hillslope scale, however, soil properties, slope, moisture conditions, and rainfall inputs vary areally. In Chapter 2 we saw that the kinematic model of infiltration predicts lateral subsurface saturated flows in a soil where conductivity decreases with depth. Under the condition of spatial uniformity, kinematic infiltration was described by the one-dimensional form of the continuity equation. Under spatially heterogeneous conditions, however, infiltration must be considered in three dimensions. Given that full solution of three-dimensional differential equations would be computationally prohibitive at the basin scale, the model uses spatial discretization into areally uniform elements to reduce three-dimensional differential equations to their one-dimensional form. Thus, the infiltration equations developed in Chapter 2 apply within each element. Spatial discretization is described in Section 3.A. Lateral flows between elements is accounted for through a computational scheme that allows simplified

element coupling. The element coupling procedure is described in Section 3.B.

The computational procedure also involves temporal discretization. At each time step, the state of moisture of each element is updated and the rate of infiltration-excess, saturation-excess and return flow runoff is computed.

To determine saturation-excess runoff, the model considers an estimated initial water-table. The procedure for water-table estimation and for moisture initialization above the water-table is described in Section 3.D. Rainfall over elements where the water-table is at the soil surface (saturated elements) becomes saturation-excess runoff. Infiltration-excess, saturation-excess and return flow runoff contribute to streamflow, and are routed over the hillslope and along stream-channels to the basin outlet. Section 3.E describes the routing procedure.

3.A SPATIAL DISCRETIZATION AND COMPUTATIONS IN ONE ELEMENT

Basin elements are taken as the pixels of the D.E.M. grid. This is done for various reasons which are summarized next. First, the use of elements in a regular grid offers considerable computational advantage. Element parameters and variable values can be stored in a rectangular matrix, and each element is easily referenced by its row and column numbers, facilitating both compact data storage and rapid data extraction; element boundaries are rectangular and neighboring elements are easily

71

identified; computation algorithms are greatly simplified. Second, the model emphasizes terrain morphology, and the variables describing topography can be extracted most simply and without bias from a regular matrix of terrain elevations, as opposed to through the extraction of contour lines (Tarboton, 1989). Third, algorithms for extraction of river-channel networks from regular D.E.M.s have been developed and proven to compare well with mapped data, and the use of the D.E.M. grid for basin discretization allows straightforward incorporation of extracted channel networks. Finally, D.E.M. rectangular grids are available for great part of the U.S. territory (at 30m x 30m and 60m x 90m grids) and many other parts of the World. The available resolution is in general superior to that of soil maps (from which soil parameters are estimated) and to that of radar measurements of rainfall rate.

Each element of the model consists of a soil column with rectangular horizontal cross-sectional area and is characterized by its soil properties, maximum slope (tan(α)) and direction of maximum slope. Soil properties may vary between elements, and in general can be obtained from digitized soil maps.

It is assumed that soil properties, slope, rainfall rate, and the initial moisture profile are areally uniform *within an element*. The equations derived in the previous section for a hillslope of spatially uniform characteristics therefore apply within an element. Spatial variability of soil type, terrain slope and rainfall rate exists *among* elements, and lateral subsurface discharge of moisture from one element to the next differs among elements. Inputs and outputs of moisture into and from an element are not equal, and lateral flows affect the moisture storage in any element. Therefore, even having reduced infiltration in each element to its

one-dimensional form, we must account for the balance of lateral moisture inputs and outputs when updating the moisture storage in the element. In Section 3.B, we present a computational procedure that allows for element coupling through lateral flows.

Complete description of the state of moisture in one element requires three **state variables**, M_t, Z_f and Z_t, defined in Chapter 2. All other variables required to write the equations of evolution (i. e. the differential equations in time) for the state variables are obtained from them. The equations of evolution for Z_f and Z_t were derived in Section 2.B. The equation of evolution for the moisture storage, M_t, is obtained from straightforward mass balance considerations. The input flows are infiltrated rainfall, and the lateral flows from contributing elements, Q_{in}. The output is the lateral flow, Q_{out}, from the element of interest to a neighboring element.

As we saw in 2.B, lateral flows are generated only from the saturated zone. Thus, the general expression for the volumetric discharge from an element to the element situated downslope from it is

$$Q_{out} = W \cdot \int_{Z_t}^{Z_f} q_h(z) \cdot dz \qquad (3.1)$$

where W represents the width of flow, i.e., the width perpendicular to the flow direction. For flow in the x or y directions, W is Δy or Δx, respectively; for flow at an angle with the x and y directions, W is $(\Delta x \cdot \Delta y)/\sqrt{\Delta y^2 + \Delta y^2}$.

Through substitution of Equation (2.33) for $q_h(z)$ in the above integral,

73

$$Q_{out} = W \cdot \int_{Z_t}^{Z_f} \frac{\tan(\alpha) \cdot \tan(\alpha'(z))}{\tan(\alpha) + \tan(\alpha'(z))} \cdot K_0 \cdot e^{-f \cdot z} \cdot dz \tag{3.2}$$

The above integral equals the following (see Appendix B),

$$Q_{out} = W \cdot K_0 \cdot \cos(\alpha) \cdot \sin(\alpha) \cdot e^{-f \cdot Z_f} \left[\frac{1}{f} \cdot (e^{-f \cdot Z_t} - e^{-f \cdot Z_f}) - (Z_f - Z_t) \right] \tag{3.3}$$

Below we summarize the equations of evolution for the three state variables, and the expressions through which the other variables involved in those equations are obtained from the state variables. In the equations below, A designates element area. Estimation of Q_{in} is achieved through the element coupling scheme which is explained in Section 3.B.

$$\frac{dM_t}{dt} = \frac{dZ_f}{dt} \cdot \theta(R_i, Z_f) + Min(R, K_0) + \frac{Q_{in} - Q_{out}}{A}$$

$$\frac{dZ_f}{dt} = \begin{cases} \text{unsaturated: } \dfrac{R_e - R_i}{\theta(R_e, Z_f) - \theta(R_i, Z_f)} \\[4ex] \text{saturated: } \quad \dfrac{K_0 \cdot e^{-f \cdot Z_f} - R_i}{\theta_s - \theta(R_i, Z_f)} \end{cases}$$

$$\frac{dZ_t}{dt} = \begin{cases} \text{unsaturated: } \dfrac{dZ_f}{dt} \\[4ex] \text{saturated: } \quad \dfrac{K_0 \cdot e^{-f \cdot Z_f} - R_e}{\theta_s - \theta(R_e, Z_f)} \end{cases}$$

where

$$R_e = K_0 \cdot \left(\frac{M_u - \theta_r \cdot Z_t}{(\theta_s - \theta_r) \cdot \left(\dfrac{\varepsilon}{f}\right) \cdot (e^{\frac{f}{\varepsilon} \cdot Z_t} - 1)} \right)^{\varepsilon}$$

$$M_u = M_t - \theta_s \cdot (Z_f - Z_t)$$

$$\theta(R,z) = \left(\frac{R}{K_0}\right)^{\frac{1}{\varepsilon}} \cdot e^{\frac{f}{\varepsilon} \cdot z} \cdot (\theta_s - \theta_r) + \theta_r$$

$$Q_{out} = W \cdot K_0 \cdot \cos(\alpha) \cdot \sin(\alpha) \cdot e^{-f \cdot Z_f} \left[\frac{1}{f} \cdot (e^{-f \cdot Z_t} - e^{-f \cdot Z_f}) - (Z_f - Z_t) \right]$$

3.B ELEMENT COUPLING

When subsurface flow has a lateral component, the state of elements located upstream and downstream mutually affect each other. Thus, the equations of evolution of the three state variables are coupled to all other equations of the elements that contribute subsurface flows to the same stream element. Simultaneous integration of the large number of coupled differential equations would be exceedingly numerically intensive given the objectives of this work, but if the lateral component of flow is significant, computations should incorporate element interactions, even if in an approximate way. We present a computational procedure that allows for element coupling through lateral flows in a simplified manner. The computational technique treats each element at a time but processes elements in an order that still allows for coupling of elements through

lateral flows. Thus, just three differential equations, corresponding to the state variables of one element, need be integrated jointly.

Computations start with the uphill elements and work their way down to the elements at the bottom of the hillslope. This order of computations guarantees that when the state variables are updated for any element, the outflow from each element that discharges into it has already been computed. The computational procedure relies on time as well as spatial discretization. Within a time interval, the outflow from one element is computed by integration of the lateral flows in time. However, the average outflow rate (total discharge divided by the time interval considered) is used in updating the state variables in the element located downstream from it, and thus only one value need be stored for each element in element coupling.

In updating the state of moisture of each element, the balance between lateral flows is added to the expression for the integral of moisture above the wetting front, according to the equations of evolution for M_t provided in Section 3.A. Whenever the value of M_t exceeds the volume corresponding to complete saturation above the wetting front (i.e., $Z_f \cdot \theta_s$) and lateral inputs exceed lateral ouput from the element, *return flow* is generated. In other words, return flow is produced when the balance of lateral subsurface flows is positive and the element is already saturated. Return flow is added to the surface runoff volume that is routed through the basin.

3.C RAINFALL INPUTS

The rainfall rate in each element at each time step may be obtained either from radar or raingage measurements. Radar offers much larger spatial and temporal resolutions than can be provided by a network of telemetering raingages. The issue of estimation of rainfall rates from radar reflectivity measurements and its potential sources of error are reviewed in Austin (1987). Wyss *et al.* (1990) used radar estimates of rainfall as input to a distributed rainfall-runoff model. When radar measurements are not available, data from a network of telemetering raingages may be used. Various methods can be employed to estimate rainfall rate distribution from the point rainfall measurements. Perhaps the simplest of such methods is to use Thiessen polygons to approximate rainfall distribution. The method corresponds to approximating the rainfall rate in each element by the reading from the closest raingage. This method will be used in the model application presented in Chapter 4.

3.D GROUNDWATER INITIALIZATION

To account for the saturation-excess mechanism of runoff generation, the event-based model must be initialized with an estimated profile of the water-table. In this section, we describe how a computational procedure parallel to that presented in Section 2.B for the update of the near-surface moisture profile during a rainstorm, can be used to obtain

77

the water-table position, and the areas of soil saturation, at the time of onset of the rainfall event.

The model relies on a series of assumptions: (1) the rate of recharge of the water table is a slow-varying value with a seasonal cycle; (2) the water table adjusts to the seasonal fluctuations of recharge rate rapidly enough that, at any time between storms, it is in a steady state of equilibrium with the recharge rate; (3) the rate of water-table recharge between storms is spatially uniform over the catchment; (4) the aquifer is unconfined and covers the entire basin; and (5) groundwater flow in the general zone of saturation can be described as a Darcian flow system i. e., macropore and pipe flow are negligible. These assumptions are implicit also in two models that have a similar intent to the model presented; TOPMODEL of Beven et al. (Beven and Kirkby, 1979; Beven and Wood, 1983; Beven et al., 1985), and the models of O'Loughlin and Moore (O'Loughlin, 1981, 1986; Moore et al., 1986).

Freeze and Cherry (1979) state that assumptions (1) and (2) are supported by field observations. It seems reasonable to expect that these assumptions will hold least strongly for low-transmissivity soils in regions where the range of values of water-table recharge varies greatly from the wet to the dry season, because the drainage of such soils may be too slow to allow an equilibrium to be reached with the low recharge rate. Assumptions (1) and (2) should hold best for the wet season, and for the purpose of flood forecasting the estimation of the water-table position in the wet, not dry, season is of interest. Assumptions (3) seems reasonable lacking information on the spatial distribution of the water-table recharge rate. However, spatial variations are to be expected as a of non-uniformity of rainfall rates, vegetation, etc. There appears to be the possibility of

investigating the correlation between terrain elevation, exposure, vegetation coverage, etc., and water-table recharge rates. Assumption (4) may or may not be met, but may represent a reasonable approximation, depending on the true situation on a particular basin. The computational scheme presented here allows consideration of spatially variable recharge rates, and of unconfined aquifers covering only part of the basin. However, it does not provide for confined aquifers, as it assumes a correspondence between level of the water table and hydraulic potential. Assumption (5) is probably the weakest, as macropores and pipes are believed to be present in most catchments. This assumption is acceptable in basins where macropore connectedness and piping is not well developed.

The equilibrium assumption (2) suggests that the rate of *recharge* can be estimated from the rate of *discharge* from the basin. The rate of recharge is estimated by dividing the volumetric discharge from the basin (measured at its outlet) by the basin area:

$$R_i = \frac{Q}{A_T} \tag{3.4}$$

where R_i is the water-table recharge rate;
Q is the observed baseflow from the basin; and
A_T is the basin area.

Groundwater flow in the saturated zone below the water-table is modelled in a manner similar to the element coupling scheme presented in 3.B. To compute water-table elevation, the saturated zone is initialized at full saturation of the soil profile (the initial water-table coincides with the terrain surface), and allowed to drain over time, under a constant and

spatially uniform rate of recharge, R_i, computed from (3.4). Unless soil transmissivity of the entire saturated soil column is very low, the initial discharge from the fully saturated soil is higher than recharge, and groundwater storage decreases. Therefore, the water table drops below the soil surface, at least in part of the basin. In time, the decrease in groundwater storage leads to progressively lower discharges. When discharge rate reaches the value of the recharge rate, the groundwater system remains stationary, in a state of equilibrium. The values obtained for the depth of the water table in each element when the steady state is reached are used in the initialization of the event-based rainfall-runoff model.

Only *one state variable*, the *depth to the water-table, Z_{wt}*, is required to characterize the state of the general zone of saturation in one element. Like Z_f and Z_t, Z_{wt} is measured in the vertical (z) direction, positive downwards, from the terrain surface, and has dimension L.

The equation of evolution for Z_{wt}, obtained by derivation analogous to that for Z_t in Section 2.B, is

$$\frac{dZ_{wt}}{dt} = \frac{\dfrac{Q_{in} - Q_{out}}{A} - R_i}{\theta_s - \theta(R_i, Z_{wt})} \tag{3.5}$$

where Q_{in} is the input subsurface flow into the element;
Q_{out} is the subsurface discharge from the element;
and A is the element area.

The general expression for Q_{out} is obtained through integration of the saturated horizontal flows over the saturated depth,

$$Q_{out} = W \cdot \int_{Z_{wt}}^{Z_{imp}} q_h(z) \cdot dz \qquad (3.6)$$

where Z_{imp} is the depth of an impermeable layer (the aquifer bottom), and W is the width of flow perpendicular to the direction of flow (the same as in (3.1)).

Representing the hydraulic gradient by $\nabla\Phi$, (3.6) may be written as

$$Q_{out} = W \cdot \int_{Z_{wt}}^{Z_{imp}} \nabla\Phi \cdot K_0 \cdot e^{-f \cdot z} \cdot dz$$

$$= W \cdot \nabla\Phi \cdot \frac{K_0}{f} \cdot (e^{-f \cdot Z_{wt}} - e^{-f \cdot Z_{imp}})$$

$$\cong W \cdot \nabla\Phi \cdot \frac{K_0}{f} \cdot e^{-f \cdot Z_{wt}} \qquad \text{, for } Z_{imp} \text{ large} \qquad (3.7)$$

Note that, since conductivity decreases exponentially with depth, knowledge of the aquifer depth, Z_{imp}, is not required for computation of Q_{out}, provided that the soil is relatively deep (Z_{imp} large).

Given that we are under the assumption of the aquifer being unconfined, the hydraulic gradient, $\nabla\Phi$, may be represented by the slope of the water-table surface. We approximate water-table slope in element i by the forward difference in water table elevations in the direction of highest water-table slope,

$$\nabla\Phi = \tan(\alpha) - \frac{Z_{wt}|_i - Z_{wt}|_j}{L} \qquad (3.8)$$

81

where $Z_{wt}|_i$ and $Z_{wt}|_j$ represent the depth of the water table for two elements i and j, with element j situated downstream from element i.

Similarly to the infiltration model, element coupling requires that the order of computations start with uphill elements and work its way down to the elements at the bottom of the hillslope. When groundwater storage is updated for each element, Q_{in} is obtained through the addition of the values of discharge, Q_{out}, from all the elements that contribute flows directly to the element of interest, which given the order of computations have already been computed.

An issue that must be noted is that the results depend on the boundary condition given by the hydraulic head (elevation) of the water surface in the stream located at the hillslope bottom. The deeper the stream channel and the lower the stage, the deeper we may expect the predicted water table to be in the vicinity of the channel, since the hydraulic gradient will be higher in this location. Data on streamwater-surface elevation along the stream network is generally not available. In fact, in the general situation no information is available on channel depth, and only a few sparse streamgages may be expected to provide stage readings. In this situation, we approximate streamwater-surface elevation by terrain elevation i. e., we assume that the level of the water surface in the channel equals the elevation of the channel banks. This is obviously not true, since we are dealing with baseflow, therefore *low* flows, for the purpose of groundwater initialization. This is a point where more realistic assumptions are needed in future improvements of the model. We expect that given the approximation used, the extent of the near-channel saturated areas are overestimated in our model.

3.E FLOW ROUTING

i) Overland flow

Runoff routing over the hillslope considers overland flow as a quickly channelized process rather than as a sheet flow regime (Freeze, 1980). Therefore, the runoff generated in an element is not allowed to infiltrate in unsaturated elements located downslope from it. The quality of this approximation is of course best for basins of high drainage density. Possible infiltration losses in microchannels are also neglected. Thus, all runoff generated at any hillslope element is routed to the stream network and contributes to the storm hydrograph.

Overland flow is routed using a constant velocity parameter, obtained through calibration. This is done lacking parameter estimates for more physically-based routing, and for simplicity of computation.

ii) Stream flow

Flow routing in the channel network also uses a constant travel velocity. This involves two approximations; (1) streamflow velocity is constant along the channel network at a given instant in time; and (2) streamflow velocity at any given point of the network is constant at all times (independently of discharge). While the first approximation is

supported by considerable research (as we will see below), the second approximation is reasonable only within a relatively narrow range of discharge values.

Leopold and Maddock (1953) studied the relation between streamflow velocity, V, and discharge, Q. They performed velocity measurements at different locations along the channel network at different times. Discharge varies with location at a given time (increasing downstream) and varies with time at a given location (according to some distribution of discharge values). These researchers attempted to relate velocity to discharge. Their experimental data were fitted by an exponential relation,

$$V = C \cdot Q^\alpha \qquad\qquad (3.7)$$

where C is a constant and α is a parameter. Equation (3.7) predicts that, at any given time, as discharge increase downstream in the channel, flow velocity also increases; and that, at aby given location, flow velocity will vary in response to discharge fluctuations. The fitted value of α for a fixed time and various locations is not the same as for a fixed location at different times.

For a given time and different locations, Leopold and Maddock found an average value of $\alpha = 0.1$ for semi-arid regions in the U.S. This value of α is small enough that we may expect a linear approximation to the V-Q relation to provide a reasonable estimate of total travel time in the channel network. This result is in agreement with that of Pilgrim (1977). This researcher conducted tracer studies, measuring total travel times in various stream reaches. The tracer studies revealed that travel times were approximately linearly related to channel length, implying that

estimation of travel times can be achieved with a uniform velocity parameter. Beven (1979) also has shown that channel kinematic-wave velocities may be approximated by a constant value, even though flow velocities depend on discharge rate. The assumption of uniform velocities in stream channels at any moment in time has been made by Surkan (1974) and Rodriguez-Iturbe and Valdes (1979), in their Geomorphological Unit Hydrograph concept. Kirkby (1976) has shown that catchment response becomes progressively more linear for large catchments, as channel travel times increasingly dominate the hydrograph form. The approximation is best for medium to high discharge rates, which are of interest to us.

For a given location at different times, flow velocity at a fixed location will vary in response to discharge fluctuations. Leopold and Maddock found an average value of $\alpha = 0.34$ for the same regions. Thus, the value of α for a fixed location with varying time is considerably larger than that for fixed time at various locations. One possible explanation for this fact may be that, at a given time, flow increase downstream is generally accompanied by a broadening of the channel cross-section, which allows increased discharge for an approximately constant velocity. An increase in discharge in time, however, is accompanied by an increase in velocity at a given location. If a large range of discharges in time is involved, a constant velocity value may not be expected to provide good estimates of travel time in the channels.

3.F PARAMETER SENSITIVITY AND CALIBRATION PROCEDURE

This section explores the sensitivity of model results to parameter values, rainfall rate and initial moisture condition. Sub-Section 3.F.1 explores sensitivity of infiltration-excess runoff and of lateral subsurface discharge in one element. Sub-Section 3.F.2 illustrates sensitivity of saturation-excess runoff to terrain morphology. Sub-Section 3.F.3 deals with calibration of conductivity parameter f.

3.F.1 SENSITIVITY IN ONE ELEMENT

i) Sensitivity of infiltration-excess runoff in one element to soil parameters and initial moisture condition

In this section we investigate model sensitivity to soil parameters K_0, f, θ_s, θ_r and ε, rainfall rate R and initial recharge rate R_i. We compare model results for a horizontal hillslope element in terms of ponding time and infiltration-excess runoff generated.

Figures 3.1 through 3.5 illustrate model sensitivity to soil conductivity parameters K_0 and f. We see that larger runoff rates result with lower values of K_0 and higher values of f. When rainfall rate is lower than K_0, runoff rate has a step increase from zero at the time of ponding, that is, when Z_t reaches zero. Note that for the largest values of f

considered, $f = 0.01$ mm^{-1}, and $f = 0.005$ mm^{-1}, runoff is generated in less than 24 hours even with $K_0 = 100$ mm/hr, a value ten times higher than the rainfall rate.

Figures 3.6 and 3.7 summarize cumulative runoff and ponding time, respectively, in 24 hours under a constant rainfall rate of 10 mm/hr, as a function of K_0 and f. Figure 3.6 shows an increase in cumulative runoff with f, and reveals that model sensitivity to K_0 is higher for lower values of f. This results from the fact that if soil conductivity decreases very gradually with depth (low f values), soil conductivity at the wetting front is not very different from surface conductivity, and the rate of infiltration after ponding (i.e., after we have $Z_t = 0$) is close to the surface saturated conductivity K_0. For the same reason, ponding time is also more sensitive to K_0 for high f values, as shown in Figure 3.7.

Figure 3.8 illustrates model sensitivity to rainfall rate R for a soil with $K_0 = 15$ mm/hr. The difference in ponding times for rainfall rates lower than K_0 is to be noted. Figure 3.9 illustrates model sensitivity to the initial recharge rate R_i. Runoff increases with R_i.

Figures 3.10, 3.11 and 3.12 illustrate model sensitivity to porosity parameters θ_s, θ_r and ε, respectively. These parameters are used in the Brooks-Corey parameterization of unsaturated conductivity. Predicted runoff decreases with θ_s and increases with both θ_r and ε.

solid line:	$f = 1 \cdot 10^{-2} \mathrm{mm}^{-1}$
long-dashed line:	$f = 5 \cdot 10^{-3} \mathrm{mm}^{-1}$
dotted line:	$f = 1 \cdot 10^{-3} \mathrm{mm}^{-1}$
dot-dashed line:	$f = 5 \cdot 10^{-4} \mathrm{mm}^{-1}$
short-dashed line:	$f = 1 \cdot 10^{-4} \mathrm{mm}^{-1}$
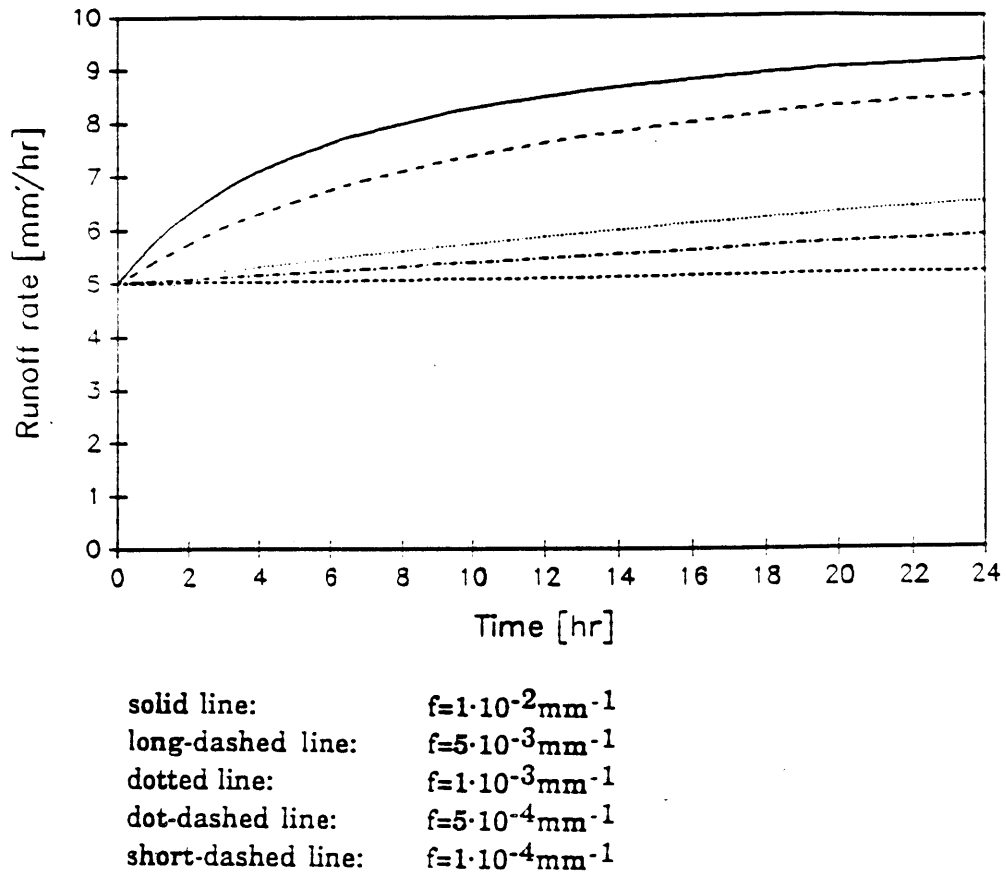
FIGURE 3.1: Sensitivity of the infiltration-excess runoff rate over time to soil conductivity parameter f. Parameters and variables used are $K_0 = 5$ mm/hr, $\theta_s = 0.5$, $\theta_r = 0.05$, $\varepsilon = 4$, $R_i = 0.1$ mm/hr and R = 10 mm/hr.
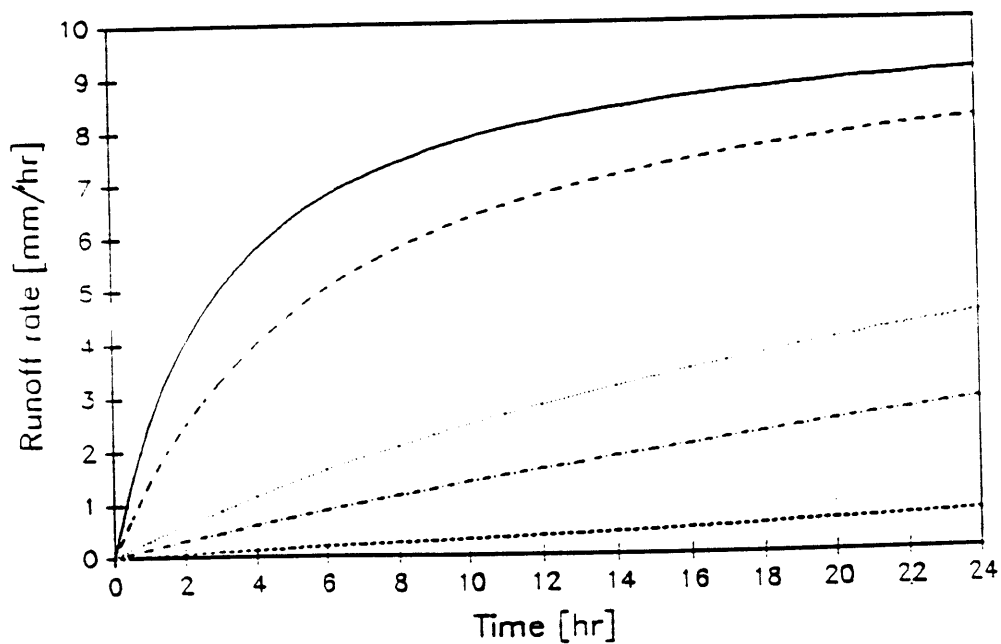
solid line:	$f = 1 \cdot 10^{-2} mm^{-1}$
long-dashed line:	$f = 5 \cdot 10^{-3} mm^{-1}$
dotted line:	$f = 1 \cdot 10^{-3} mm^{-1}$
dot-dashed line:	$f = 5 \cdot 10^{-4} mm^{-1}$
short-dashed line:	$f = 1 \cdot 10^{-4} mm^{-1}$

FIGURE 3.2: Sensitivity of the infiltration-excess runoff rate over time to soil conductivity parameter f. Parameters and variables used are K_0 = 10 mm/hr, θ_s = 0.5, θ_r = 0.05, ε = 4, R_i = 0.1 mm/hr and R = 10 mm/hr.
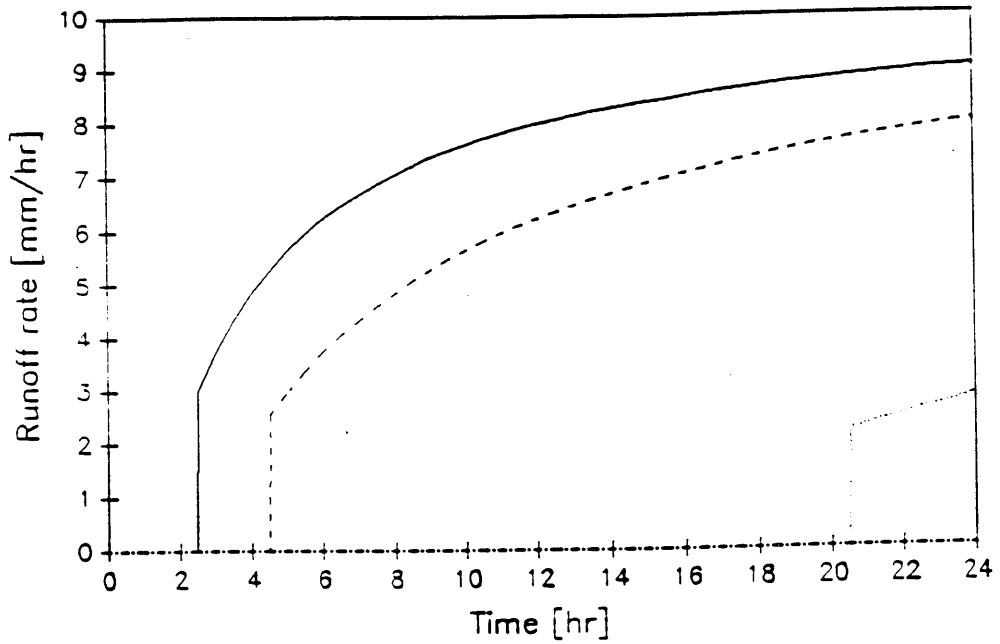
solid line: $f=1 \cdot 10^{-2} mm^{-1}$
long-dashed line: $f=5 \cdot 10^{-3} mm^{-1}$
dotted line: $f=1 \cdot 10^{-3} mm^{-1}$
dot-dashed line: $f=5 \cdot 10^{-4} mm^{-1}$

FIGURE 3.3: Sensitivity of the infiltration-excess runoff rate over time to soil conductivity parameter f. Parameters and variables used are K_0 = 15 mm/hr, θ_s = 0.5, θ_r = 0.05, ε = 4, R_i = 0.1 mm/hr and R = 10 mm/hr.
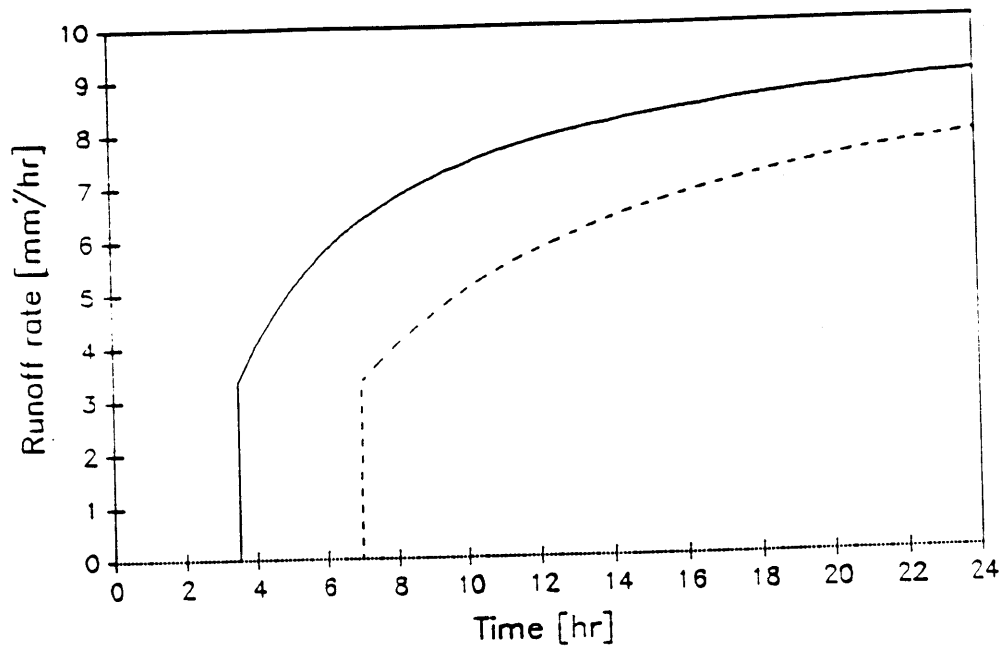
solid line: $f = 1 \cdot 10^{-2} \text{mm}^{-1}$
long-dashed line: $f = 5 \cdot 10^{-3} \text{mm}^{-1}$
dotted line: $f = 1 \cdot 10^{-3} \text{mm}^{-1}$

FIGURE 3.4: Sensitivity of the infiltration-excess runoff rate over time to soil conductivity parameter f. Parameters and variables used are $K_0 = 20$ mm/hr, $\theta_s = 0.5$, $\theta_r = 0.05$, $\varepsilon = 4$, $R_i = 0.1$ mm/hr and R = 10 mm/hr.
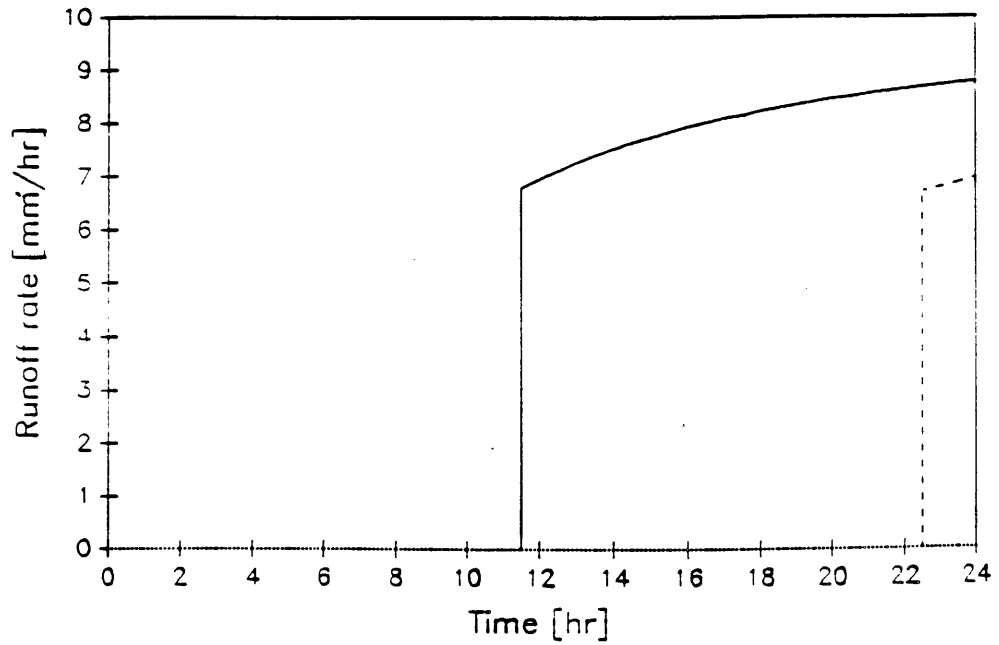
solid line: $f = 1 \cdot 10^{-2} mm^{-1}$
long-dashed line: $f = 5 \cdot 10^{-3} mm^{-1}$
dotted line: $f = 1 \cdot 10^{-3} mm^{-1}$

FIGURE 3.5: Sensitivity of the infiltration-excess runoff rate over time to soil conductivity parameter f. Parameters and variables used are $K_0 = 100$ mm/hr, $\theta_s = 0.5$, $\theta_r = 0.05$, $\varepsilon = 4$, $R_i = 0.1$ mm/hr and $R = 10$ mm/hr.

solid line:	$f=1\cdot10^{-2}\text{mm}^{-1}$
long-dashed line:	$f=5\cdot10^{-3}\text{mm}^{-1}$
dotted line:	$f=1\cdot10^{-3}\text{mm}^{-1}$
dot-dashed line:	$f=5\cdot10^{-4}\text{mm}^{-1}$
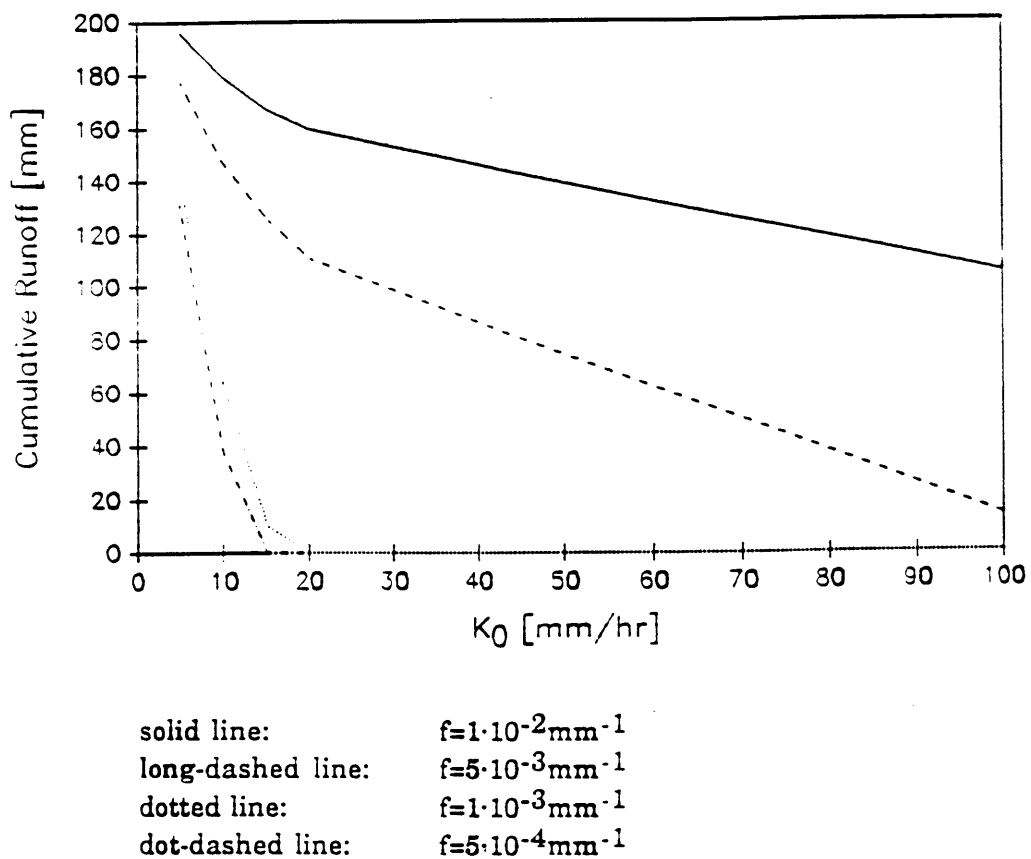
FIGURE 3.6: Sensitivity of the cumulative runoff rate after 24 hours to conductivity parameters K_0 and f. Parameters and variables used are $\theta_s = 0.5$, $\theta_r = 0.05$, $\varepsilon = 4$, $R_i = 0.1$ mm/hr, and R = 10 mm/hr.
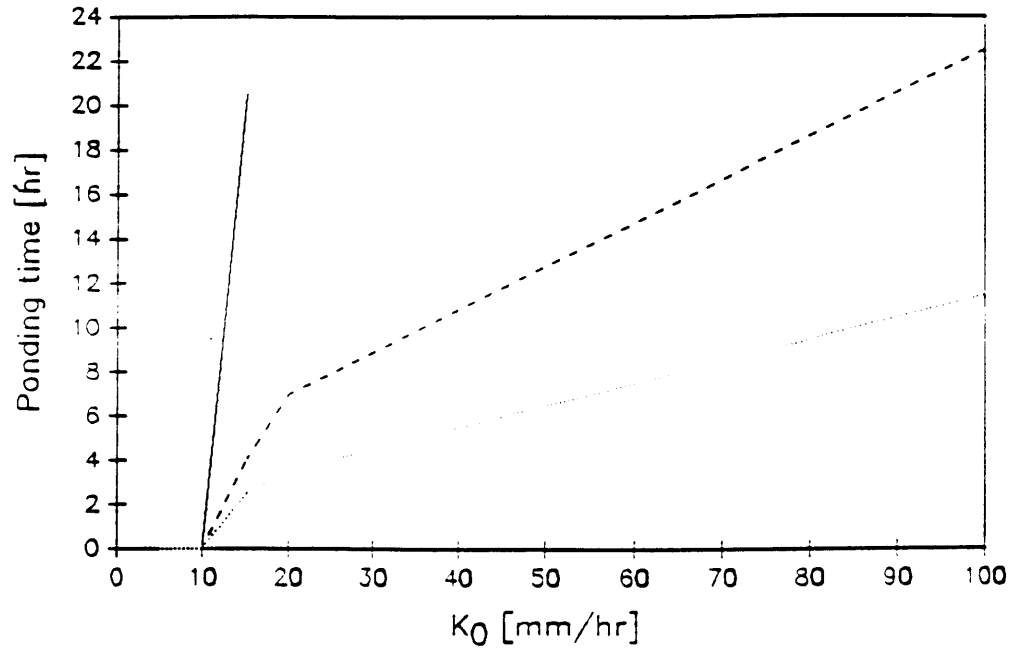
solid line: $f=1 \cdot 10^{-2} mm^{-1}$
long-dashed line: $f=5 \cdot 10^{-3} mm^{-1}$
dotted line: $f=1 \cdot 10^{-3} mm^{-1}$

FIGURE 3.7: Sensitivity of the ponding time to conductivity parameters K_0 and f. Parameters and variables used are $\theta_s = 0.5$, $\theta_r = 0.05$, $\varepsilon = 4$, $R_i = 0.1$ mm/hr, and $R = 10$ mm/hr.
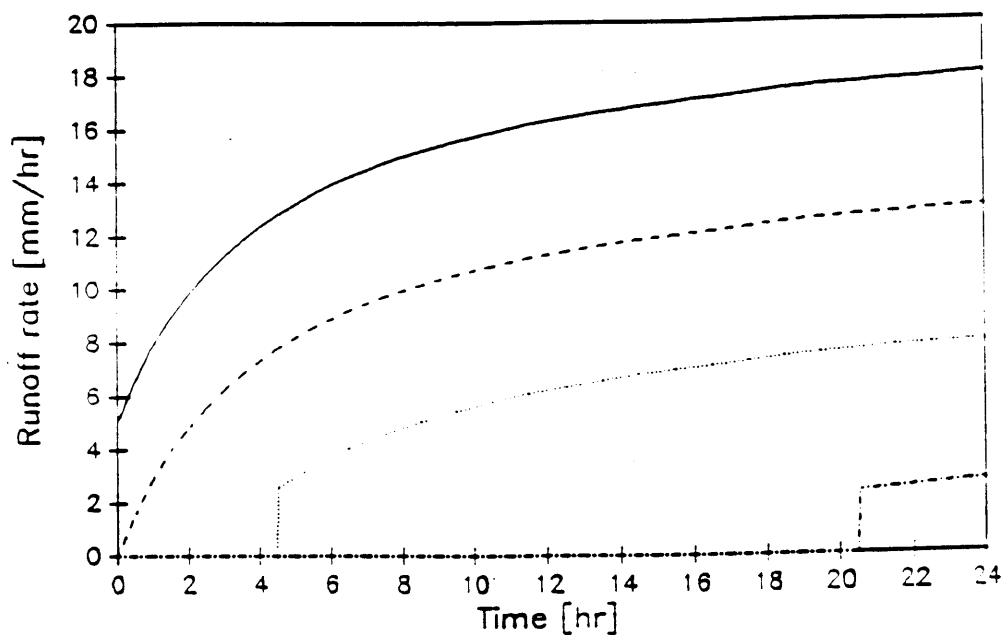
solid line:	R = 20 mm/hr
long-dashed line:	R = 15 mm/hr
dotted line:	R = 10 mm/hr
dot-dashed line:	R = 5 mm/hr

FIGURE 3.8: Sensitivity of the infiltration-excess runoff rate over time to rainfall rate R. Parameters and variables used are K_0 = 15 mm/hr, $f = 10^{-3} mm^{-1}$, $\theta_s = 0.5$, $\theta_r = 0.05$, $\varepsilon = 4$, and $R_i = 0.1$ mm/hr.
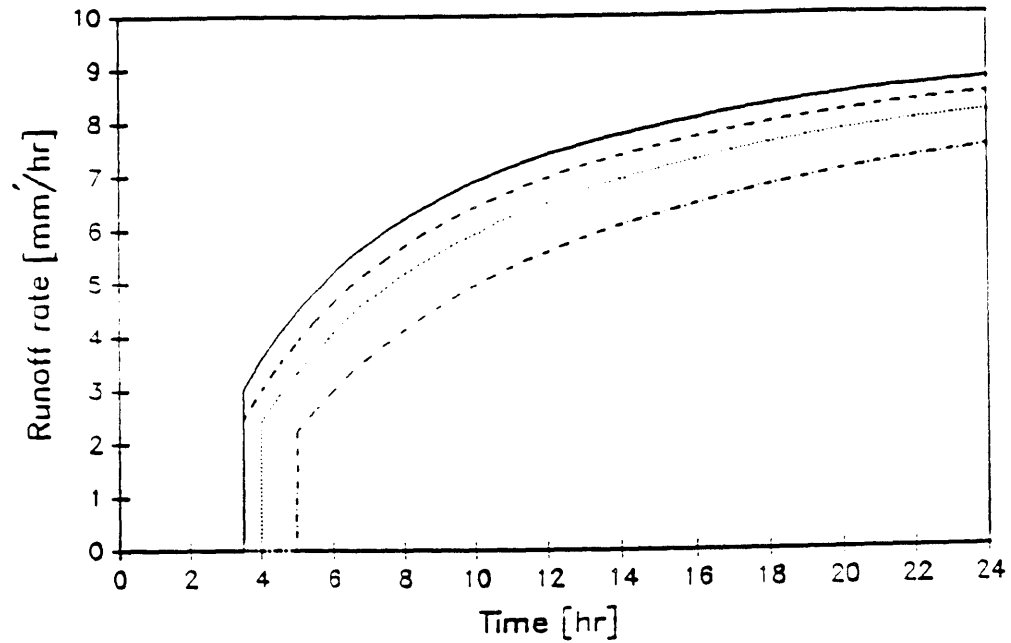
solid line:	R_i = 1.0 mm/hr
long-dashed line:	R_i = 0.5 mm/hr
dotted line:	R_i = 0.1 mm/hr
dot-dashed line:	R_i = 0.01 mm/hr

FIGURE 3.9: Sensitivity of the infiltration-excess runoff rate over time to the initial recharge rate R_i. Parameters and variables used are K_0 = 15 mm/hr, $f = 10^{-3} mm^{-1}$, θ_s = 0.5, θ_r = 0.05, ε = 4, and R = 10 mm/hr.
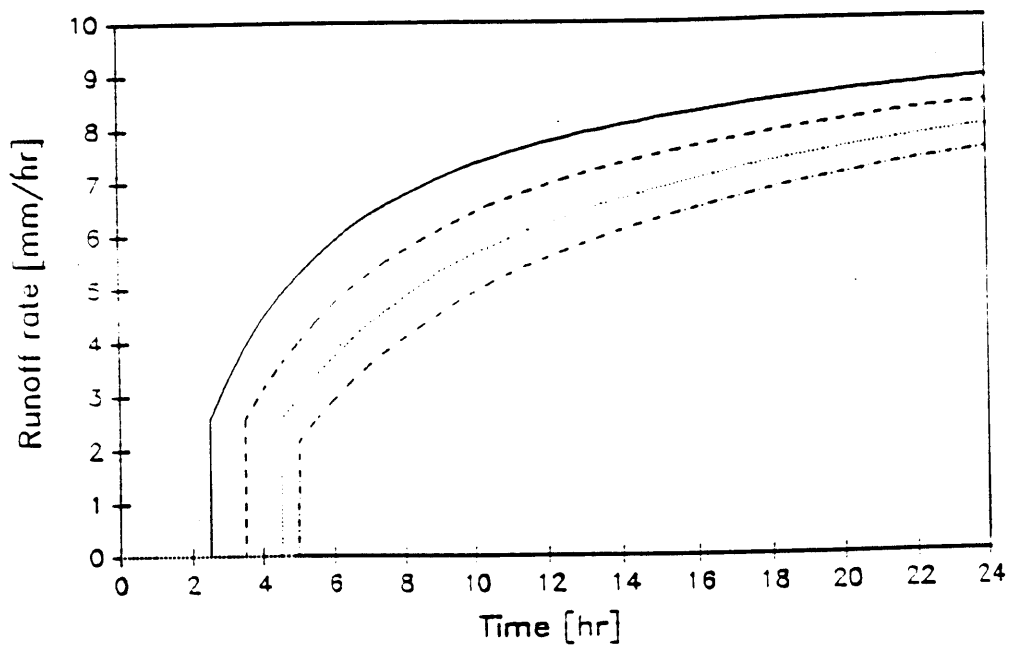
solid line:	θ_s = 0.3 mm/hr
long-dashed line:	θ_s = 0.4 mm/hr
dotted line:	θ_s = 0.5 mm/hr
dot-dashed line:	θ_s = 0.6 mm/hr

FIGURE 3.10: Sensitivity of the infiltration-excess runoff rate over time to the porosity parameter θ_s. Parameters and variables used are K_0 = 15 mm/hr, $f = 10^{-3}mm^{-1}$, θ_r = 0.05, ε = 4, and R = 10 mm/hr.
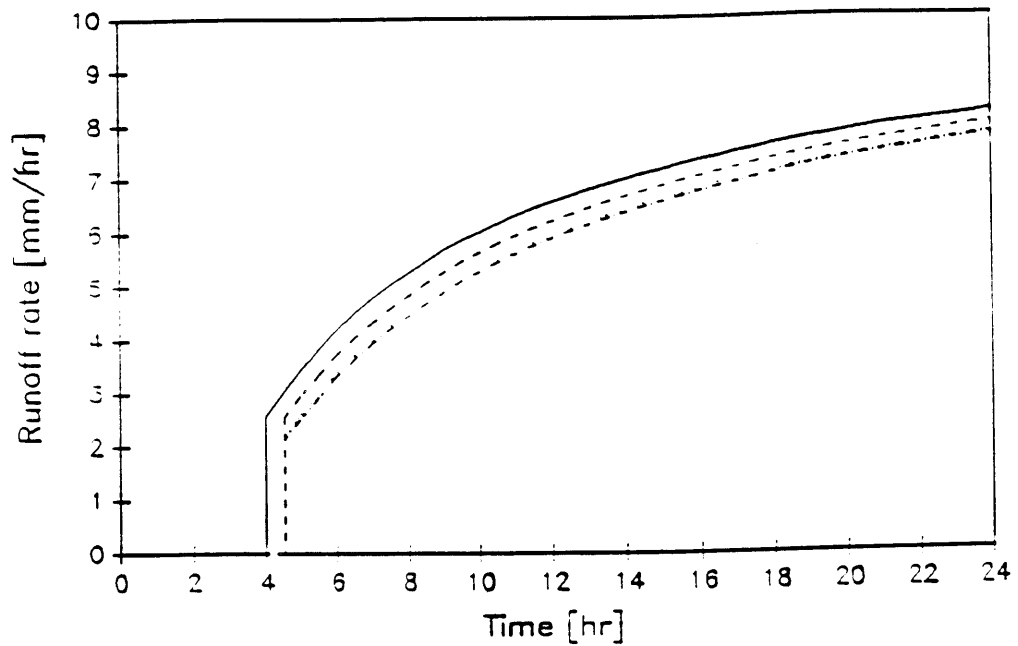
solid line: $\theta_r = 0.1$ mm/hr
long-dashed line: $\theta_r = 0.05$ mm/hr
dotted line: $\theta_r = 0.01$ mm/hr
dot-dashed line: $\theta_r = 0.001$ mm/hr

FIGURE 3.11: Sensitivity of the infiltration-excess runoff rate over time to the porosity parameter θ_r. Parameters and variables used are $K_0 = 15$ mm/hr, $f = 10^{-3}$mm^{-1}, $\theta_s = 0.5$, $\varepsilon = 4$, $R_i = 0.1$ mm/hr, and $R = 10$ mm/hr.
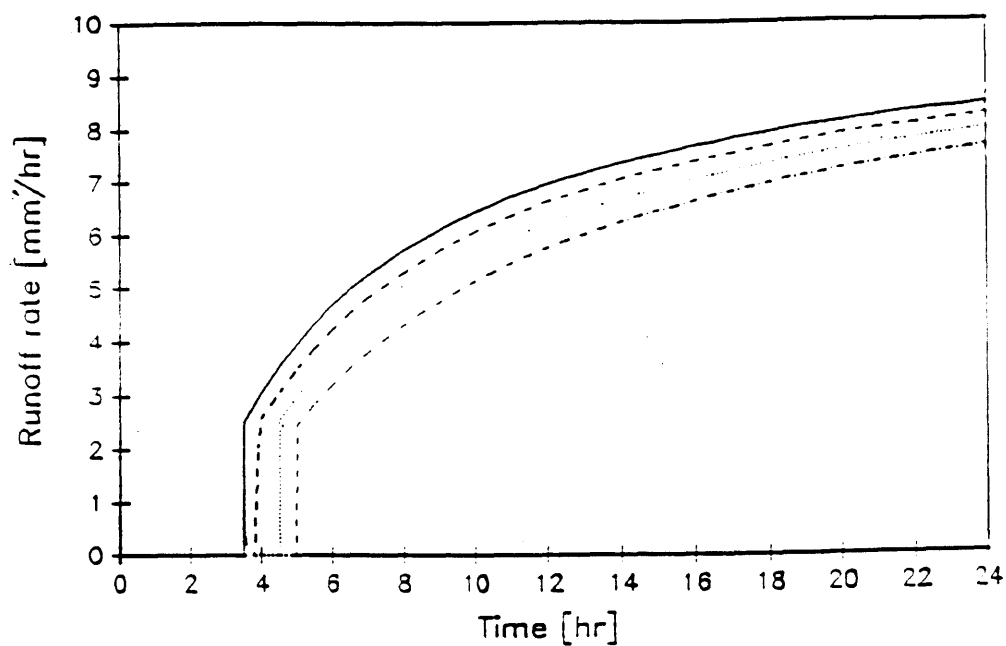
solid line:	$\varepsilon =$	mm/hr
long-dashed line:	$\varepsilon =$	mm/hr
dotted line:	$\varepsilon =$	mm/hr
dot-dashed line:	$\varepsilon =$	mm/hr

FIGURE 3.12: Sensitivity of the infiltration-excess runoff rate over time to soil parameter ε. Parameters and variables used are K_0 = 15 mm/hr, f = 10^{-3}mm^{-1}, θ_s = 0.5, θ_r = 0.05, R_i = 0.1 mm/hr, and R = 10 mm/hr.

ii) Sensitivity of subsurface discharge from one element to soil parameters and terrain inclination

In this section we investigate the sensitivity of lateral subsurface discharge from a hillslope element to soil parameters and terrain slope. We will consider a constant rainfall rate, $R = 10$ mm/hr, and various values of soil parameters K_0 and f.   Table 3.1 summarizes the runs performed and the figure where the corresponding results are presented.

Run	K_0[mm/hr]	f [mm-1]	Figure
1	10	5.10^{-3}	3.13
2	10	1.10^{-3}	3.14
3	10	1.10^{-4}	3.15
4	20	5.10^{-3}	3.16
5	100	5.10^{-3}	3.17

TABLE 3.1: Summary of runs performed to illustrate the sensitivity of subsurface discharge rate to soil conductivity parameters K_0 and f.

Figures 3.13 through 3.17 represent the evolution in time of (a) variables Z_f and Z_t, and (b) rate of subsurface discharge. Subsurface discharge rate is expressed as volumetric discharge rate per unit surface area of soil, i. e. in dimensions [L/T]. In all runs, the highest subsurface discharge rate was obtained with $\alpha = 45°$, which results from the fact that factor $(\cos(\alpha) \cdot \sin(\alpha))$ in Equation (3.3) for Q_{out} has its maximum value at
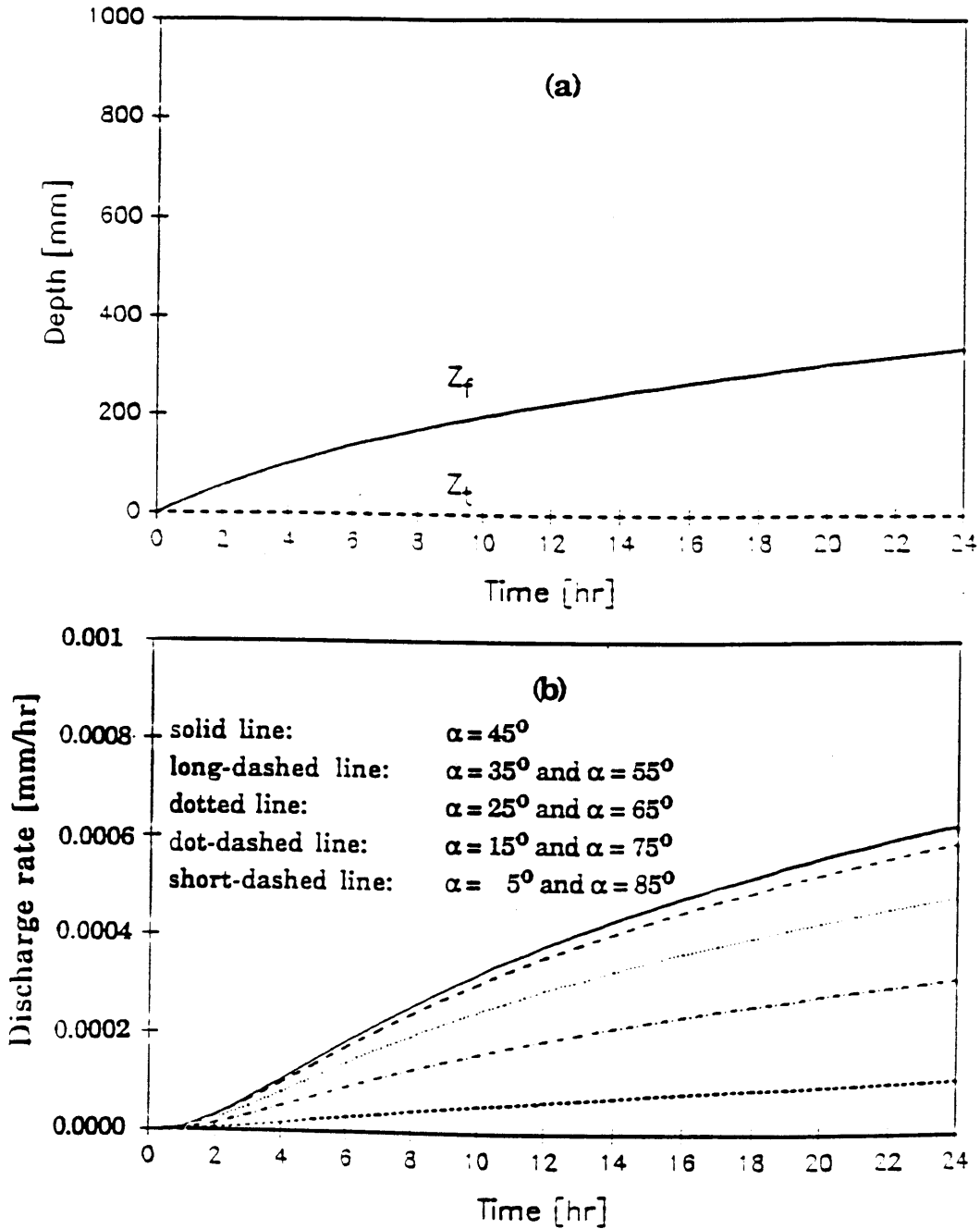
FIGURE 3.13: Evolution in time of (a) variables Z_f and Z_t, and (b) lateral subsurface discharge rate for different values of terrain inclination angle α. Parameters and variables considered are $K_0 = 10$ mm/hr, $f = 5 \cdot 10^{-3}$ mm^{-1}, $\theta_s = 0.5$, $\theta_r = 0.05$, $\varepsilon = 4.0$, $R_i = 0.1$ mm/hr, and $R = 10$ mm/hr.
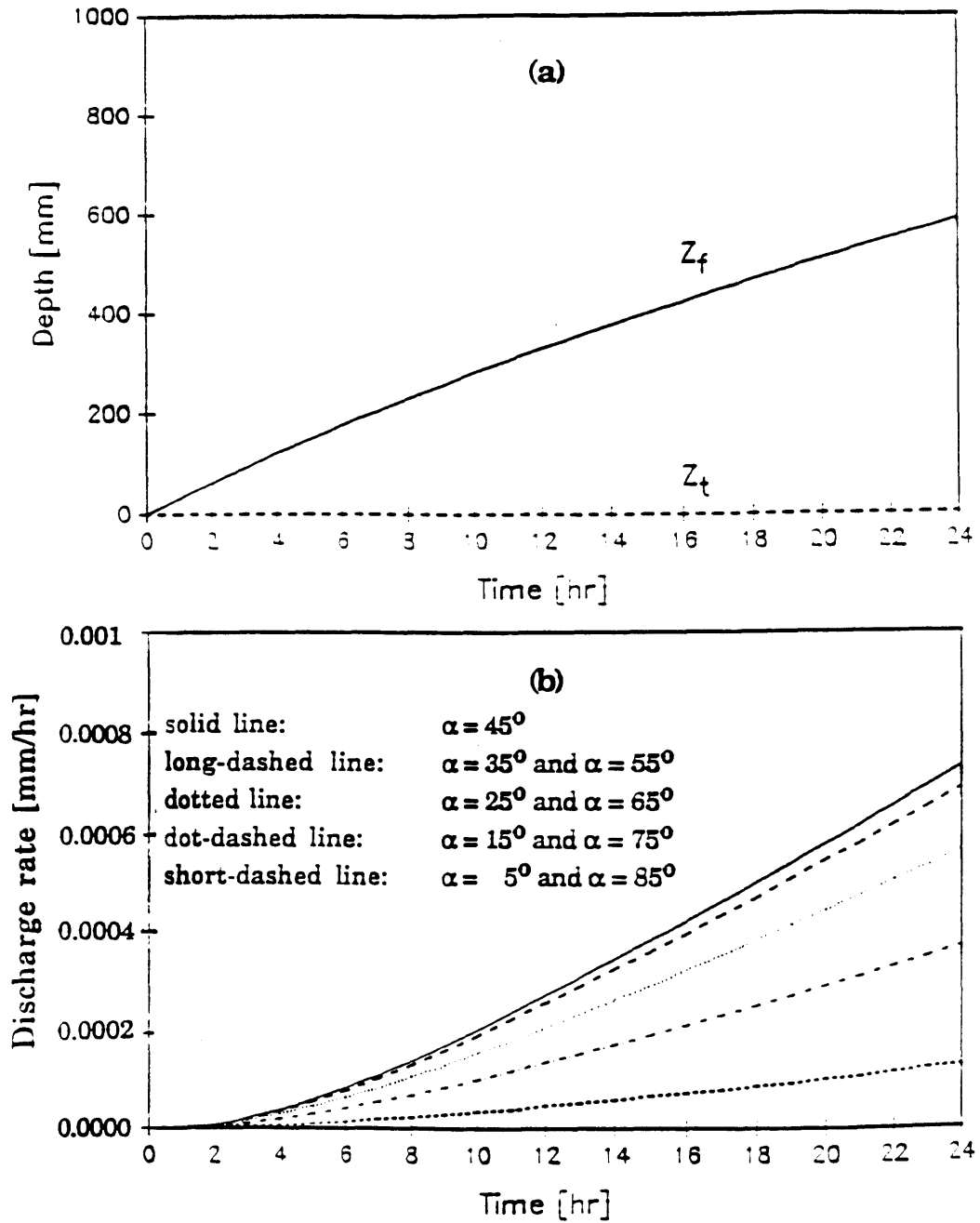
FIGURE 3.14: Evolution in time of (a) variables Z_f and Z_t, and (b) lateral subsurface discharge rate for different values of terrain inclination angle α. Parameters and variables considered are $K_0 = 10$ mm/hr, $f = 1 \cdot 10^{-3}$ mm^{-1}, $\theta_s = 0.5$, $\theta_r = 0.05$, $\varepsilon = 4.0$, $R_i = 0.1$ mm/hr, and $R = 10$ mm/hr.
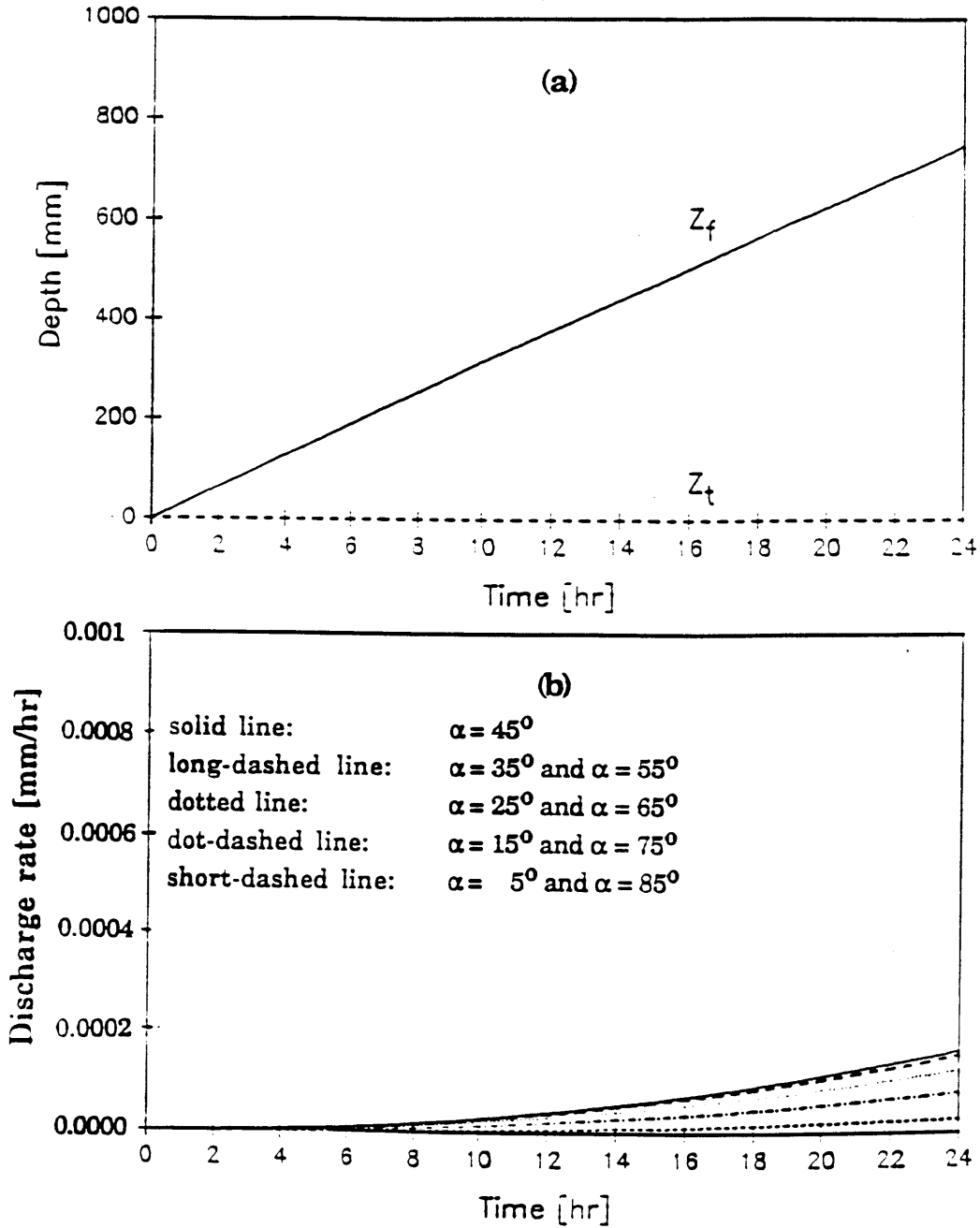
FIGURE 3.15: Evolution in time of (a) variables Z_f and Z_t, and (b) lateral subsurface discharge rate for different values of terrain inclination angle α. Parameters and variables considered are K_0 = 10 mm/hr, f = $1 \cdot 10^{-4}$ mm^{-1}, θ_s = 0.5, θ_r = 0.05, ε = 4.0, R_i = 0.1 mm/hr, and R = 10 mm/hr.
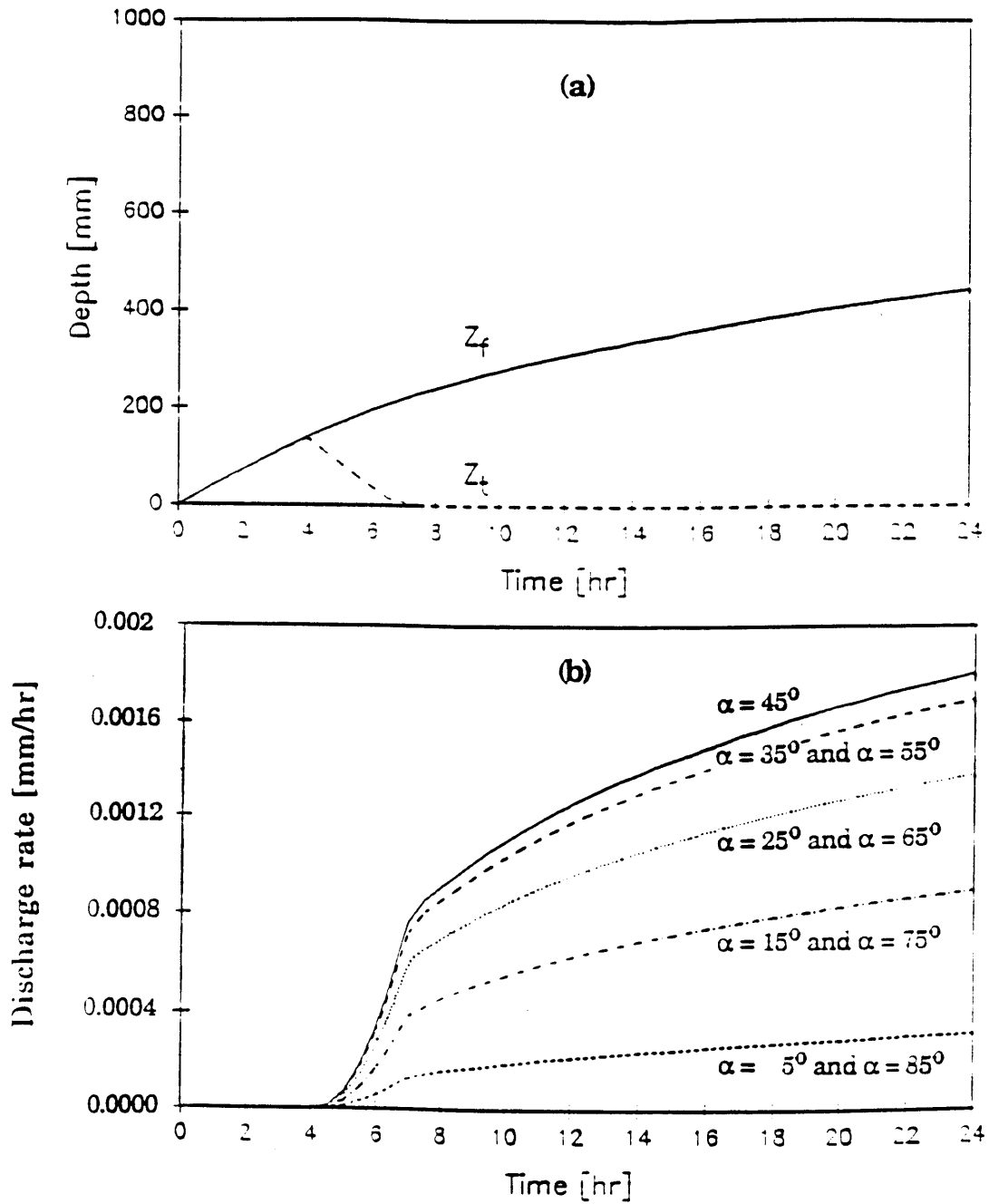
FIGURE 3.16: Evolution in time of (a) variables Z_f and Z_t, and (b) lateral subsurface discharge rate for different values of terrain inclination angle α. Parameters and variables considered are $K_0 = 20$ mm/hr, $f = 5 \cdot 10^{-3}$ mm^{-1}, $\theta_s = 0.5$, $\theta_r = 0.05$, $\varepsilon = 4.0$, $R_i = 0.1$ mm/hr, and $R = 10$ mm/hr.
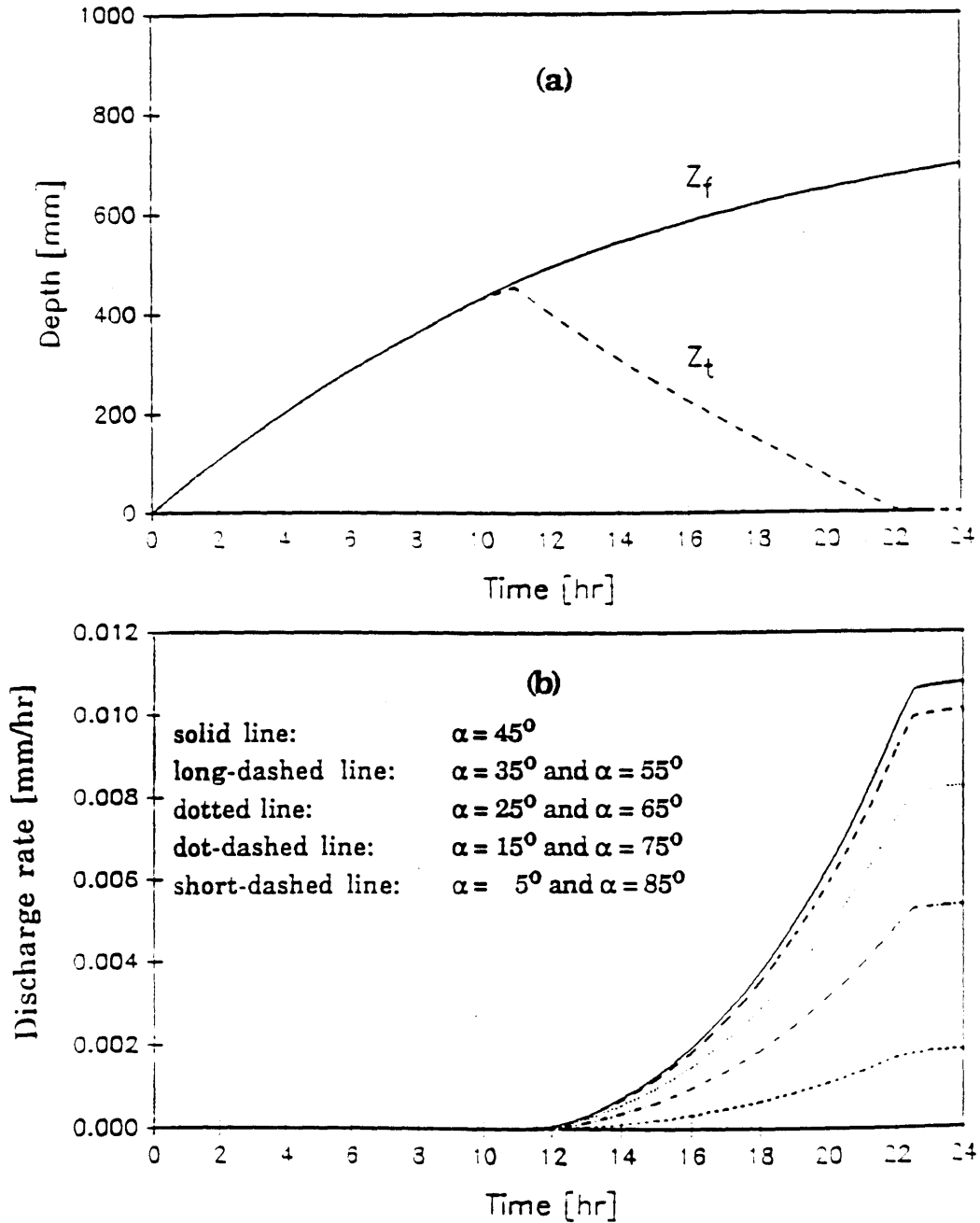
FIGURE 3.17: Evolution in time of (a) variables Z_f and Z_t, and (b) lateral subsurface discharge rate for different values of terrain inclination angle α. Parameters and variables considered are $K_0 = 100$ mm/hr, $f = 5 \cdot 10^{-3}$ mm^{-1}, $\theta_s = 0.5$, $\theta_r = 0.05$, $\varepsilon = 4.0$, $R_i = 0.1$ mm/hr, and $R = 10$ mm/hr.

$\alpha = 45^\circ$. The split between the curves for Z_t and Z_f (which occurs at $Z^*(R)$, given in Equation (2.15)), indicates the development of a zone of perched saturation. For $K_0 \leq R$ (runs 1, 2 and 3), Z_t equals zero from the time of initiation of rainfall. For $K_0 > R$ (runs 4 and 5), perched saturation develops only after some time of continued rainfall. Once saturation has developed within the soil, lateral subsurface discharge is initiated.

Comparison of runs 1, 2 and 3 (Figures 3.13, 3.14 and 3.15) show sensitivity of subsurface discharge rate to parameter f. The relation between subsurface discharge rate and parameter f is nonlinear, as is apparent from Equation (3.3) for Q_{out}. Note that in (3.3) Z_f and Z_t are also determined by f (see equations of evolution for these variables, summarized in Section 3.B). The lateral discharge rate is initially higher for $f = 5 \cdot 10^{-3}$ mm^{-1} than for $f = 1 \cdot 10^{-3}$ mm^{-1} (Figures 3.13 and 3.14), but after approximately 20 hours of rainfall (for $\alpha = 45^\circ$), the opposite is true. Subsurface discharge rate for $f = 1 \cdot 10^{-4}$ mm^{-1} is much lower than that for $1 \cdot 10^{-3}$ mm^{-1} within 24 hours.

Comparison of runs 1, 4 and 5 (Figures 3.13, 3.16 and 3.17) shows sensitivity of lateral subsurface discharge to conductivity parameter K_0 (note the different vertical scales in the three plots). For $K_0 = 20$ mm/hr and $K_0 = 100$ mm/hr ($K_0 > R$), subsurface discharge is initiated only after perched saturation has developed, i. e. when Z_f reaches $Z^*(R)$. Subsurface discharge rate increases in time as the perched saturation zone grows. The curve of subsurface discharge rate is initially concave but becomes convex, with the inflection point occurring at the ponding time ($Z_t = 0$).

It is important to note the small magnitude of the values of lateral subsurface discharge rate relative to the rainfall rate, $R = 10$ mm/hr. The highest subsurface discharge rate in 24 hours was obtained in run 5 for α

106

= 45° (Figure 3.17) and this is only approximately 0.01 mm/hr, that is 1,000 times smaller than the rainfall rate. Therefore, we should expect lateral subsurface flows during a rainfall event to have very little influence in determining ponding times and infiltration-excess runoff generation on a hillslope. We must keep in mind, however, that this is under the assumption of isotropic soils. This may not be the case when lateral hydraulic conductivities are higher than vertical ones (see Appendix A).

3.F.2 SENSITIVITY OF SATURATION-EXCESS RUNOFF TO HILLSLOPE MORPHOLOGY

The saturation-excess runoff mechanism is determined by water-table elevations; where the water-table is at the soil surface (waterlogged areas), direct runoff occurs. The procedure used to estimate the position of the water-table is described in Section 3.D. Here we investigate sensitivity of estimated water-table elevations to conductivity parameters K_0 and f, and to recharge rate R_i. For the purpose of illustration, we will use the DEM of the Sieve basin in Italy, and will assign to this basin different parameters and recharge rate values. These values are fictitious and are used only for illustration purposes. In Chapter 4, the model is applied to the Sieve basin using estimated real parameters. Table 3.2 summarizes the illustration runs performed and the results obtained.

We see that the percentage of basin saturation at steady-state is the same in runs 1, 5 and 8; in runs 2 and 6; and in runs 4 and 7. Runs 5 has a conductivity 10 times smaller than run 1 but an f parameter that is 10

107

times smaller as well. Therefore, the total saturated transmissivity of the soil column, which is approximated by K_0/f (see Section 3.D), is the same in the two runs. The result of same transmissivity is a similar position of the steady-state water-table. Run 8 has a value of f that is 10 times larger than that in run 1. However, the recharge rate considered is also 10 times larger, and the result is a similar position of the steady-state water-table. The similarities of water-tables for runs 2 and 6, and runs 4 and 7 has the same explanation. We conclude that the extent of the saturated areas is constant for constant values of the ratios K_0/f, K_0/Ri and R_i/f.

Run	K_0 [mm/hr]	f [mm^{-1}]	R_i [mm/hr]	% Saturation
1	100	10^{-2}	0.01	95.6
2	100	10^{-3}	0.01	40.8
3	100	10^{-4}	0.01	25.3
4	10	10^{-2}	0.01	99.3
5	10	10^{-3}	0.01	95.6
6	10	10^{-4}	0.01	40.8
7	100	10^{-2}	0.1	99.3
8	100	10^{-3}	0.1	95.6
9	100	10^{-4}	0.1	40.8

TABLE 3.2: Summary of runs performed to illustrate sensitivity of water-table position and the extent of saturated areas to hillslope morphology.

Figures 3.18, 3.19, and 3.20 represent water-table depth for runs 1, 2 and 3, respectively.
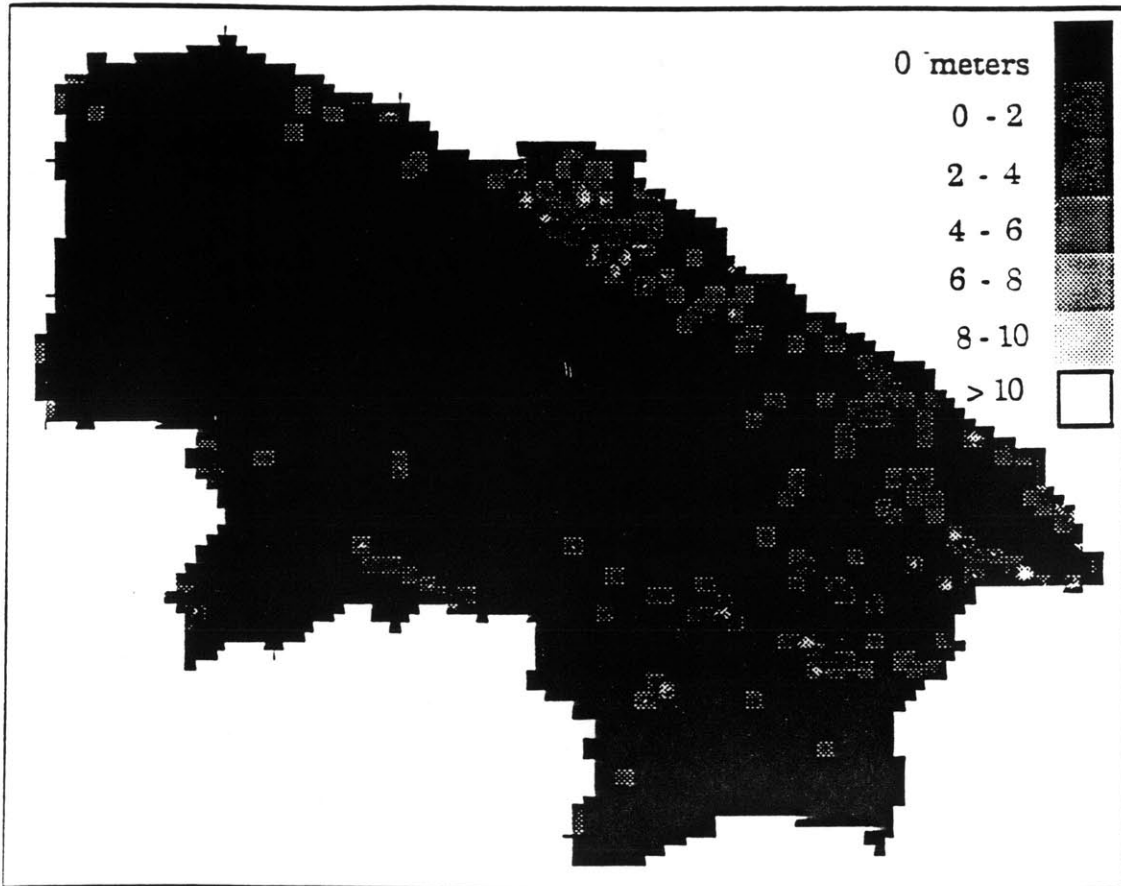
FIGURE 3.18: Map of depths (meters) below the surface of the water-table in steady-state with the recharge rate $R_i = 0.01$, for soil parameters $K_0 = 100$ mm/hr and $f = 10^{-2}$ mm^{-1}.
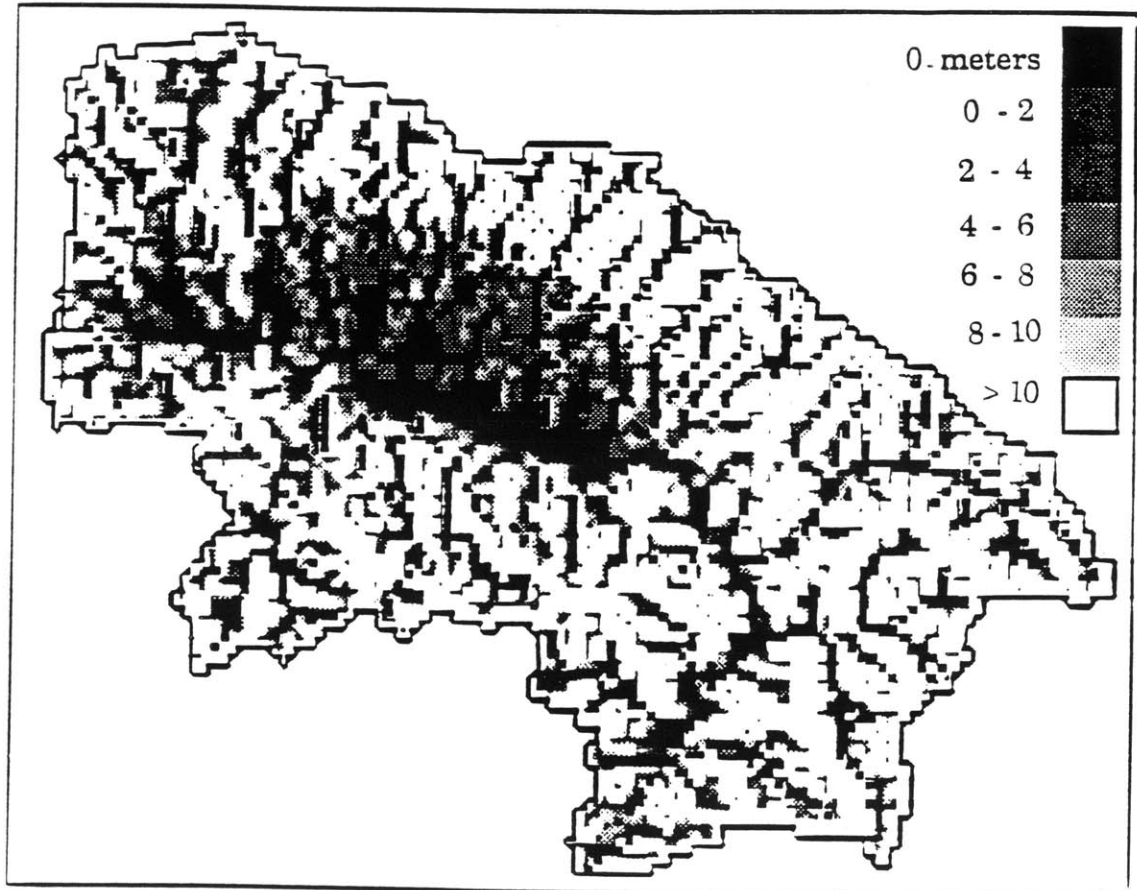
FIGURE 3.19: Map of depths (meters) below the surface of the water-table in steady-state with the recharge rate R_i = 0.01, for soil parameters K_0 = 100 mm/hr and $f = 10^{-3}$ mm^{-1}.
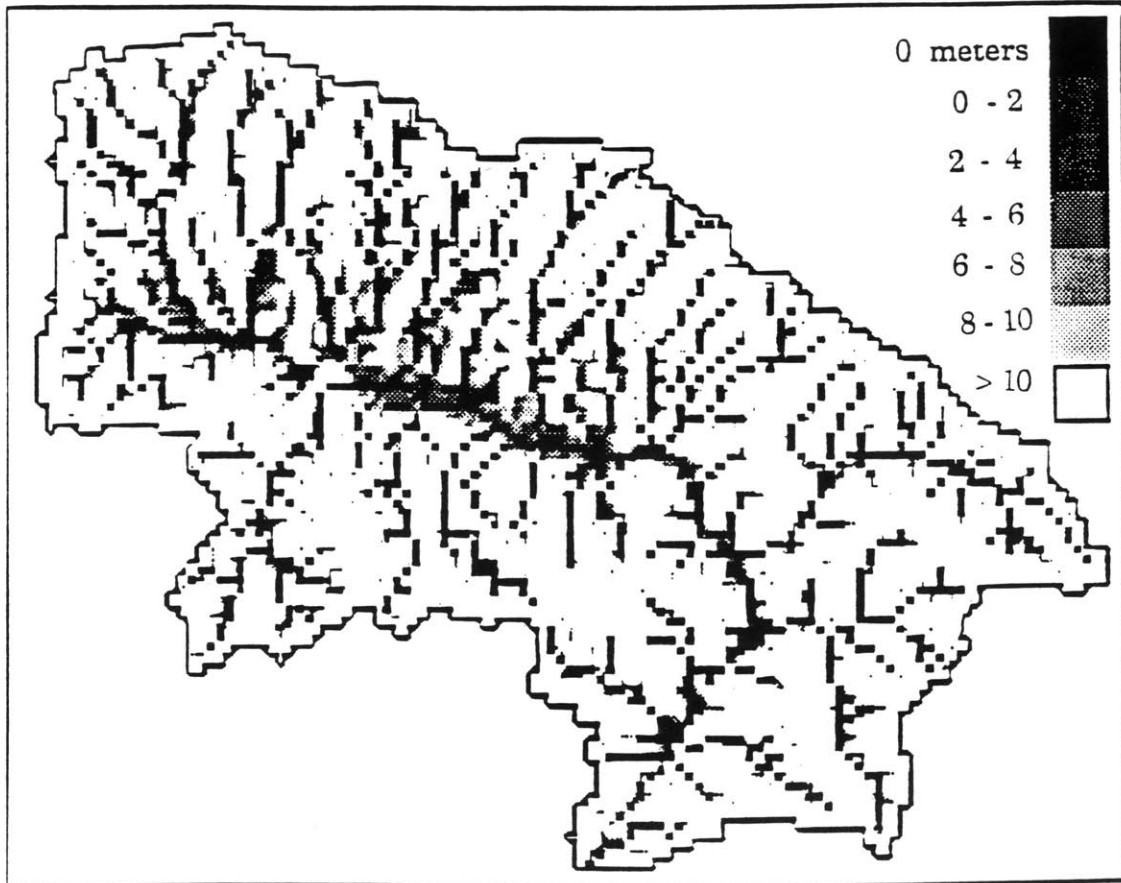
FIGURE 3.20: Map of depths (meters) below the surface of the water-table in steady-state with the recharge rate $R_i = 0.01$, for soil parameters $K_0 = 100$ mm/hr and $f = 10^{-4}$ mm^{-1}.

3.F.3 CALIBRATION OF CONDUCTIVITY PARAMETER f

Parameter f is the rate of exponential decrease with depth of the saturated hydraulic conductivity, as expressed by the soil parameterization equation repeated below as Equation (3.8),

$$K(z) = K_0 \cdot e^{-f \cdot z} \qquad (3.8)$$

Beven (1982) summarized the results of fitting Equation (3.8) to a variety of soils whose conductivity had been measured over depth by different researchers. The values of f providing the best fit to the various soils ranged from 10^{-3} mm^{-1} to 10^{-2} mm^{-1}.

In the usual situation, however, such studies are not available, especially if the catchment in question is large and includes a great variety of soil types. In that situation, soil parameterization must be made based on assumptions. In absence of field measurements, we assume that a single value of f represents all soil types in the basin. Figure (4.7) in Chapter 4 shows simulated basin discharge over time starting at full saturation, for various values of f, in the model application to the Arno River catchment. We see from this Figure that the maximum discharge from the basin varies approximately linearly with f. This is explained by the fact that the transmissivity of a soil with conductivity given by Equation (3.8) is approximated by K_0/f (see Section 3.D), and therefore discharge, Q_{out}, from a saturated element of slope $\tan(\alpha)$ is approximated by

$$Q_{out} = \tan(\alpha) \cdot \frac{K_0}{f} \qquad (3.9)$$

If the range of basin baseflow values is known (as usually is, or can be estimated from typical regional values), then an important physical basis imposes an upper limit on the value of f. The value of f must be such that the maximum baseflow obtained by the groundwater model be equal or higher than the maximum baseflow observed in the basin. However, if we have reason to believe that the soil parameterization given by Equation (2.12) applies only to a limited soil depth rather than to the entire soil profile, then the groundwater model cannot be used to predict the initial water-table profile. The water-table position, and the extent of the zone of saturated soil, must then be estimated through field measurements. In this case, parameter f can be obtained by calibration with observed flows.

Chapter 4

MODEL RESULTS: APPLICATION TO THE SIEVE RIVER BASIN

This chapter presents the application of the rainfall-runoff model to the Sieve River basin in the Tuscany Region, Italy. The hydro-geophysical characteristics of the Sieve are reviewed in Section 4.A. Section 4.B describes the pertinent data available for the basin and data processing. Calibration of conductivity parameter f and routing parameters V_s and V_o is dealt with in Sections 4.C and 4.D. Finally, in Section 4.E we present results of predicted basin response for observed storms.

The Sieve basin has an area of approximately 840 Km^2 and is one of the major sub-basins of the Arno catchment (8,000 Km^2). The Arno River crosses the cities of Florence and Pisa and has produced severe flooding of these two cities in the past, endangering their populations and raising both national and international concern for the preservation of the artistic and historical patrimony of Florence. This concern has led to the creation of the *Arno Project*, which aims at developing a monitoring system of hydraulic variables over the Arno basin which will increase lead time of hydrologic forecasting for the Arno. The technologies considered for the monitoring system include telemetering ground sensor networks, a meteorological radar, airborne and satellite sensors, and telemetering streamgages. It is expected that such technologies be implemented in the near future. The new distributed information that will thus be made available should be fully utilized by a distributed rainfall-runoff model

such as the one presented here. As we will see, we have encountered data limitations in our model application to the Sieve which hopefully will be reduced in the future.

4.A THE SIEVE RIVER BASIN

The Sieve basin is bordered to the North-East by the Appennine mountains, with a point of maximum elevation at Falterona mountain (1657 meters above sea level); to the North and West it is bordered by a series of mountain ranges of peak elevations of 800 to 900 meters. The average elevation of the basin is 470 meters above sea level. The basin has moderate to strong relief, as is apparent from the three-dimensional view given in Figure 4.1. The confluence of the Sieve with the main course of the Arno is located 19 Km upstream from the city of Florence. The basin has approximately 63,000 inhabitants (1971).

Due to its exposure and high elevation, the Sieve basin is subject to intense orographic precipitation events, as a result of the interception of the dominant winds coming from the Mediterranean Sea. It is a characteristic of the Mediterranean climate that the rain season coincides with the cold season. This situation is particularly propitious to the generation of high runoff volumes, given that the lower evaporation rates in the Winter result in high levels of soil saturation and in reduced infiltration.

Monthly precipitation varies widely throughout the year, with maximums in October-November and in February, and minimum flows in
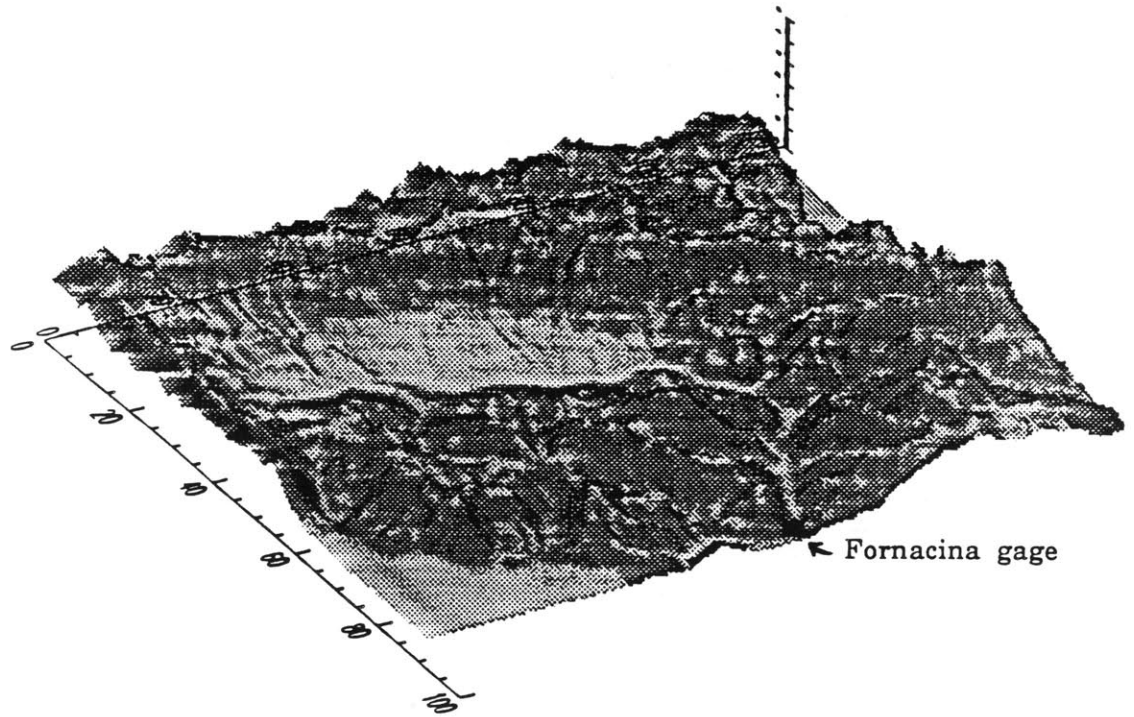
FIGURE 4.1: Aspect of the topography of the Sieve basin, obtained from the DEM.

116

July and October. February is characterized by the highest amplitude of observed values of precipitation. In some years, February will be among the months with maximum yearly precipitation, in other years among those with minimum precipitation.

Table 4.1 shows the probability distribution (values with exceedence probability of 10%, 50%, and 90%) of monthly minimum flows, in cubic meters per second, observed at Fornacina.

4.B DATA AVAILABLE FOR THE SIEVE BASIN

This section summarizes the data available for the Sieve basin; the characteristics of the digital elevation map, soils data, river stage data; and rainfall data.

4.B.1 DIGITAL ELEVATION MAP

The DEM available for the Sieve basin has a square grid, 400 meters to the side, with elevation given in integer meters, with North-South and East-West coordinates. The DEM was provided by the Italian Military Geographic Institute (IGMI), and was obtained through the IGMI standard procedure of digitalization of contours of 25 meters interval from a topographic map at the scale of 1:25,000, utilizing an electronic raster scanner (A. Carrara *et al.*, 1987). The IGMI procedure consists of

117

month	P=90%	P=50%	P=10%	Maxim.
Jan	3.0	7.5	15.0	22.6
Feb	3.0	9.0	17.0	20.5
Mar	4.0	7.0	21.0	24.0
Apr	2.5	6.5	14.5	20.0
May	3.0	5.5	9.5	14.5
Jun	1.0	3.5	5.0	10.0
Jul	0.5	1.0	2.5	3.0
Aug	0.4	0.9	1.5	2.0
Sep	0.5	0.9	1.5	2.0
Oct	0.5	1.0	4.0	5.5
Nov	1.0	4.0	10.0	18.5
Dec	2.0	7.0	15.5	25.0

TABLE 4.1 : Distribution of monthly minimum flows (in m^3/s) at Fornacina. P represents the probability of exceedence. The column on the right indicates maximum observed values.

overlying the square grid on the topographic map and identifying the *points of intersection* of the grid lines with the topographic contours. Lines of maximum slope are obtained by connecting these intersection points, and finally an elevation value is assigned to each grid cell by interpolation between the maximum slope lines (E. Caporali, 1988). This procedure of DEM acquisition is subject to a variety of errors, associated with the approximations inherent to the establishment of the lines of maximum slope, rounding errors, and operator errors. However, a limited number of validation studies have been made, comparing digitized and observed elevations, indicating a maximum error of ± 3 meters (E. Caporali, 1988).

The resolution of 400 meters seems lower than desirable for appropriate representation of terrain morphology, given the marked relief of the basin. We expect that at this resolution terrain slopes computed from the DEM underestimate true slopes. Also, given the grid size, automatic generation of the channel network is not able to reproduce the high density found for the digitized network.

The DEM was processed to obtain estimated distributed terrain slopes and an automatically-generated channel network. The algorithms used for both purposes were developed by Tarboton (see Tarboton, 1989).

Extraction of a channel network from the DEM requires a threshold contributing area. The most appropriate threshold to use depends on the DEM grid size, the observed drainage density, and the purpose for which the extracted network will be used. Figure 4.2 represents the map-digitized stream network of the Sieve basin. It is apparent that the detail and high density of this network cannot be reproduced by the 400 meter grid. In fact, the large grid spacing of the DEM represents the most important limitation to network density. Carlá *et al.* (1986), working with
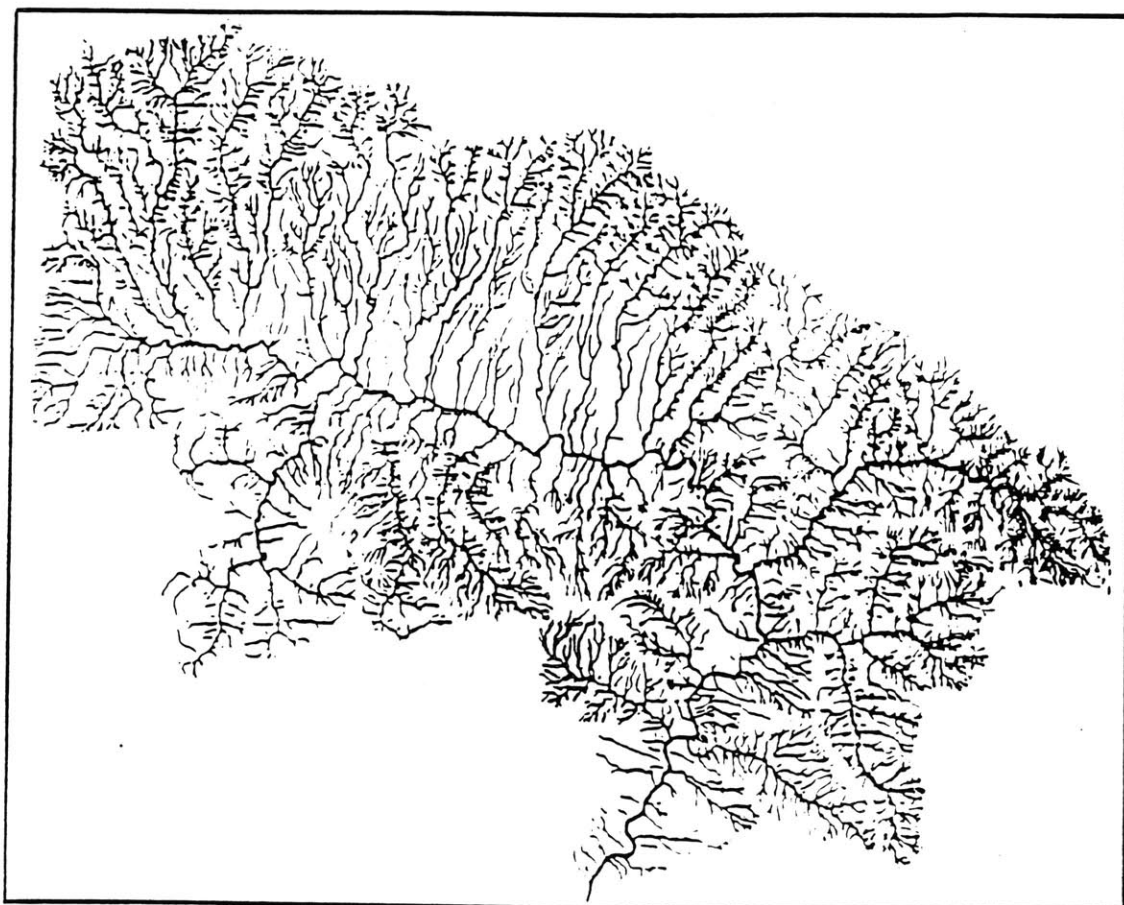
FIGURE 4.2: Channel network obtained from digitalization of map blue lines.

the same DEM for the Sieve, found that a threshold area corresponding to 8 elements (1.28 K^2) produced a network which compares very favorably with that represented in maps at the scale of 1:200,000. We have adopted the threshold value of 8 elements based on Carlá's findings. The corresponding channel network is represented in Figure 4.3. This network has 1084 stream elements (the total number of elements in Figure 4.2 is 5252). The drainage density (average length of channel per unit basin area) of the generated network is 0.52 Km/Km^2. The drainage density obtained from mapped blue lines is 13.2 Km/Km^2 (Carlá *et al.*, 1986). Again, we can not expect to reproduce observed drainage density with the 400 m grid. The maximum Strahler order is IV. Table 4.2 represents the number and length of channels by Strahler order.

Strahler order	Number of channels	Length of channels [Km]
I	63	253
II	14	87
III	2	38
IV	1	17

TABLE 4.2: Number and length of channels by Strahler order, obtained from the 400m DEM for the Sieve basin using a threshold contributing area of 1.28 Km^2 (8 elements).
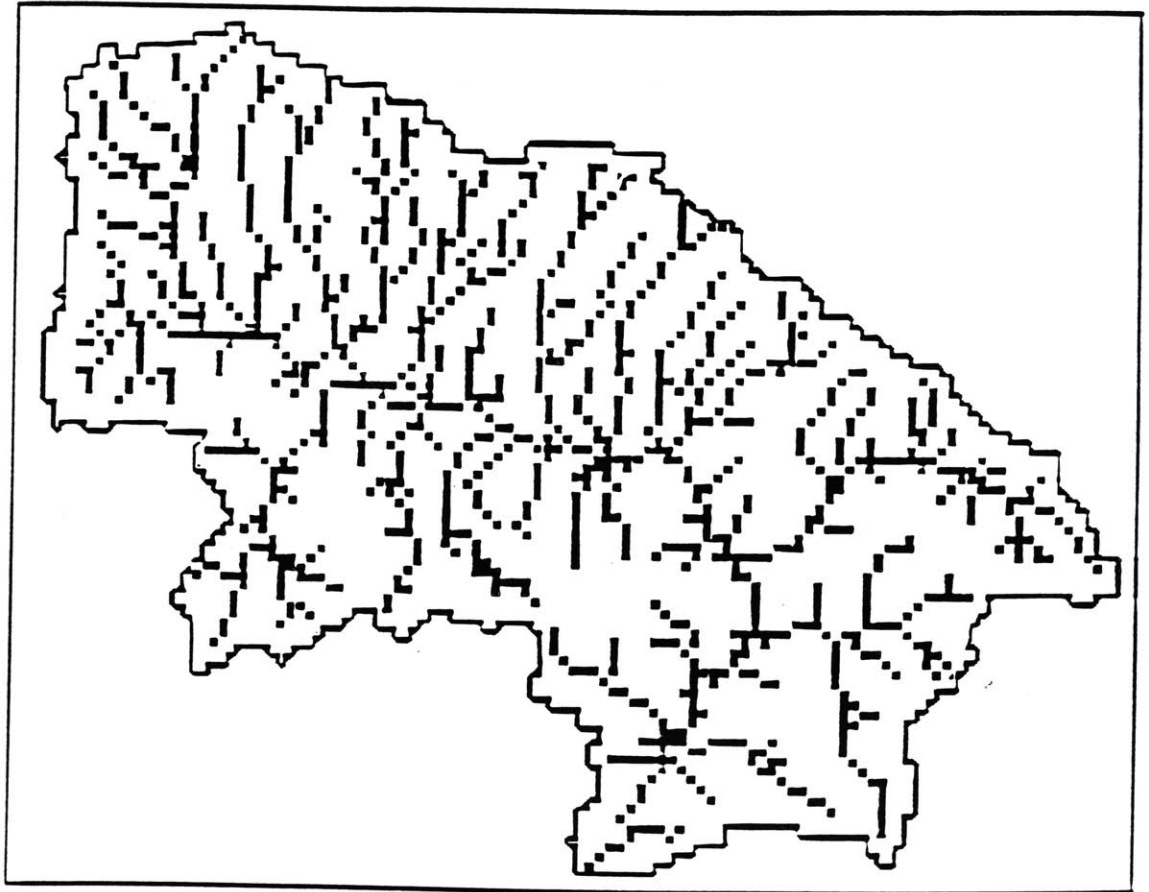
FIGURE 4.3: Channel network generated from the 400 meter grid DEM, using a threshold area equal to 8 elements (1.28 Km^2).

4.B.2 SOILS DATA

No field measurements of soil parameters are available for the Sieve. However, a map of soil types exists from which estimated physical parameters were derived based on measurements conducted for similar soils in other basins in the region, and based on typical parameter values by soil type provided in hydrology literature. The map of soil types is represented in Figure 4.4 .

Ranges of values of saturated conductivity of the topsoil were derived from measurements conducted with soils of assumed similar type and characteristics from basins in the same region. The ranges of conductivity values is large, varying over two orders of magnitude. We will use these values, described as topsoil saturated conductivity, as estimates for our conductivity parameter K_0. Given the ranges of values provided, we will take the median value from each range to represent our best estimate of K_0 for a given soil type. The range of conductivity values provided and the resulting estimate of K_0 are given in Table 4.3 .

Estimated values of total porosity were also obtained from field studies conducted on similar soils. We will take these values as our best estimates for parameter θ_s in the Brooks-Corey parameterization. For parameters θ_r (residual porosity) and ε (pore-size distribution parameter) in the same parameterization equation, we will adopt values indicated in hydrology literature as frequent in each soil textural type (Bear, 1972, Entekhabi, 1988). The parameter values used are summarized in Table 4.3.

0017
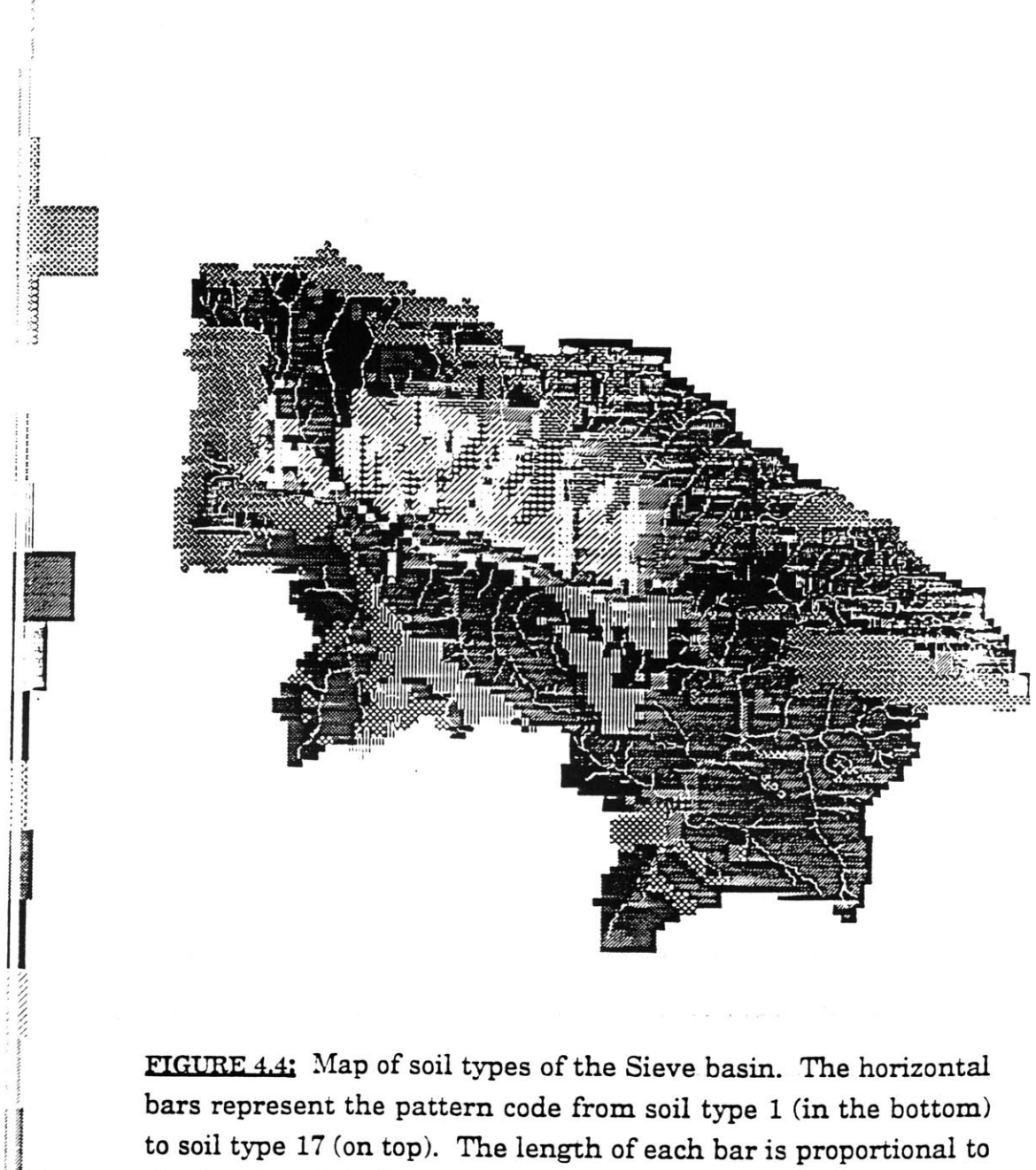
FIGURE 4.4: Map of soil types of the Sieve basin. The horizontal bars represent the pattern code from soil type 1 (in the bottom) to soil type 17 (on top). The length of each bar is proportional to the fraction of the basin represented by the respective soil type.

0001

Soil Type #	Texture Class	K [mm/hr]	K_0 [mm/hr]	θ_s	θ_r	ε
1	FS-FLA	2 - 41	21.5	0.53	0.02	3.6
2	FL-FA	0.2 - 7	3.6	0.52	0.04	3.6
3	A	0.01 - 0.5	0.25	0.48	0.09	7.5
4	A	0.01 - 0.5	0.25	0.48	0.09	7.5
5	FA	20 - 70	45	0.56	0.11	3.6
6	A	1 - 50	25.5	0.56	0.09	7.5
7	FL-FLA	0.2 - 7	3.6	0.53	0.11	3.6
8	FL	0.2 - 10	5.1	0.49	0.11	3.6
9	F-FA	0.2 - 33	16.6	0.52	0.06	3.5
10	FS	2.7 - 41	21.8	0.48	0.04	3.4
11	FS-FA	0.2 - 41	20.6	0.52	0.07	3.6
12	FS-FA	0.2 - 41	20.6	0.52	0.07	3.6
13	FS-FA	0.2 - 41	20.6	0.52	0.07	3.6
14	F-FS-FA-FL	0.2 - 41	20.6	0.50	0.07	3.6
15	F-FS	2.7 - 41	21.8	0.49	0.03	3.5
16	FS	2.7 - 41	21.8	0.48	0.041	3.6
17	Detritic	40	40	0.25	0.02	3.4

TABLE 4.3 : Summary of soil types and parameters used in the model.

4.B.3 RIVER STAGE DATA

The Sieve river is gaged at Fornacina, a location near the confluence of the Sieve with the main course of the Arno river. Stage recording is not continuous in time; it is initiated manually some time after the onset of a rainstorm event perceived by the operator to be important. Therefore, existing stage records are of short duration and do not cover inter-storm periods. A stage curve exists for the Fornacina gage which allowed conversion of stage readings to flow rates.

4.B.4 RAINFALL DATA

Rainfall measurements at intervals of 20 minutes are available for the period from 1968 to 1985, for four raingages located inside or in the vicinity of the Sieve basin. The Thiessen polygons corresponding to each of these raingages are represented in Figure 4.5 . We see that one gage, Borgo S. Lorenzo, covers approximately 75% of the basin area. The available rainfall record therefore does not provide the spatial resolution necessary to take best advantage of distributed rainfall-runoff modeling.

The rainfall record contains several gaps which reduce the number of storms for which we have both stage and rainfall data to be used for calibration runs.

Hourly rainfall records with higher spatial resolution are available for 3 rainfall events; of November of 1987, December of 1981, and February
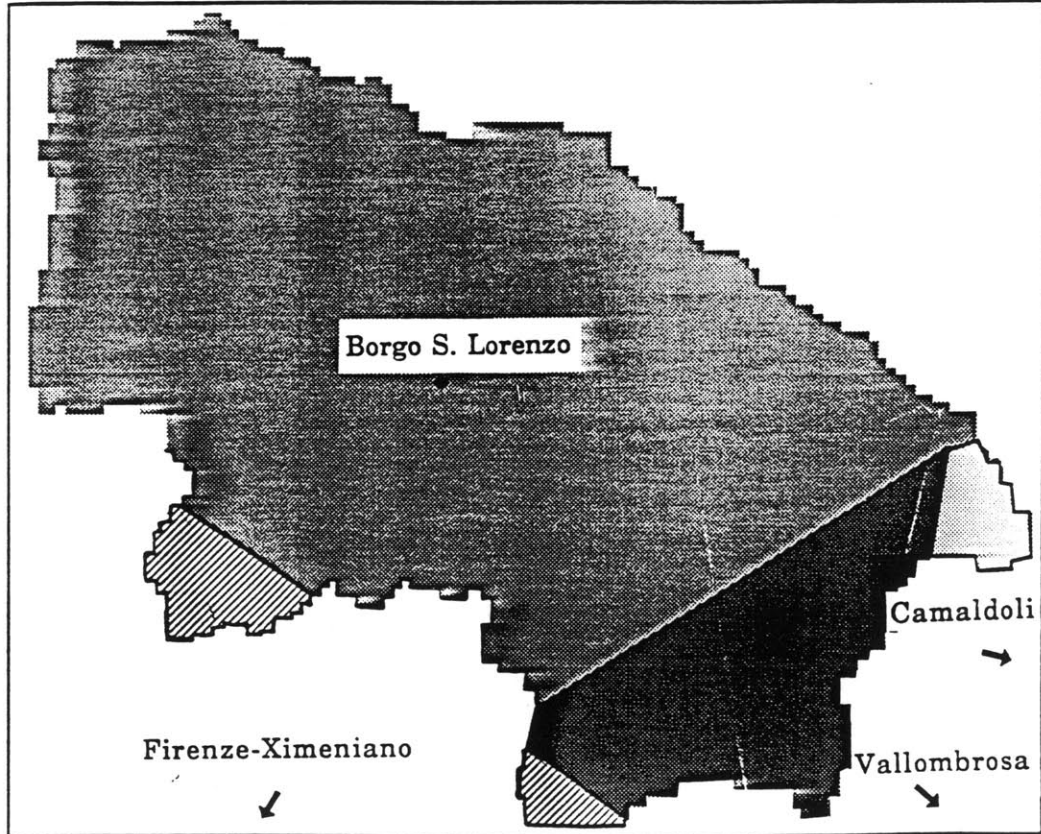
FIGURE 4.5: Thiessen polygons corresponding to the 4 raingages that recorded most rainfall events. Only one raingage is located inside the Sieve basin.

of 1968. The storm of November of 1987 was recorded by 7 raingages. The corresponding Thiessen polygons are represented in Figure 4.6. The storms of October of 1981 and February of 1968 were recorded by 6 raingages; the same as the storm of November of 1987, except for the gage of Vetta Le Croci.

4.C CALIBRATION OF CONDUCTIVITY PARAMETER f

A uniform value of f will be used throughout the basin, given that we do not have information on soil depth for the different soil types. Table 4.1 above gives the distribution of monthly minimum flow values. The values with an exceedence probability of 50% are interpreted as representing basin baseflow, i. e. as not including any component of direct runoff. These baseflow values vary from 0.9 to 9.0 m^3/s.

Figure 4.7 represents the discharge curves corresponding to various values of f, using the estimated values of surface conductivity and porosity parameters in Table 4.3. The runs represented in the figure were initiated at full saturation of the basin (with the groundwater coinciding with the terrain surface), and the initial discharge corresponds to the maximum discharge allowed by the value of f used. We see that the values of f smaller than 10^{-4} mm^{-1} do not provide groundwater discharges comparable to the observed 50% exceedence-probability minimum monthly flows of the Winter months. Even at full saturation of the basin, the groundwater discharge obtained with f = 10^{-3} mm^{-1} was approximately ten

1	Ponte a Olmo
2	Calenzano
3	Borgo S. Lorenzo
	Vetta Le Croci
5	Villore
6	Nave di Rosano
	Consuma
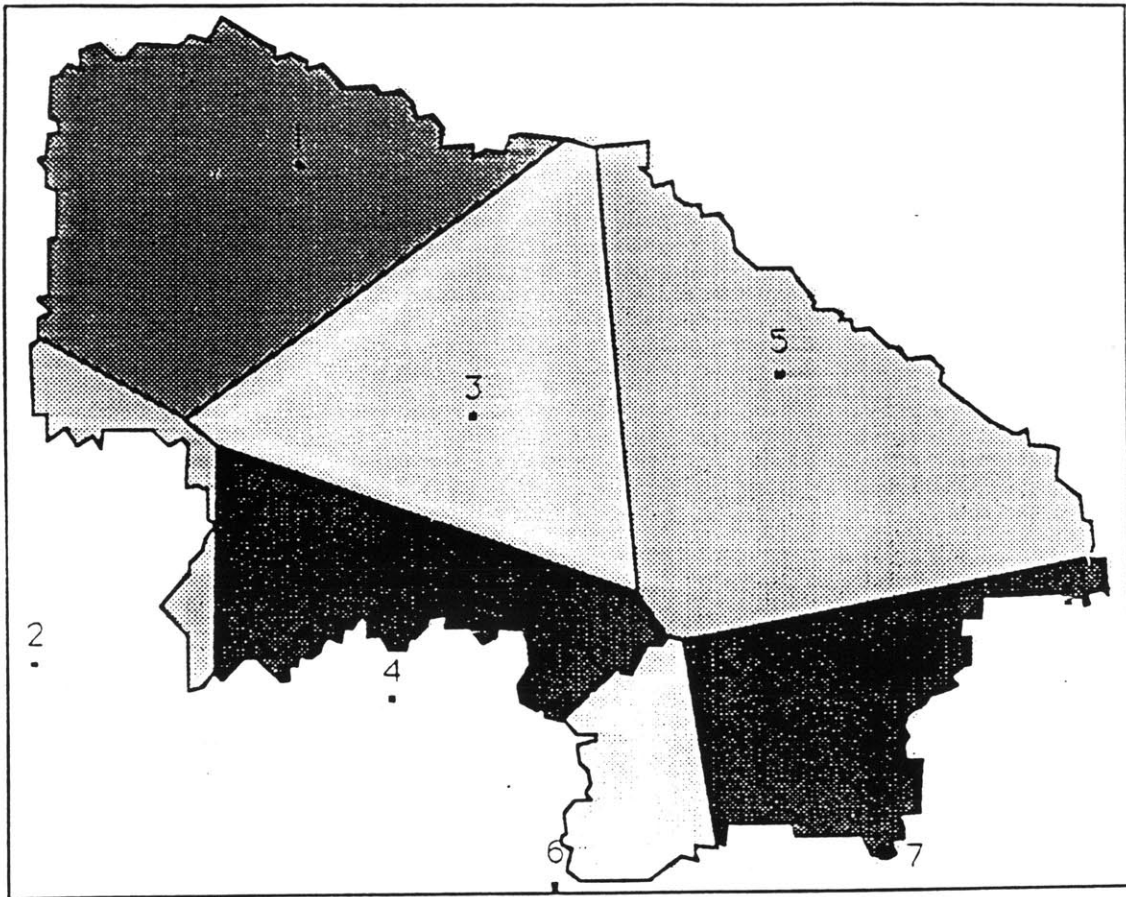
FIGURE 4.6: Thiessen polygons corresponding to the raingages that recorded the event of November, 1987.
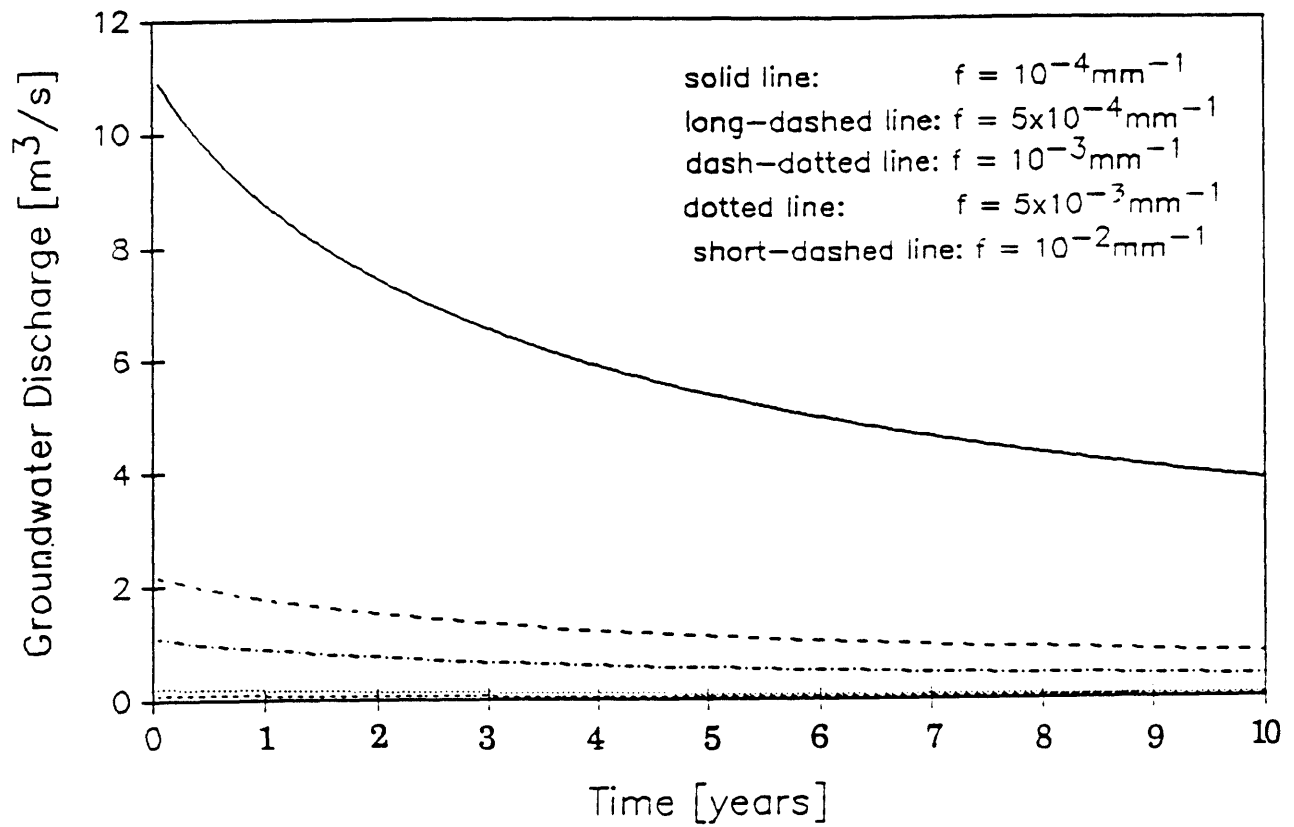
FIGURE 4.7: Curves of predicted groundwater discharge from the Sieve basin for various values of parameter f.

times smaller than the 50% exceedence probability minimum flow for the month of February.

Only the value $f = 10^{-4}$ mm^{-1} can account for basin baseflow at full saturation of the basin (at time zero). Therefore, if we assume the soils to be isotropic, we must not choose a value of f smaller than 10^{-4} mm^{-1}. For this reason, we chose the value **$f = 10^{-4}$ mm^{-1}**, a very small value but which represents a maximum established by the observed baseflow values.

It should be noted that if we considered the soil to be anisotropic, with conductivity in the direction parallel to the surface higher than in the direction normal to the surface according to an anisotropy ratio a_r (see Appendix A), then the same discharge at full saturation would be obtained for a value of $f a_r$ times larger than 10^{-4} mm^{-1}. As an example, in Figure 4.8 we show the discharge curve for $f = 10^{-3}$ mm^{-1} and $a_r = 10$. Discharge at time zero, when the basin is fully saturated, is the same for $f = 10^{-3}$ mm^{-1} and $a_r = 10$ as for $f = 10^{-4}$ mm^{-1} and $a_r = 0$. However, the time rate of decay of the discharge is higher for the anisotropic soil.

We did not consider anisotropy for the soils of the Sieve given that no data are available on this characteristic. An anisotropy ratio could of course be obtained through calibration of model results, but that calibration would be interdependent with that for parameter f. The resulting degrees of freedom in parameter fitting would result in little physical meaning for parameters f and a_r.
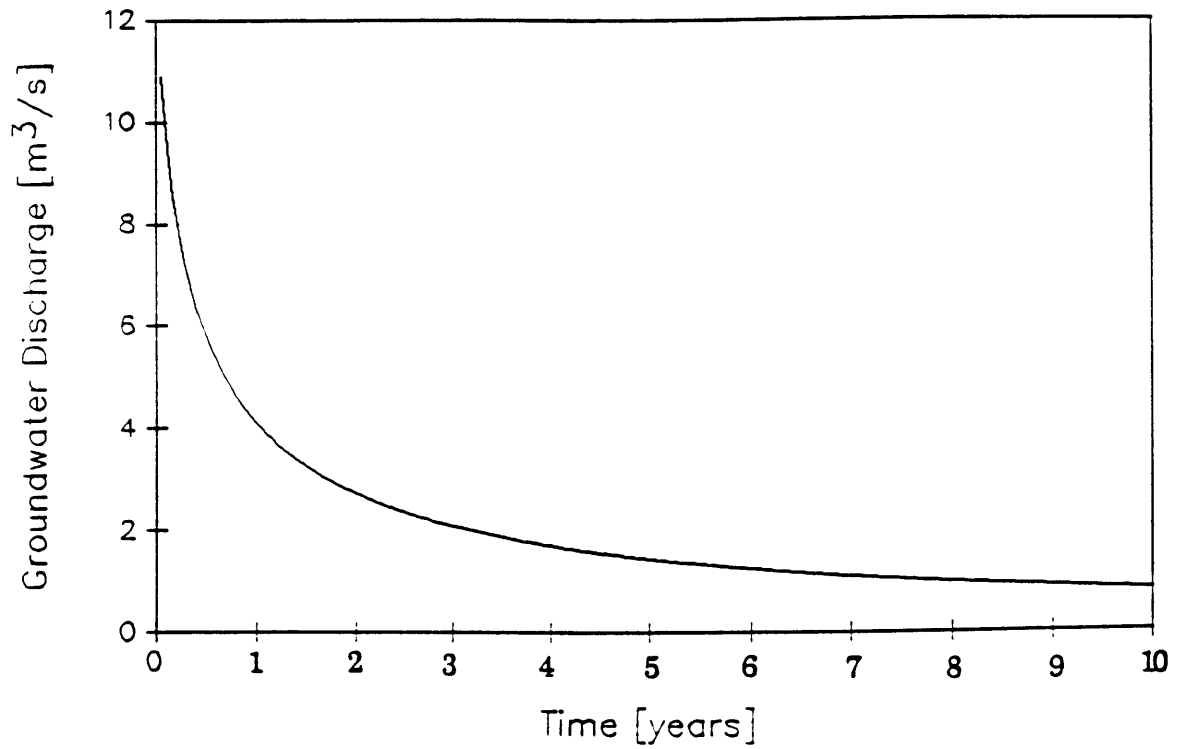
FIGURE 4.8: Curve of predicted groundwater discharge from the Sieve basin for f = 10^{-3} mm^{-1} and an soil anisotropy ratio of a_r=10.

4.D CALIBRATION OF ROUTING PARAMETERS V_S AND V_0

We saw in Section 3.E that routing parameters V_s and V_0 represent the velocities of streamflow and overland flow, respectively, assumed independent of flow levels and spatially uniform. We used various values of these two parameters and in different combinations, to obtain predicted hydrographs for the calibration storms. The best combinations of V_s and V_0 values for each storm are summarized in Table 4.4. To illustrate the sensitivity of results to the two routing parameters, we present in Figure 4.9 the predicted hydrographs obtained for different values of V_s and V_0 for the storm of December, 1981.

In general, the sensitivity of results to routing parameter V_0 was very small for values higher than 0.4 Km/hr. With V_0 lower than 0.4 Km/hr, however, hydrograph dispersion would increase markedly, with the shape and peak intensity not being preserved. For this reason, we considered **V_0 = 0.4 Km/hr** to be an appropriate value. For the stream velocity, **V_s = 6.0 Km/hr** is the most frequent value providing the best fit.

4.E RESULTS FOR OBSERVED STORMS

The calibrated parameter values that we will use are V_s = 6.0 Km/hr, V_0 = 0.4 Km/hr, and f = 10^{-4} mm^{-1}. In this section we present the predicted hydrographs for twelve observed rainfall events in the Sieve basin.

Storm	V_s [Km/hr]	V_o [Km/hr]
Feb 1968	6.0	0.4
Dec 1968	6.0	0.4
Jan 1969	6.0	0.4
Dec 1975	6.0	0.2
Dec 1976	5.5	0.4
Feb 1977	7.0	0.4
Jan 1979	6.0	0.3
Dec 1981	8.0	0.4
Nov 1982	4.0	0.4
Feb 1983	6.0	0.4
Jan 1985	5.0	0.4
Nov 1987	5.5	0.4

TABLE 4.4: Velocity parameters providing the best fit between predicted and observed hydrographs at Fornacina for the rainfall events indicated.
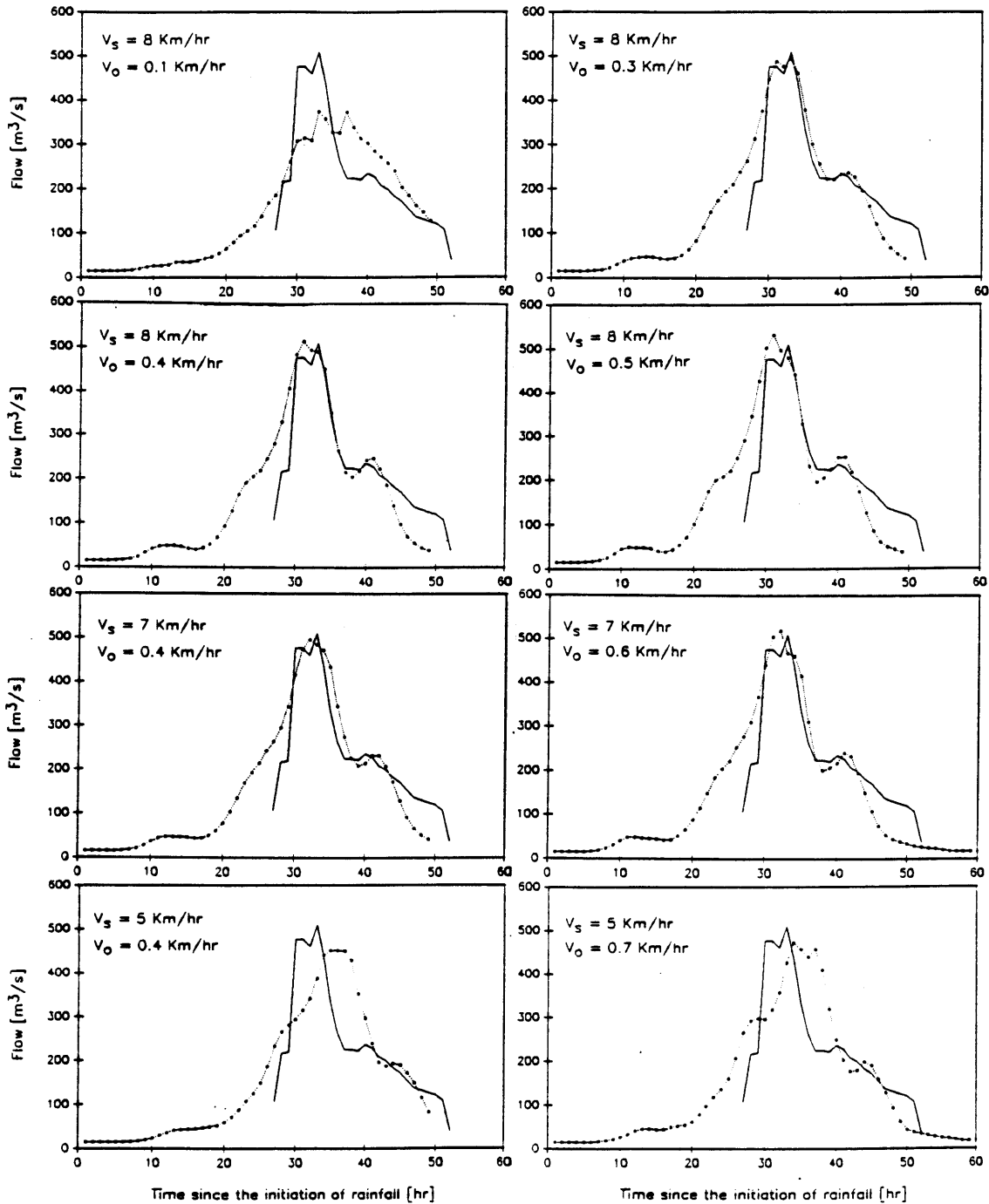
FIGURE 4.9 : Sensitivity of the predicted hydrograph to the velocity parameters V_S and V_0 for the storm of December, 1981. Note the small sensitivity to V_0 for $V_0 > 0.4$ Km/hr. The figure demonstrates the subjectivity involved in selecting one combination of V_S and V_0 as "the best" for a given storm (for example, not the similarity between the predicted hydrographs with $V_S = 8$ Km/hr and $V_0 = 0.4$ Km/hr and with $V_S = 7$ Km/hr and $V_0 = 0.6$ Km/hr).

135

Both stage and rainfall records exist for these twelve rainstorms. All events originated unusually high discharges. Unfortunately, no data is available for the pre-storm baseflow for any of the events. Therefore, we cannot determine R_i from observed baseflow as described in Section 3.D. In face of the unavailability of baseflow values, we will compute predicted hydrographs considering three hypothetical pre-storm baseflow values, representing a typical dry, average and moist condition for the month of the event in question. To represent the dry condition we will use the baseflow value that has an exceedence probability of 90% in that month; for the average condition we will use the value with 50% exceedence probability; and for the wet condition we will use the value with 10% exceedence probability. As examples, Figures 4.10, 4.11 and 4.12 represent derived steady-state groundwater positions corresponding to the wet, average, and dry minimum flow for the month of November.

These results are presented in Figures 4.13 through 4.48. By comparing the results of the three runs corresponding to each storm, we see that for some storms the dry initial condition provided the best hydrograph prediction, but for other storms the average or the wet initial condition was best. Using the minimum deviation between predicted and observed peak-flows as the criterion to define the best good prediction, we see from the Figures that 5 storms were predicted best with the dry initial groundwater condition (December 1968, January 1969, December 1975, November 1982, November 1987), 4 with the average condition (February, 1968, February 1977, January 1979, January 1985), and 3 with the wet condition (December 1976, December 1981, February 1983). Given that all 12 storms studied had high observed peak-flow discharges, it is somewhat surprising that in 5 of them the dry initialization provided the best

estimated, while the wet initial condition was best in only 3 cases. A possible explanation for this is the fact, already noted in Chapter 3, that the model to estimate the depth of the initial water-table tends to over-estimate the extent of the zones of saturation, given that the boundary condition for water-table depth adjacent to a channel is approximated by the elevation of the channel banks. If the extent of the zones of saturation are overestimated for a given water-table recharge rate, then a better prediction results from considering a lower recharge rate.

To investigate a relation between the initial condition which obtained the best estimate and the actual antecedent condition in the basin, we will use an antecedent precipitation index as an indicator of the degree of wetness of the basin. Figure 4.49 represents the quality of the prediction obtained with the average initialization (50% baseflow exceedence probability), in terms of percentage deviation of the predicted from the observed peak-flow, against an antecedent precipitation index (cumulative precipitation over the preceding 30 days). Only 9 of the 12 storms are represented in the Figure given the gaps encountered in the rainfall records in the 20-day period preceding each of the remaining 3 storms. We should expect to find a descending tendency in the plot, i. e., that storms with low antecedent precipitation to be overpredicted by the assumption of an average initial moisture content of the basin and, inversely, storms with high antecedent precipitation to be underpredicted by that assumption. This expected tendency is suggested in the plot. Nevertheless, the small number of points in the plot makes it difficult to derive a definite conclusion about any tendency in the results. A tendency would mean that the best value of R_i to use in groundwater initialization

during operational use of the model can be obtained from the observed baseflow at the storm start, as we suggest.

We consider that the model with the calibrated f and velocity parameters provided overall reasonable estimates of peak flow rate, timeliness of peak flow, and hydrograph shape in general. It must be noted, however, that these are not true verification runs, as the storms utilized here are the same used for calibration of the routing parameters. However, the velocity parameters providing the best fit for the different storms showed clear consistency, which in itself provides credibility.
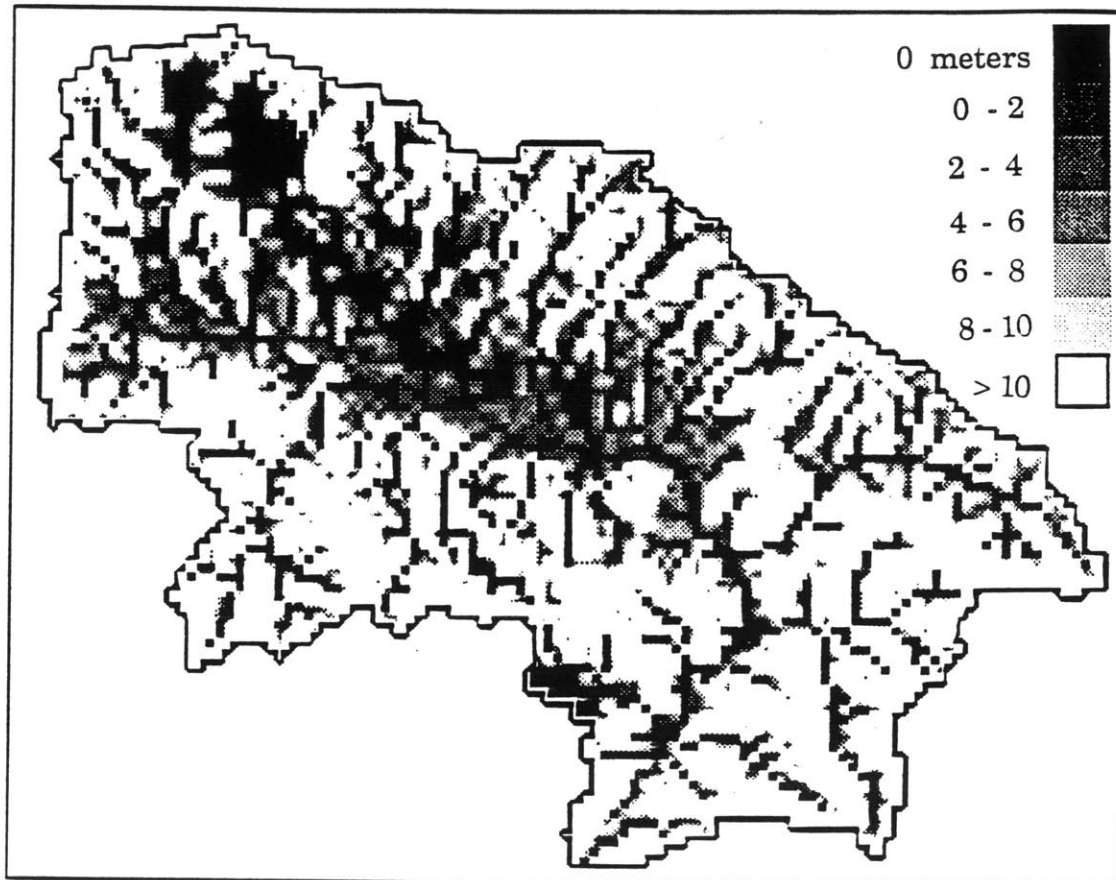
FIGURE 4.10: Depth below the surface (in meters) of the water-table in a *dry* month of November. The water-table is in steady-state with the basin discharge rate, Q_b = 1.0 m³/s (the corresponding recharge rate is $R_i = Q_b/A$ = 0.0043 mm/hr), that has an exceedence probability of 90% in November.
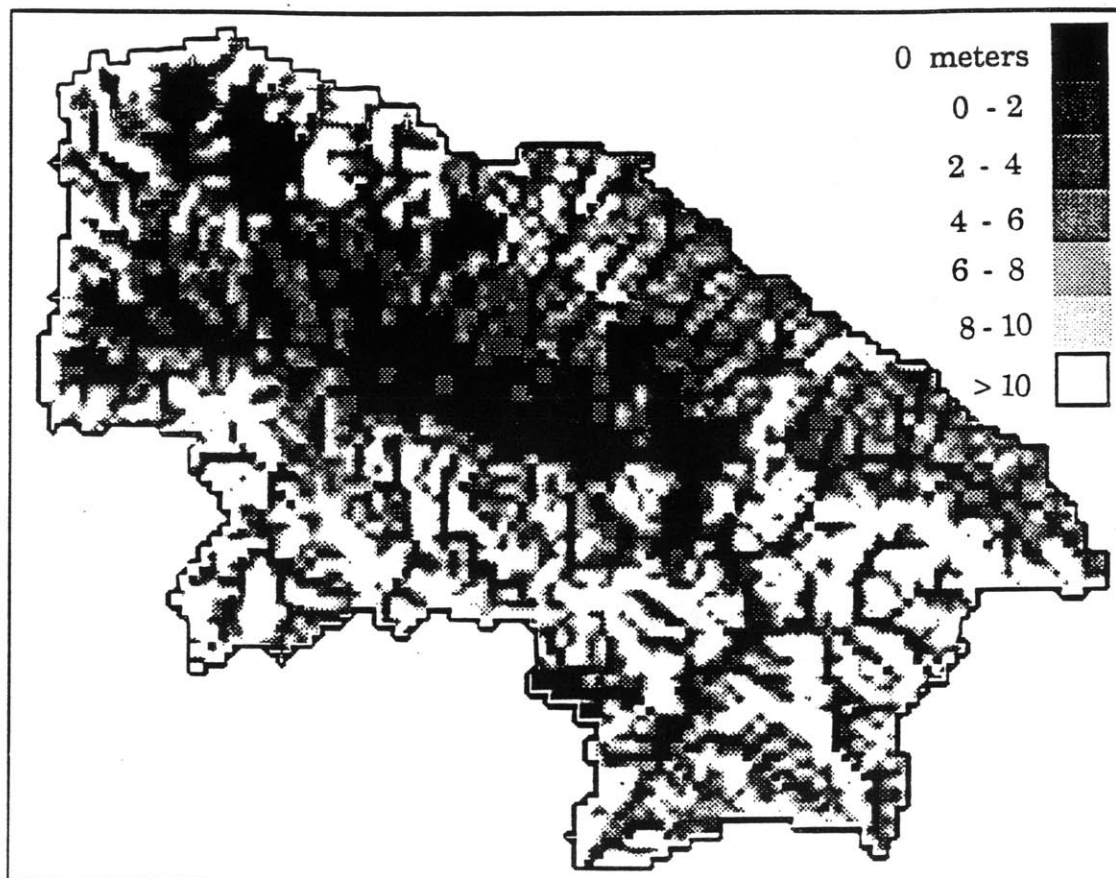
FIGURE 4.11: Depth below the surface (in meters) of the water-table in a *average* month of November. The water-table is in steady-state with the basin discharge rate, Q_b = 4.0 m^3/s (the corresponding recharge rate is $R_i = Q_b/A$ = 0.0171 mm/hr), that has an exceedence probability of 50% in November.

140
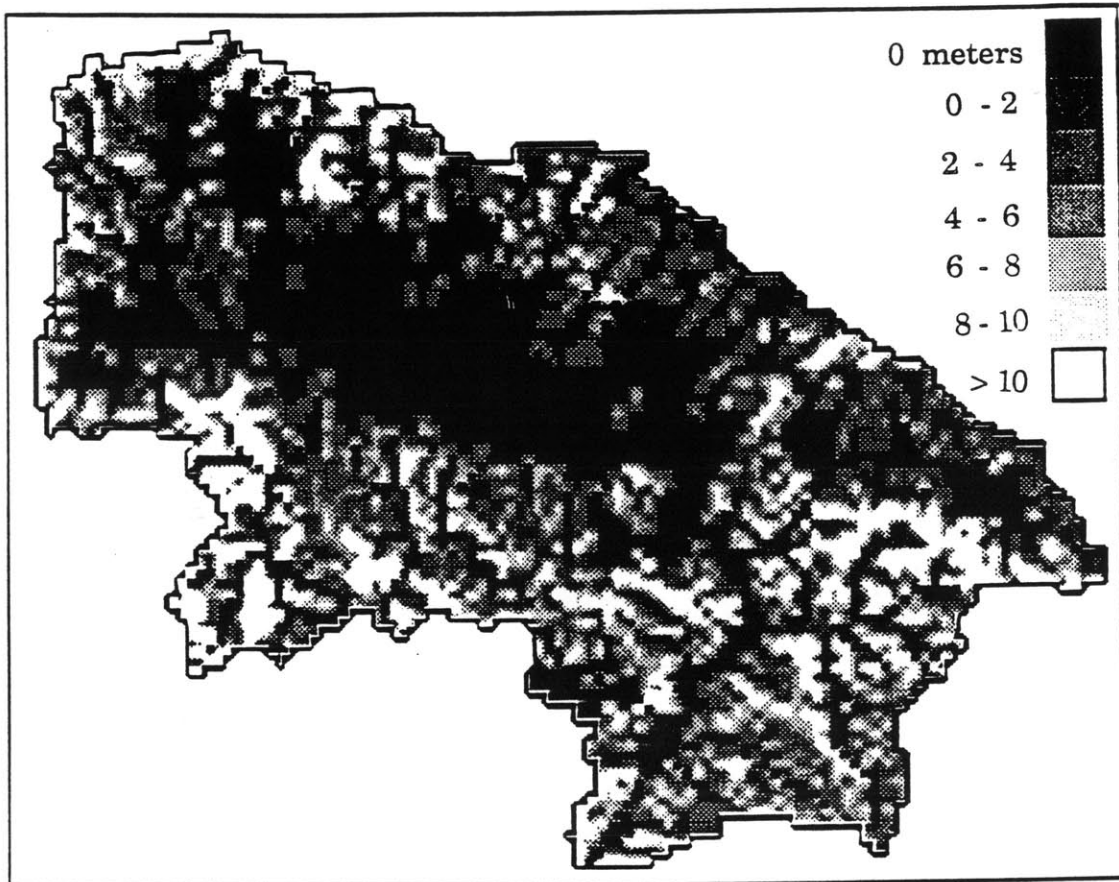
FIGURE 4.12: Depth below the surface (in meters) of the water-table in a *wet* month of November. The water-table is in steady-state with the basin discharge rate, Q_b = 10.0 m³/s (the corresponding recharge rate is R_i = Q_b/A = 0.0428 mm/hr), that has an exceedence probability of 10% in November.

Storm of February, 1968
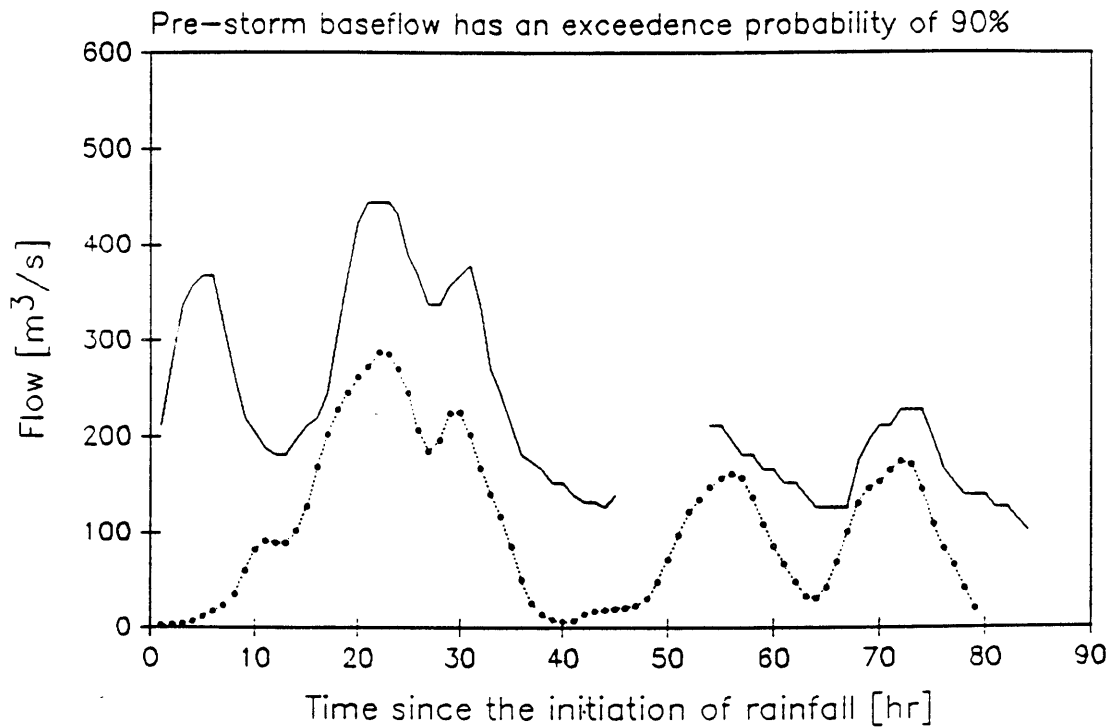
Pre—storm baseflow has an exceedence probability of 90%

FIGURE 4.24: Observed (solid line) and predicted (dashed line) hydrographs for the storm of February, 1968. Groundwater was initialized in steady-state with the **dry recharge rate** (i. e. that has an exceedence probability of 90%) in the month of February, R_i = 0.0129 mm/hr.

Storm of February, 1968

Pre-storm baseflow has an exceedence probability of 50%

FIGURE 4.14: Observed (solid line) and predicted (dashed line) hydrographs for the storm of February, 1968. Groundwater was initialized in steady-state with the **average recharge rate** (i. e. that has an exceedence probability of 50%) in the month of February, R_i = 0.0386 mm/hr.

Storm of February, 1968

FIGURE 4.15: Observed (solid line) and predicted (dashed line) hydrographs for the storm of February, 1968. Groundwater was initialized in steady-state with the **wet recharge rate** (i. e. that has an exceedence probability of 10%) in the month of February, R_i = 0.0728 mm/hr.

144

Storm of December, 1968

Pre—storm baseflow has an exceedence probability of 90%

FIGURE 4.16: Observed (solid line) and predicted (dashed line) hydrographs for the storm of December, 1968. Groundwater was initialized in steady-state with the **dry recharge rate** (i. e. that has an exceedence probability of 90%) in the month of December, $R_i = 0.0087$ mm/hr.

Storm of December, 1968

FIGURE 4.17: Observed (solid line) and predicted (dashed line) hydrographs for the storm of December, 1968. Groundwater was initialized in steady-state with the **average recharge rate** (i. e. that has an exceedence probability of 50%) in the month of December, R_i = 0.0300 mm/hr.

146

Storm of December, 1968

Pre—storm baseflow has an exceedence probability of 10%

FIGURE 4.18: Observed (solid line) and predicted (dashed line) hydrographs for the storm of December, 1968. Groundwater was initialized in steady-state with the **wet recharge rate** (i. e. that has an exceedence probability of 10%) in the month of December, $R_i = 0.0664$ mm/hr.

Storm of January, 1969

FIGURE 4.19: Observed (solid line) and predicted (dashed line) hydrographs for the storm of January, 1969. Groundwater was initialized in steady-state with the **dry recharge rate** (i. e. that has an exceedence probability of 90%) in the month of January, $R_i = 0.0129$ mm/hr.

Storm of January, 1969

Pre—storm baseflow has an exceedence probability of 50%

FIGURE 4.20: Observed (solid line) and predicted (dashed line) hydrographs for the storm of January, 1969. Groundwater was initialized in steady-state with the **average recharge rate** (i. e. that has an exceedence probability of 50%) in the month of January, R_i = 0.0321 mm/hr.

Storm of January, 1969

Pre—storm baseflow has an exceedence probability of 10%

FIGURE 4.21: Observed (solid line) and predicted (dashed line) hydrographs for the storm of January, 1969. Groundwater was initialized in steady-state with the **wet recharge rate** (i. e. that has an exceedence probability of 10%) in the month of January, R_i = 0.0643 mm/hr.

Storm of December, 1975

FIGURE 4.22: Observed (solid line) and predicted (dashed line) hydrographs for the storm of December, 1975. Groundwater was initialized in steady-state with the **dry recharge rate** (i. e. that has an exceedence probability of 90%) in the month of December, $R_i = 0.0087$ mm/hr.

Storm of December, 1975
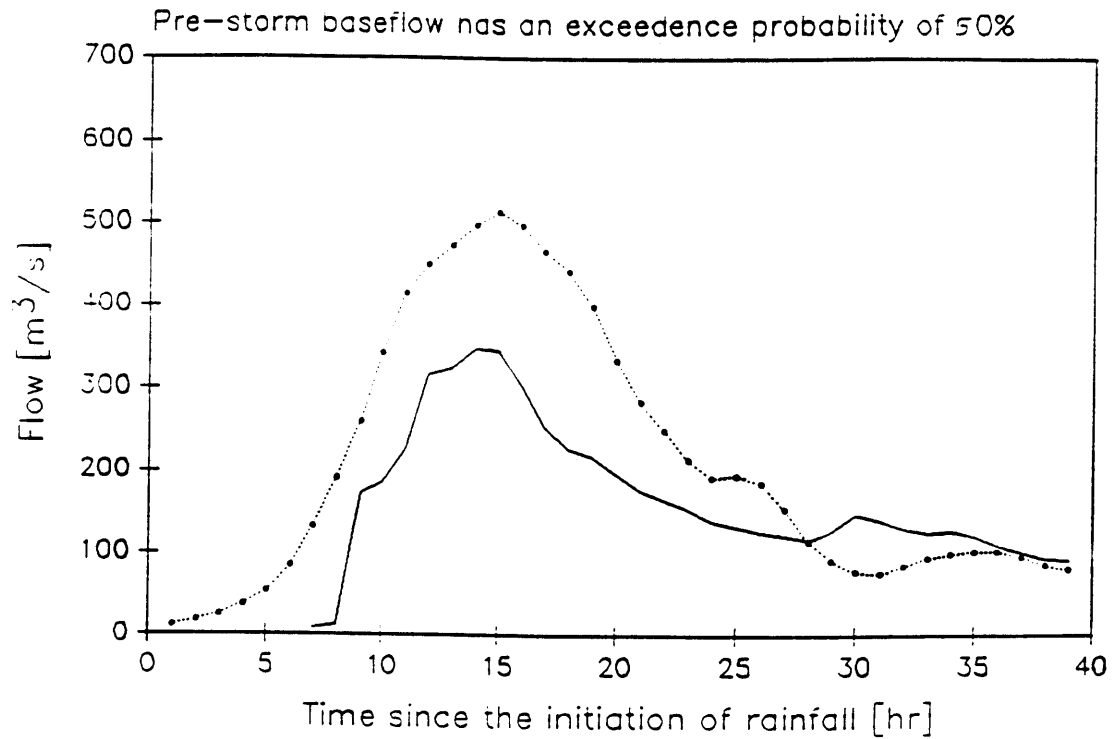
FIGURE 4.23: Observed (solid line) and predicted (dashed line) hydrographs for the storm of December, 1975. Groundwater was initialized in steady-state with the **average recharge rate** (i. e. that has an exceedence probability of 50%) in the month of December, $R_i = 0.0300$ mm/hr.

152

Storm of December, 1975

FIGURE 4.24: Observed (solid line) and predicted (dashed line) hydrographs for the storm of December, 1975. Groundwater was initialized in steady-state with the **wet recharge rate** (i. e. that has an exceedence probability of 10%) in the month of December, $R_i = 0.0664$ mm/hr.

Storm of December, 1976

Pre—storm baseflow has an exceedence probability of 90%
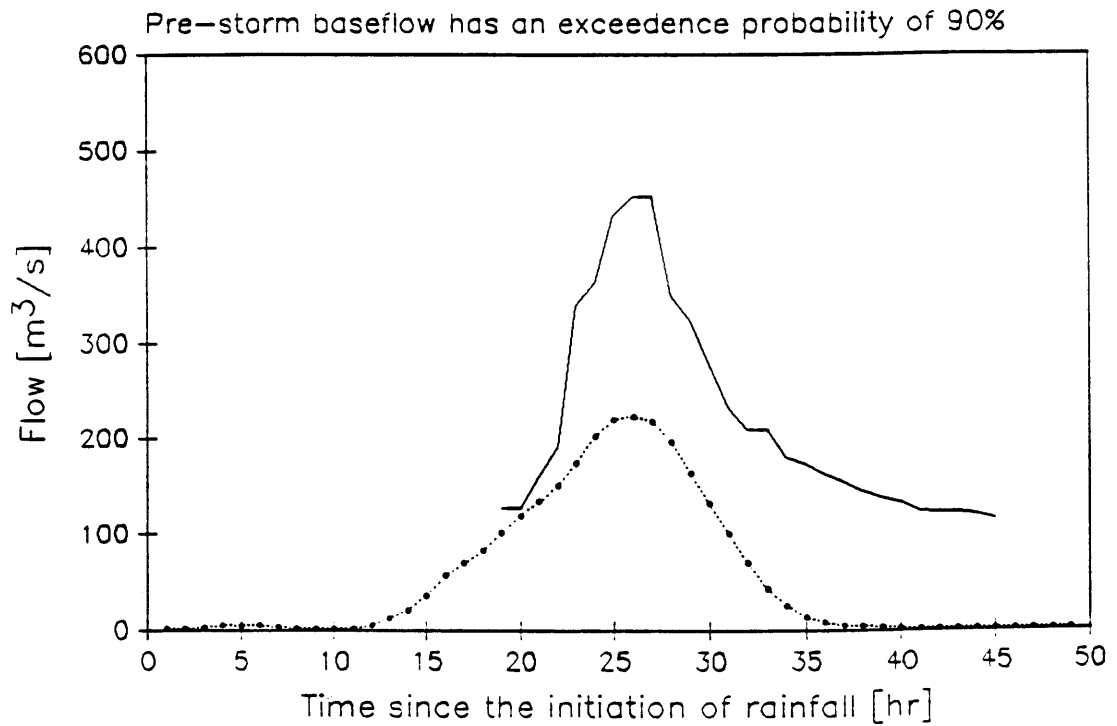
FIGURE 4.25: Observed (solid line) and predicted (dashed line) hydrographs for the storm of December, 1976. Groundwater was initialized in steady-state with the **dry recharge rate** (i. e. that has an exceedence probability of 90%) in the month of December, $R_i = 0.0087$ mm/hr.

Storm of December, 1976

Pre—storm baseflow has an exceedence probability of 50%
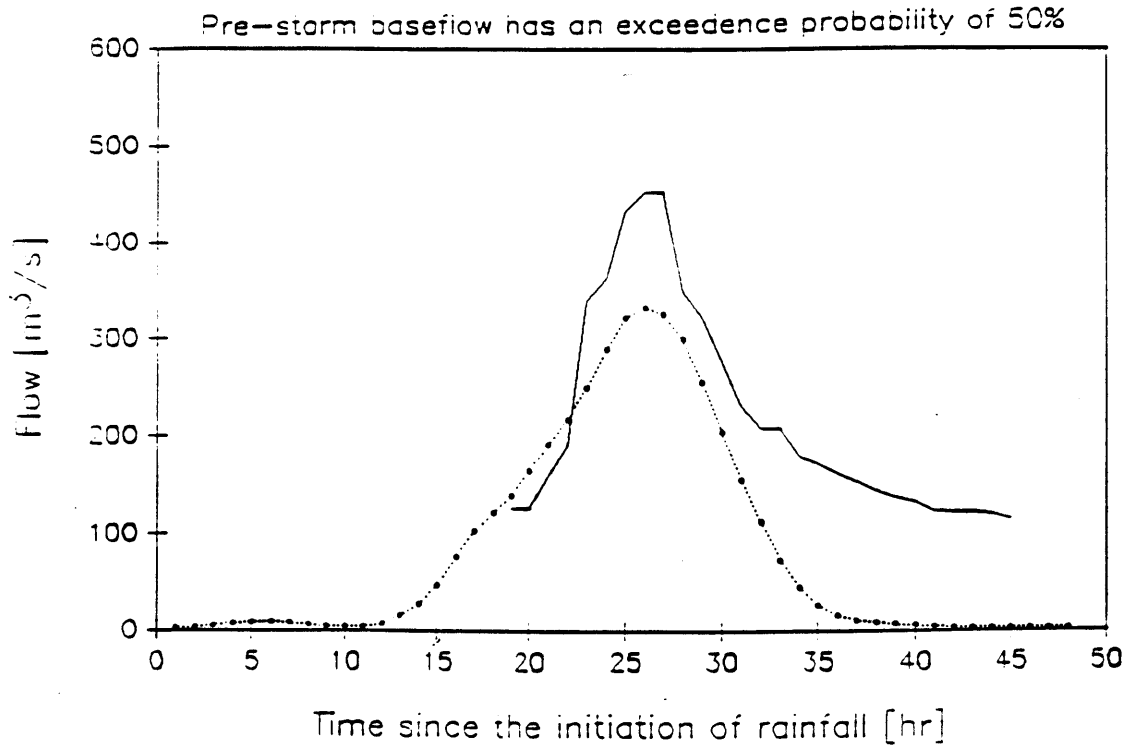
FIGURE 4.26: Observed (solid line) and predicted (dashed line) hydrographs for the storm of December, 1976. Groundwater was initialized in steady-state with the **average recharge rate** (i. e. that has an exceedence probability of 50%) in the month of December, $R_i = 0.0300$ mm/hr.

Storm of December, 1976
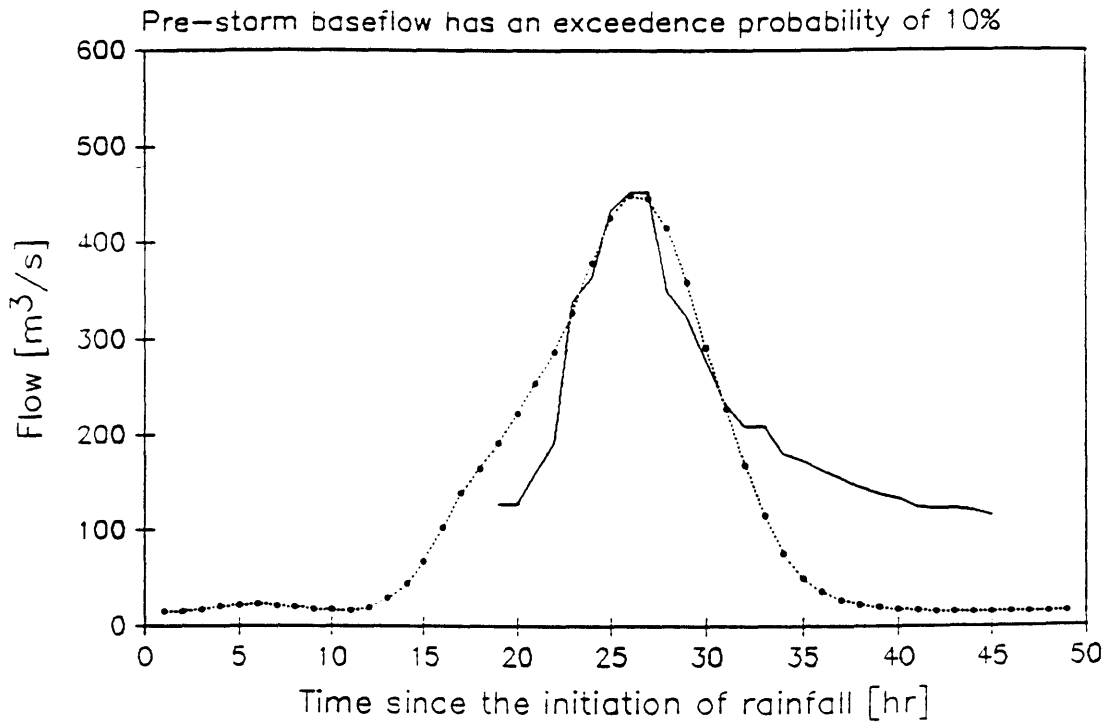
FIGURE 4.27: Observed (solid line) and predicted (dashed line) hydrographs for the storm of December, 1976. Groundwater was initialized in steady-state with the **wet recharge rate** (i. e. that has an exceedence probability of 10%) in the month of December, $R_i = 0.0664$ mm/hr.

Storm of February, 1977

Pre-storm baseflow has an exceedence probability of 90%
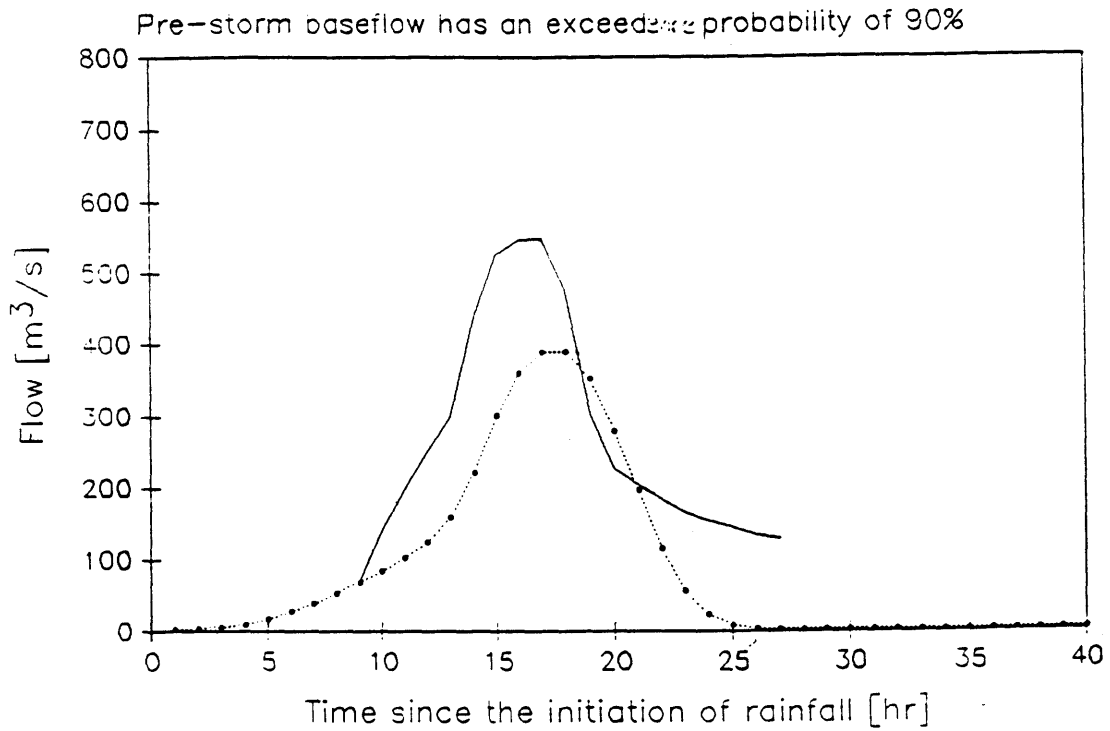
FIGURE 4.28: Observed (solid line) and predicted (dashed line) hydrographs for the storm of February, 1977. Groundwater was initialized in steady-state with the **dry recharge rate** (i. e. that has an exceedence probability of 90%) in the month of February, $R_i = 0.0129$ mm/hr.

Storm of February, 1977

Pre-storm baseflow has an exceeding probability of 50%
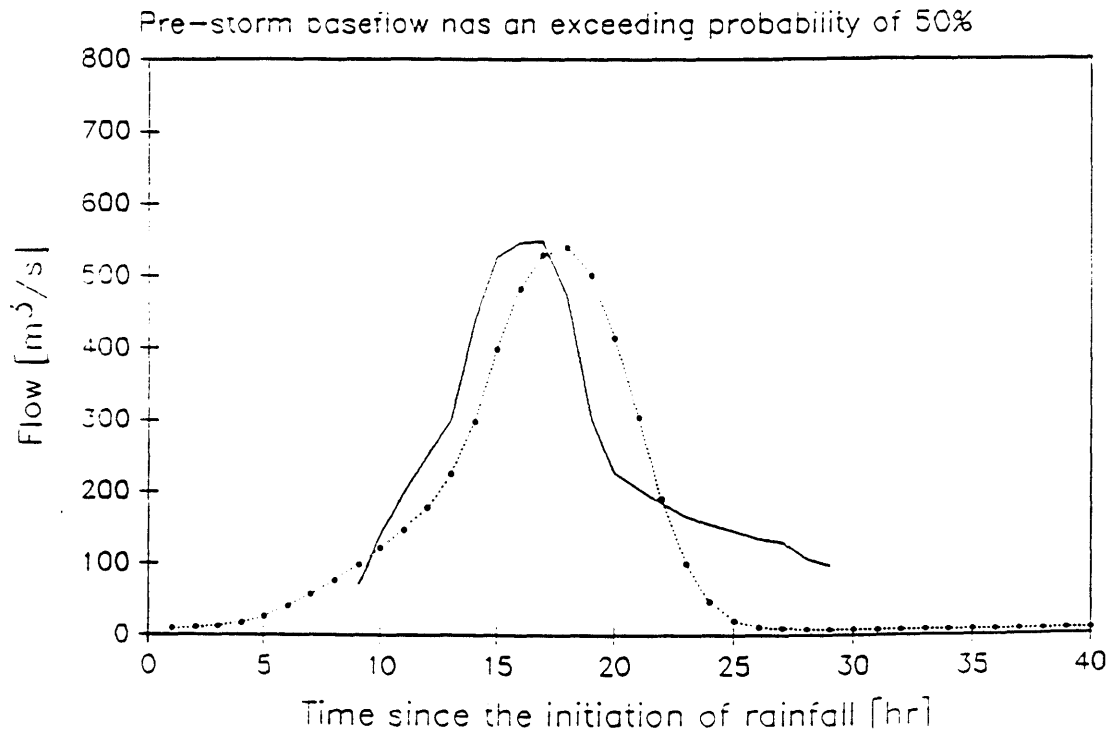
FIGURE 4.29: Observed (solid line) and predicted (dashed line) hydrographs for the storm of February, 1977. Groundwater was initialized in steady-state with the **average recharge rate** (i. e. that has an exceedence probability of 50%) in the month of February, R_i = 0.0386 mm/hr.

Storm of February, 1977

Pre-storm baseflow has an exceeding probability of 10%
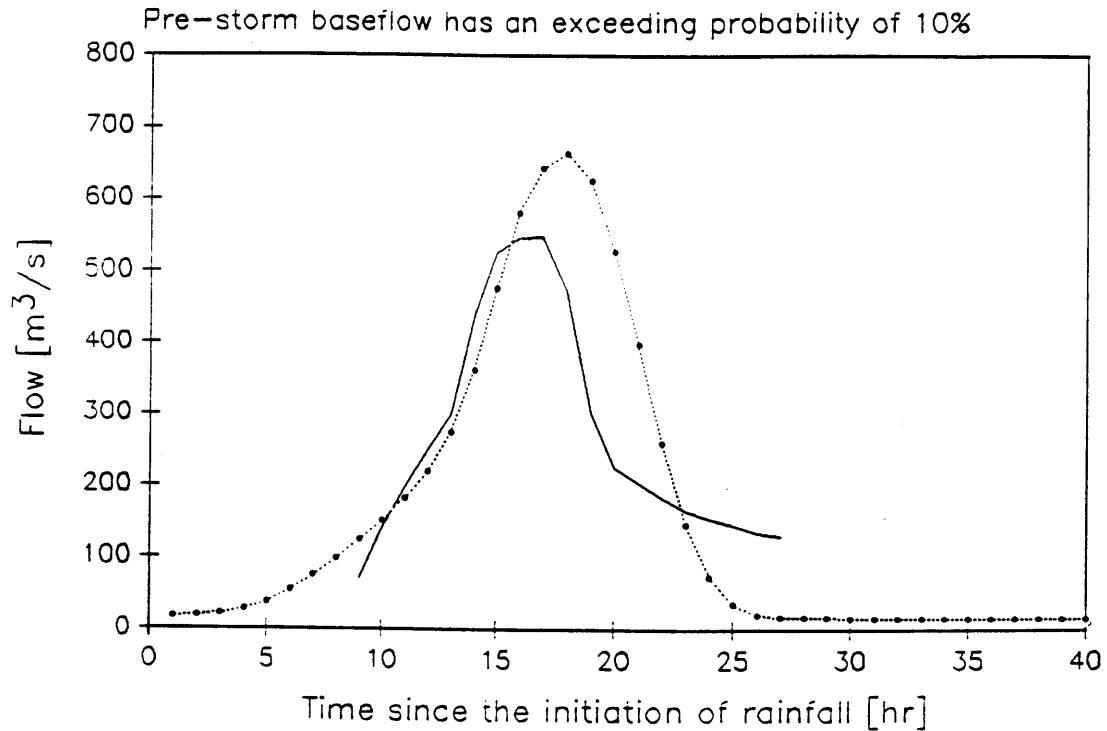
FIGURE 4.30: Observed (solid line) and predicted (dashed line) hydrographs for the storm of February, 1977. Groundwater was initialized in steady-state with the **wet recharge rate** (i. e. that has an exceedence probability of 10%) in the month of February, $R_i = 0.00428$ mm/hr.

Storm of January, 1979

Pre—storm baseflow has an exceedence probability of 90%
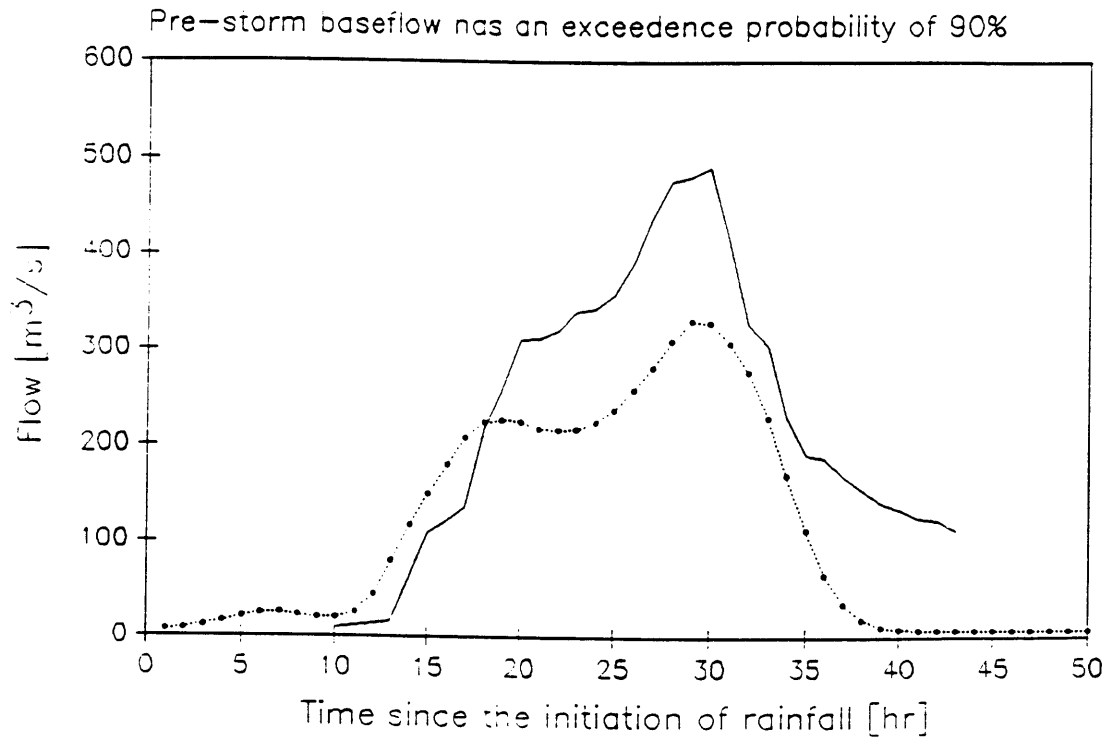
FIGURE 4.31: Observed (solid line) and predicted (dashed line) hydrographs for the storm of January, 1979. Groundwater was initialized in steady-state with the **dry recharge rate** (i. e. that has an exceedence probability of 90%) in the month of January, R_i = 0.0129 mm/hr.

Storm of January, 1979

Pre—storm baseflow has an exceedence probability of 50%
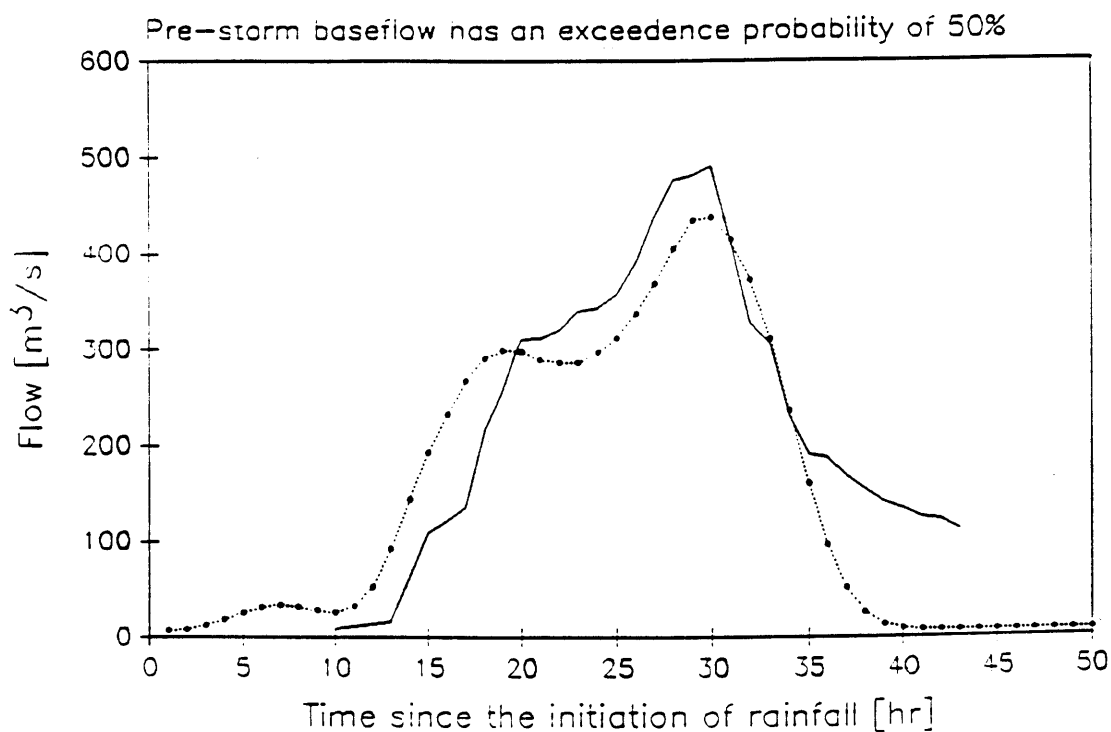
FIGURE 4.32: Observed (solid line) and predicted (dashed line) hydrographs for the storm of January, 1979. Groundwater was initialized in steady-state with the **average recharge rate** (i. e. that has an exceedence probability of 50%) in the month of January $R_i = 0.0321$ mm/hr.

Storm of January, 1979

Pre—storm baseflow has an exceedence probability of 10%
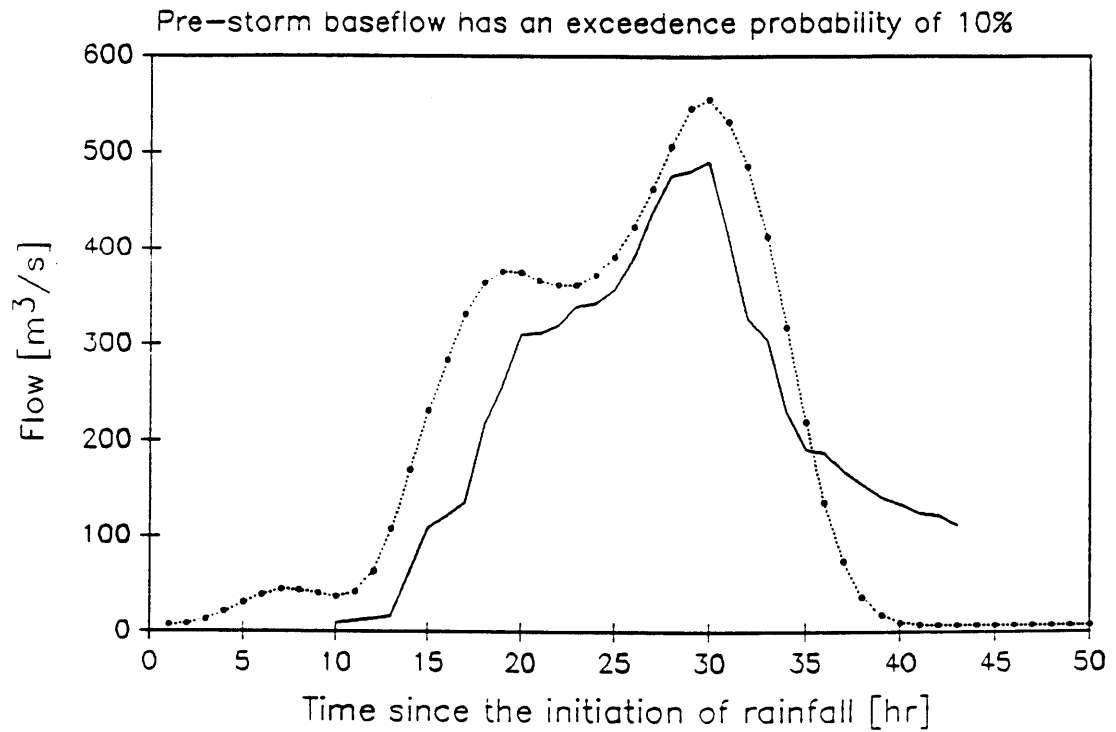
FIGURE 4.33: Observed (solid line) and predicted (dashed line) hydrographs for the storm of January, 1979. Groundwater was initialized in steady-state with the **wet recharge rate** (i. e. that has an exceedence probability of 10%) in the month of January, $R_i = 0.0643$ mm/hr.

Storm of December, 1981
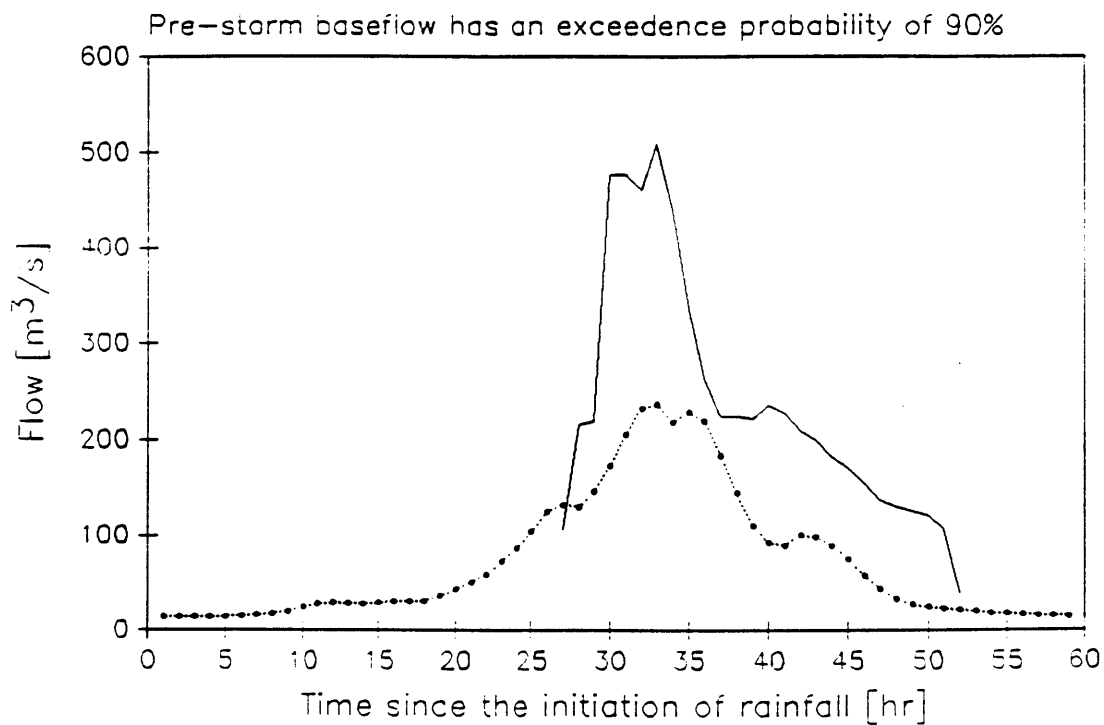
FIGURE 4.34: Observed (solid line) and predicted (dashed line) hydrographs for the storm of December, 1981. Groundwater was initialized in steady-state with the **dry recharge rate** (i. e. that has an exceedence probability of 90%) in the month of December, $R_i = 0.0087$ mm/hr.

Storm of December, 1981
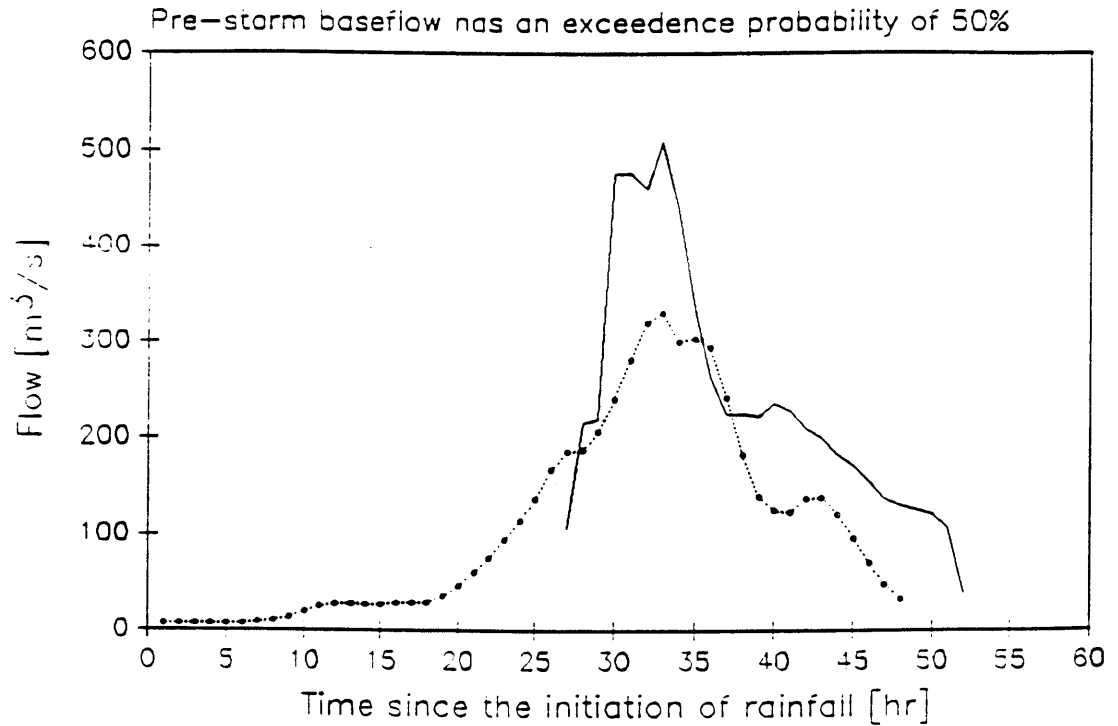
FIGURE 4.35: Observed (solid line) and predicted (dashed line) hydrographs for the storm of December, 1981. Groundwater was initialized in steady-state with the **average recharge rate** (i. e. that has an exceedence probability of 50%) in the month of December, $R_i = 0.0300$ mm/hr.

Storm of December, 1981
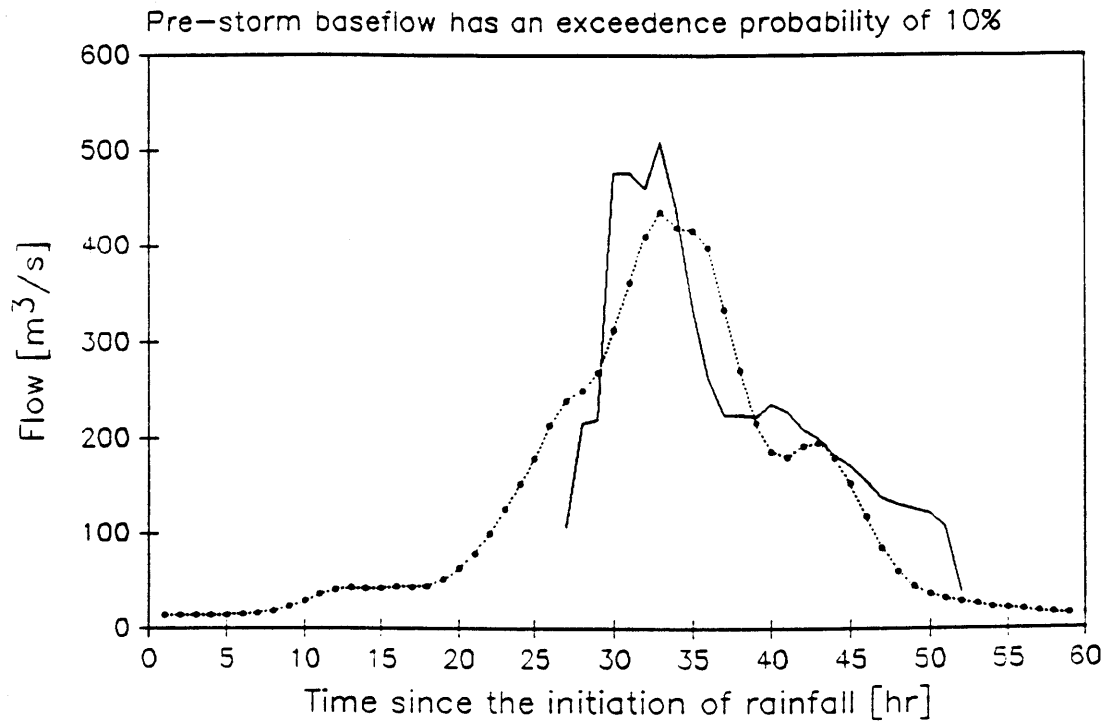
FIGURE 4.36: Observed (solid line) and predicted (dashed line) hydrographs for the storm of December, 1981. Groundwater was initialized in steady-state with the **wet recharge rate** (i. e. that has an exceedence probability of 10%) in the month of December, R_i = 0.0664 mm/hr.
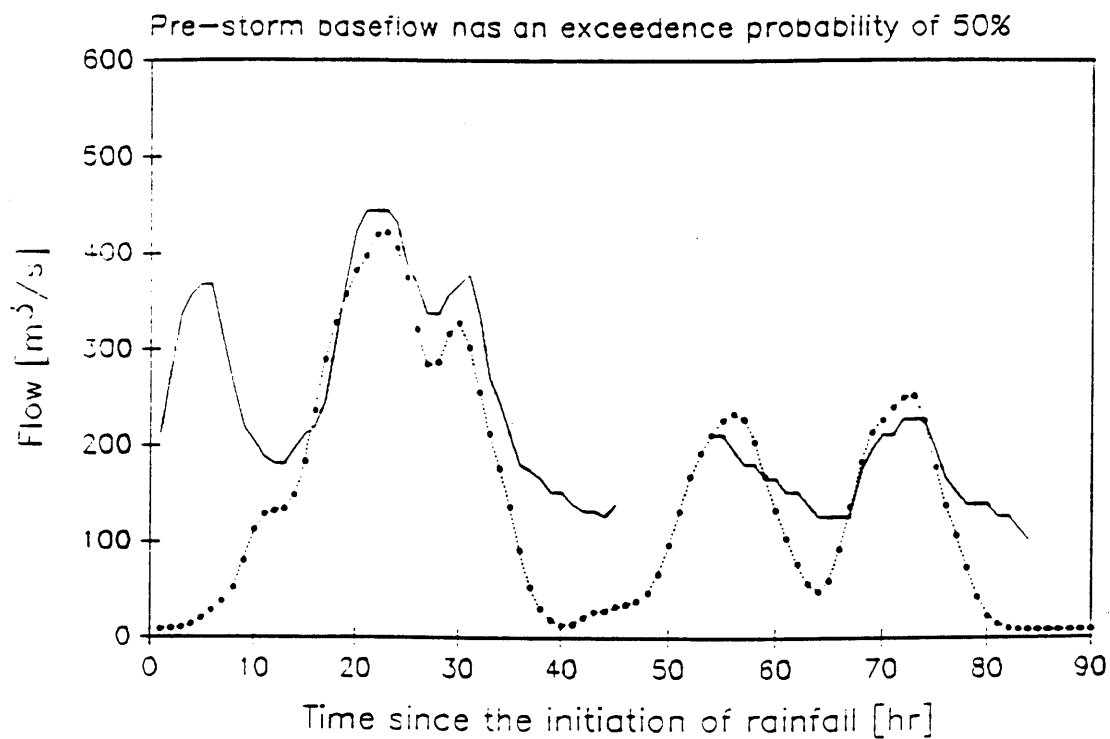
Storm of November, 1982
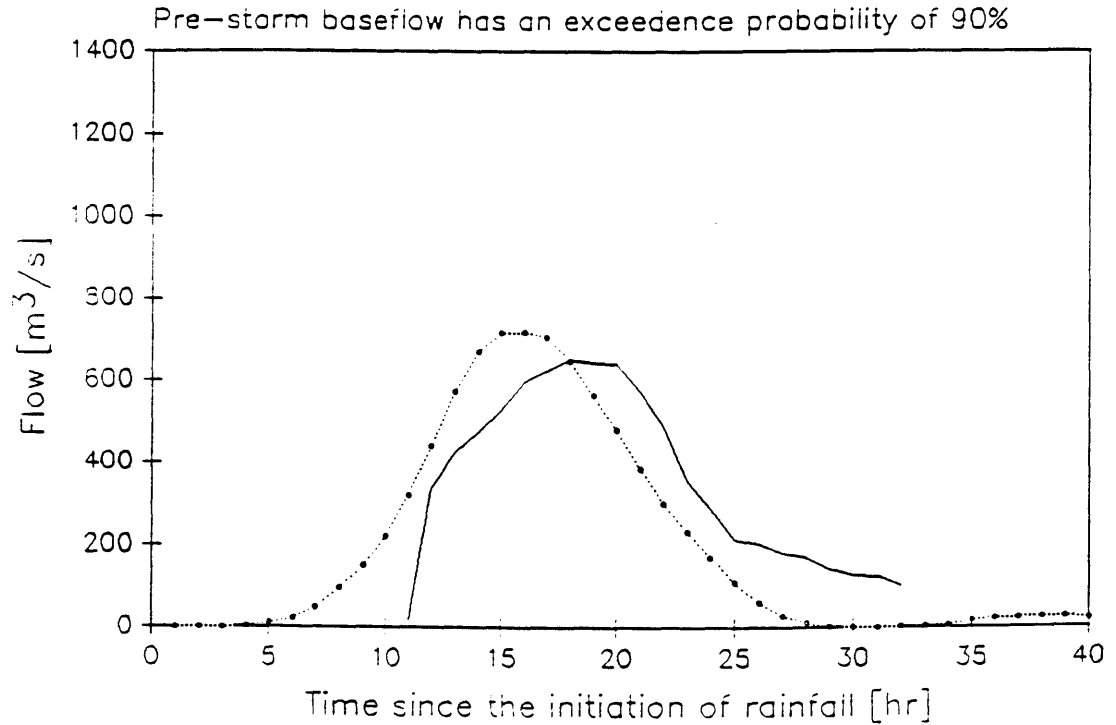
FIGURE 4.37: Observed (solid line) and predicted (dashed line) hydrographs for the storm of November, 1982. Groundwater was initialized in steady-state with the **dry recharge rate** (i. e. that has an exceedence probability of 90%) in the month of November, $R_i = 0.00428$ mm/hr.

Storm of November, 1982
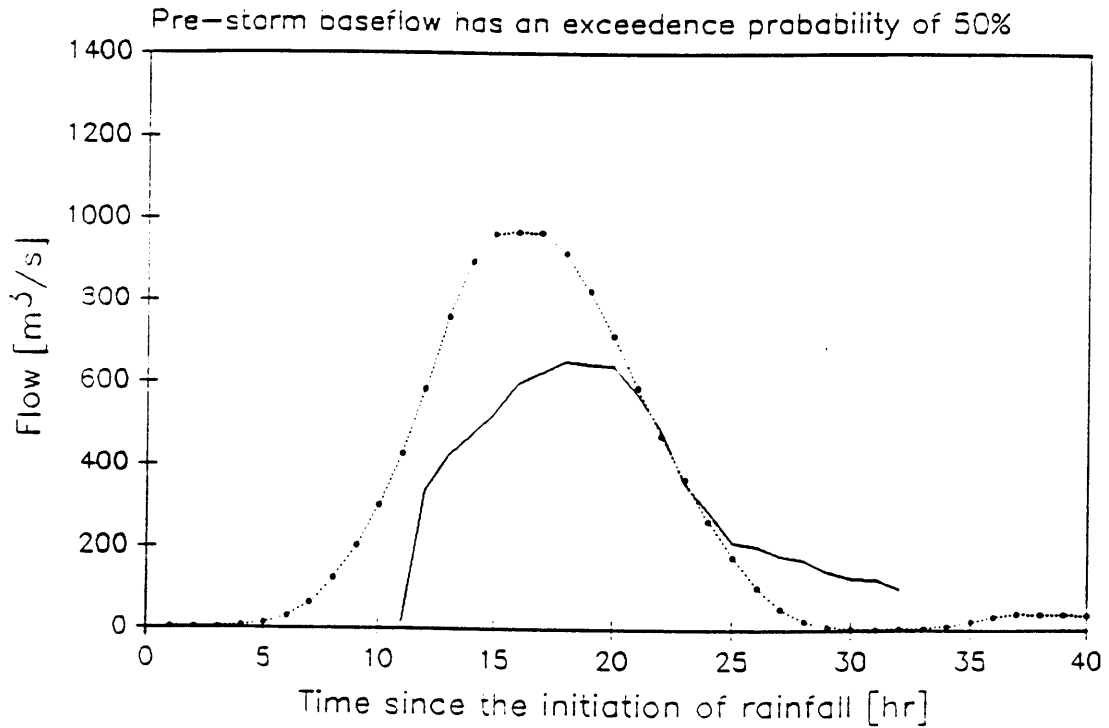
FIGURE 4.38: Observed (solid line) and predicted (dashed line) hydrographs for the storm of November, 1982. Groundwater was initialized in steady-state with the **average recharge rate** (i. e. that has an exceedence probability of 50%) in the month of November, $R_i = 0.0171$ mm/hr.

Storm of November, 1982
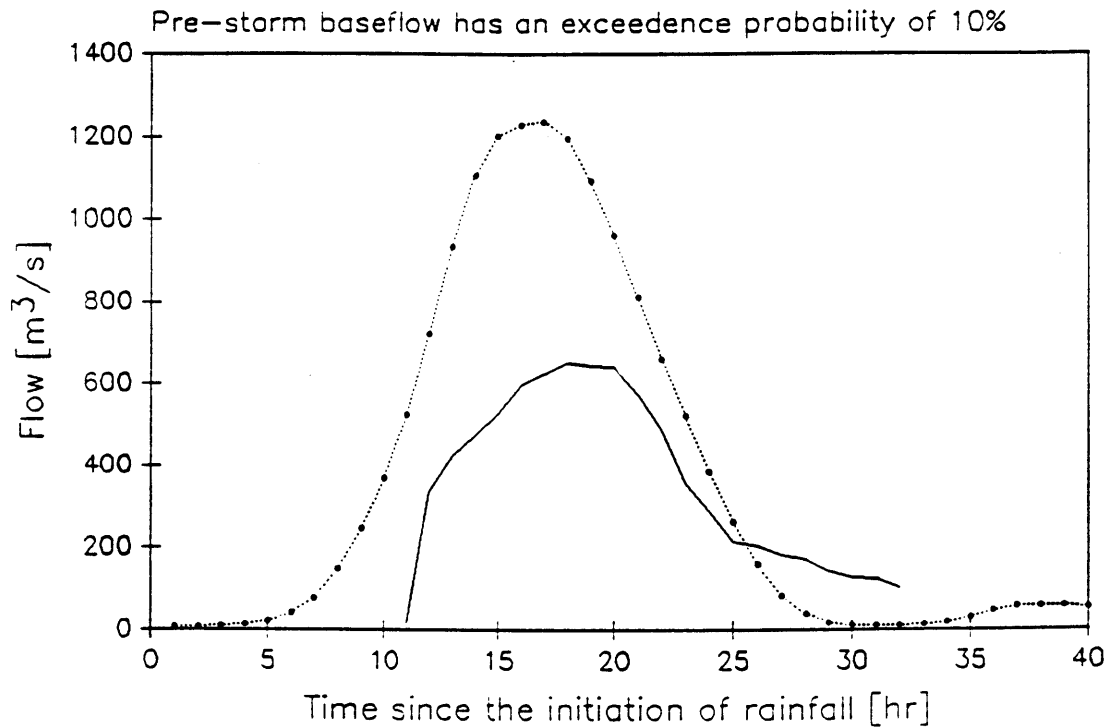
FIGURE 4.39: Observed (solid line) and predicted (dashed line) hydrographs for the storm of November, 1982. Groundwater was initialized in steady-state with the **wet recharge rate** (i. e. that has an exceedence probability of 10%) in the month of November, R_i = 0.0428 mm/hr.
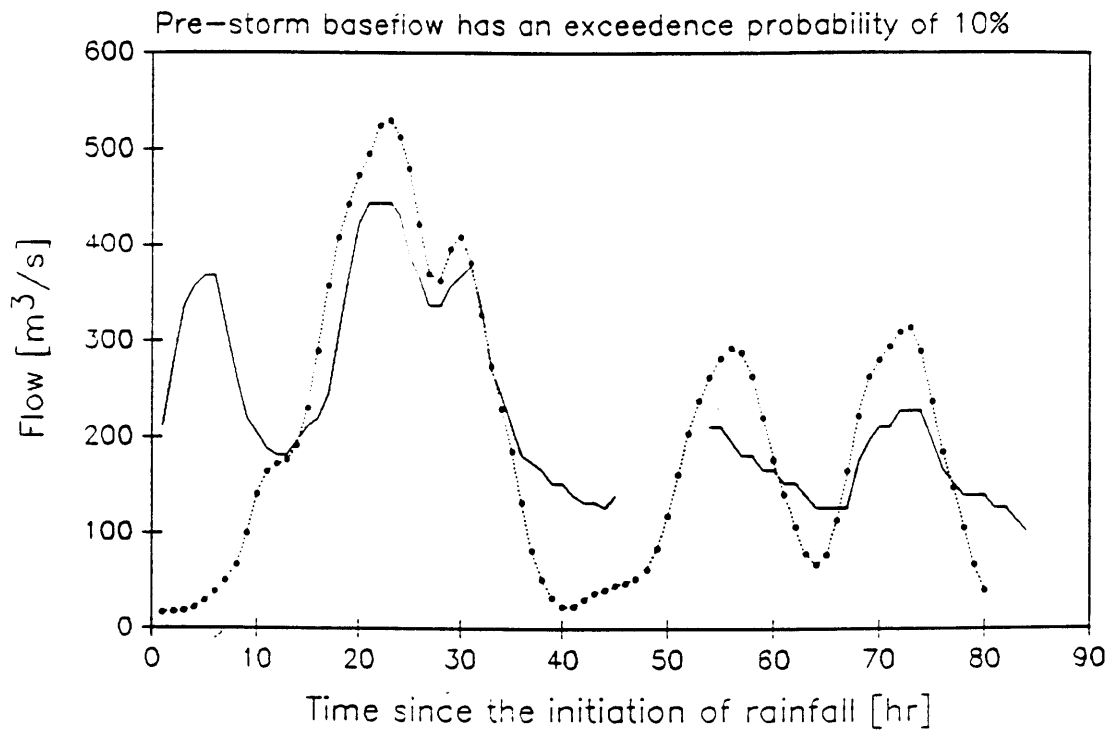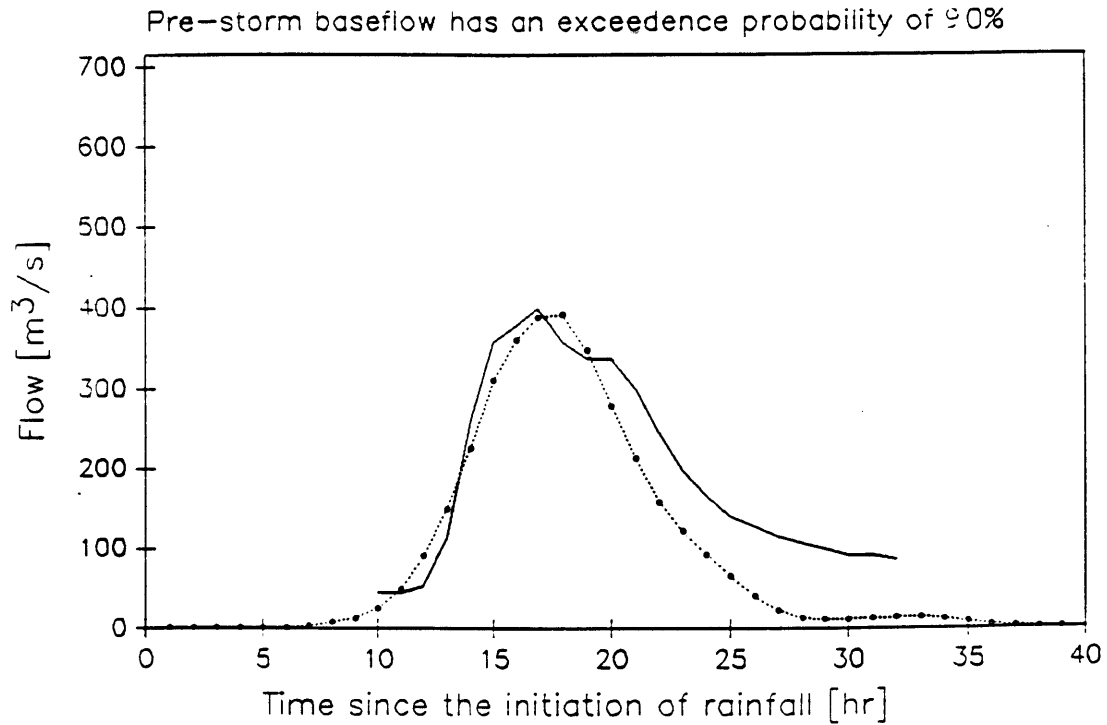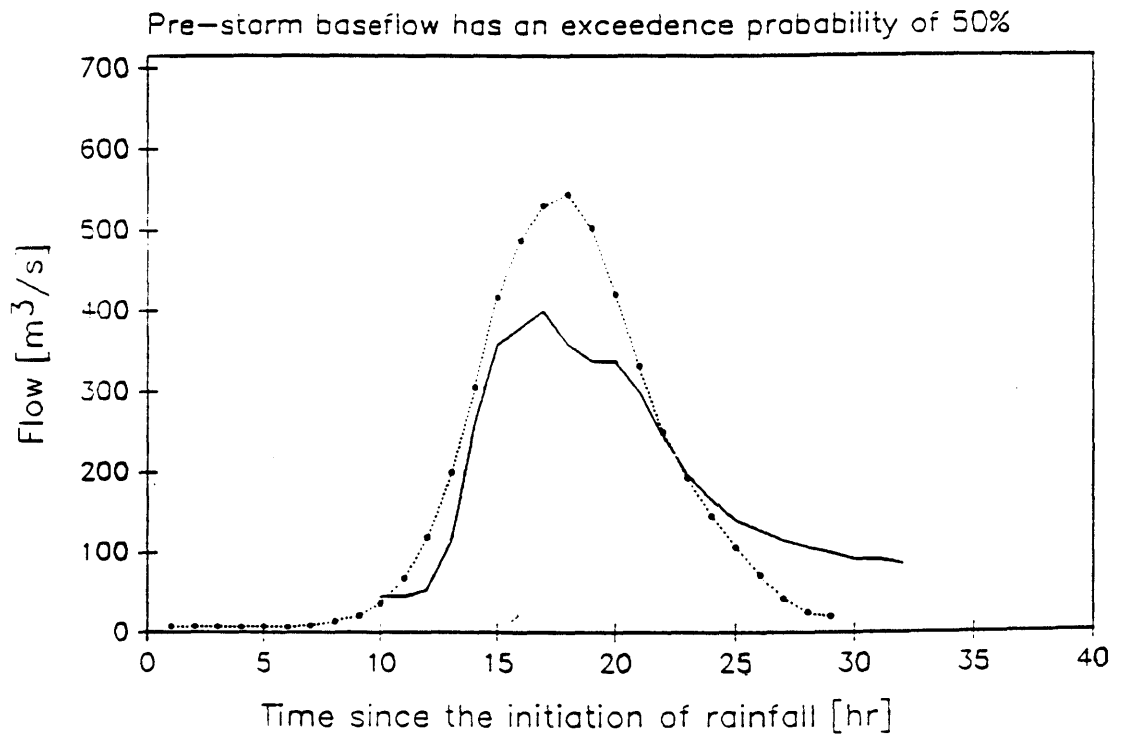
Storm of February, 1983
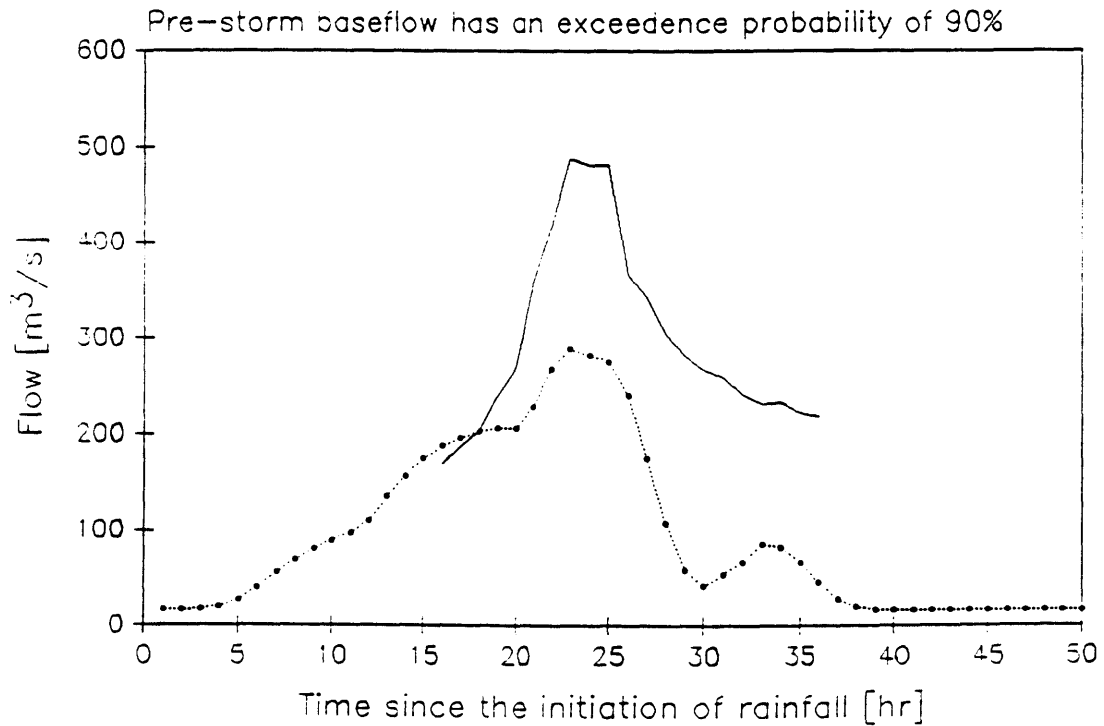
FIGURE 4.40: Observed (solid line) and predicted (dashed line) hydrographs for the storm of February, 1983. Groundwater was initialized in steady-state with the **dry recharge rate** (i. e. that has an exceedence probability of 90%) in the month of February, $R_i = 0.0129$ mm/hr.
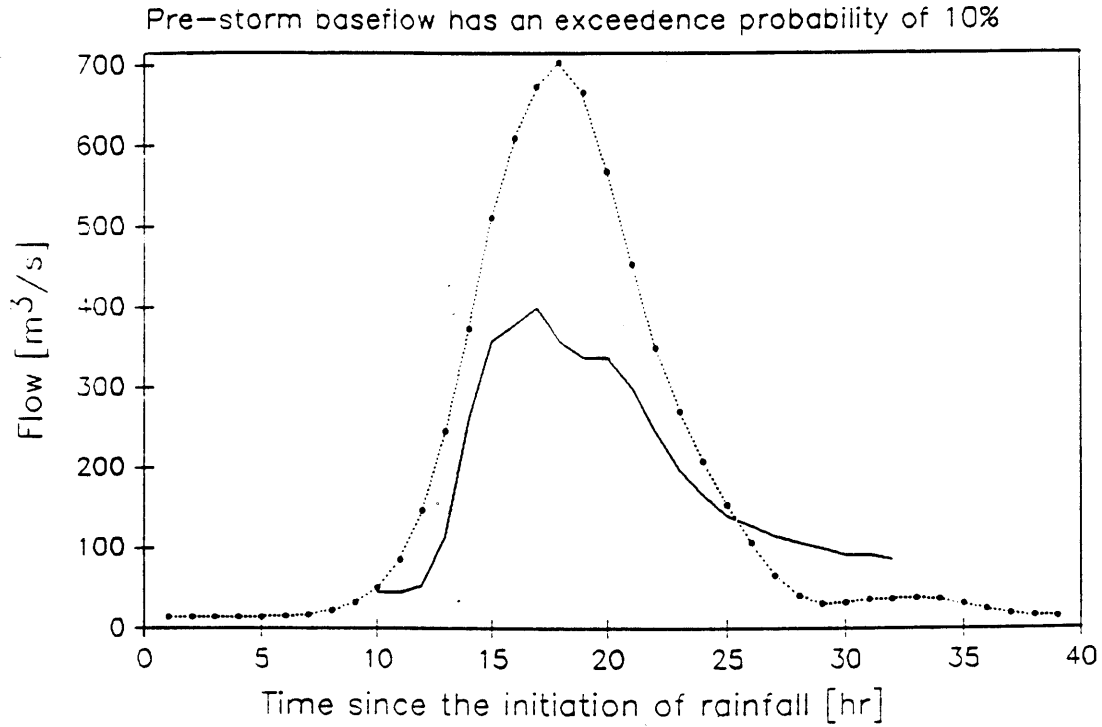
Storm of February, 1983
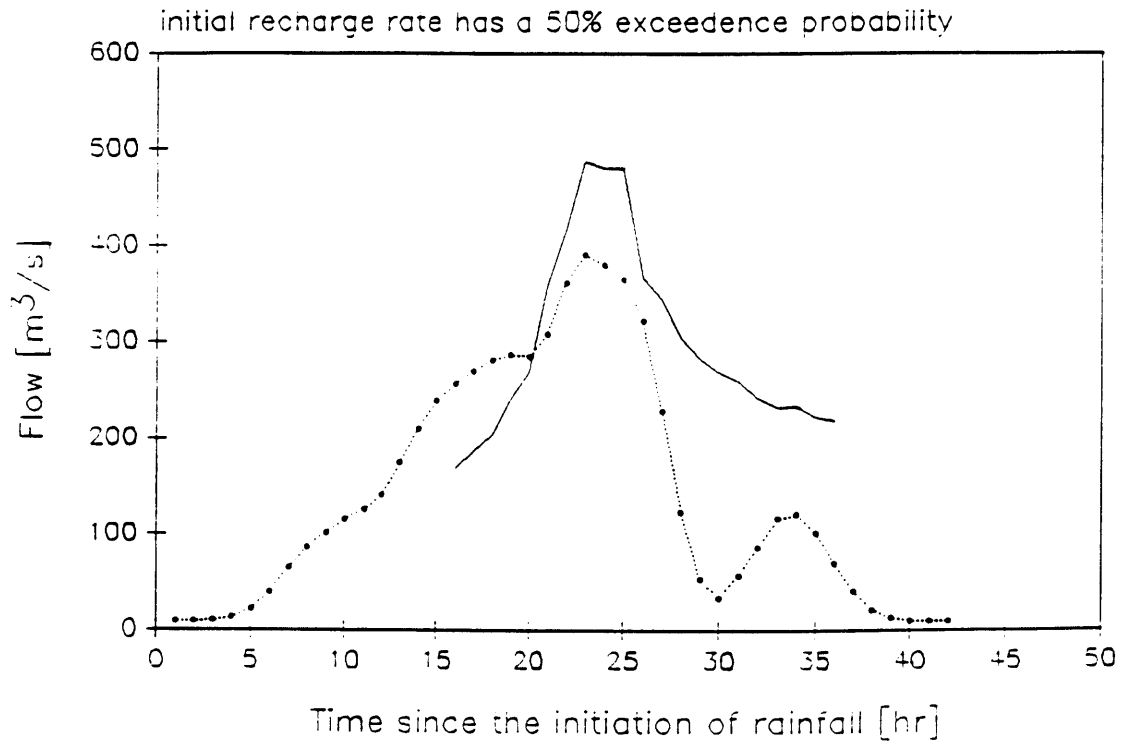
FIGURE 4.41: Observed (solid line) and predicted (dashed line) hydrographs for the storm of February, 1983. Groundwater was initialized in steady-state with the **average recharge rate** (i. e. that has an exceedence probability of 50%) in the month of February, $R_i = 0.0386$ mm/hr.

Storm of February, 1983
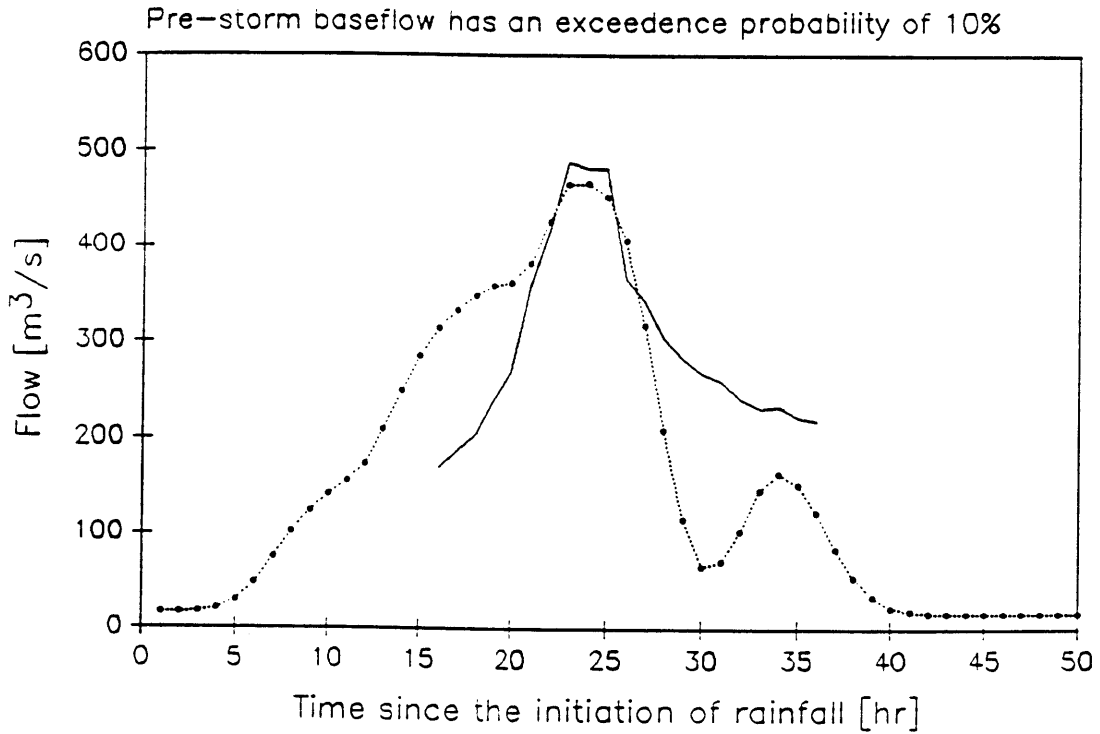
FIGURE 4.42: Observed (solid line) and predicted (dashed line) hydrographs for the storm of February, 1983. Groundwater was initialized in steady-state with the **wet recharge rate** (i. e. that has an exceedence probability of 10%) in the month of February, R_i = 0.00428 mm/hr.

Storm of January, 1985
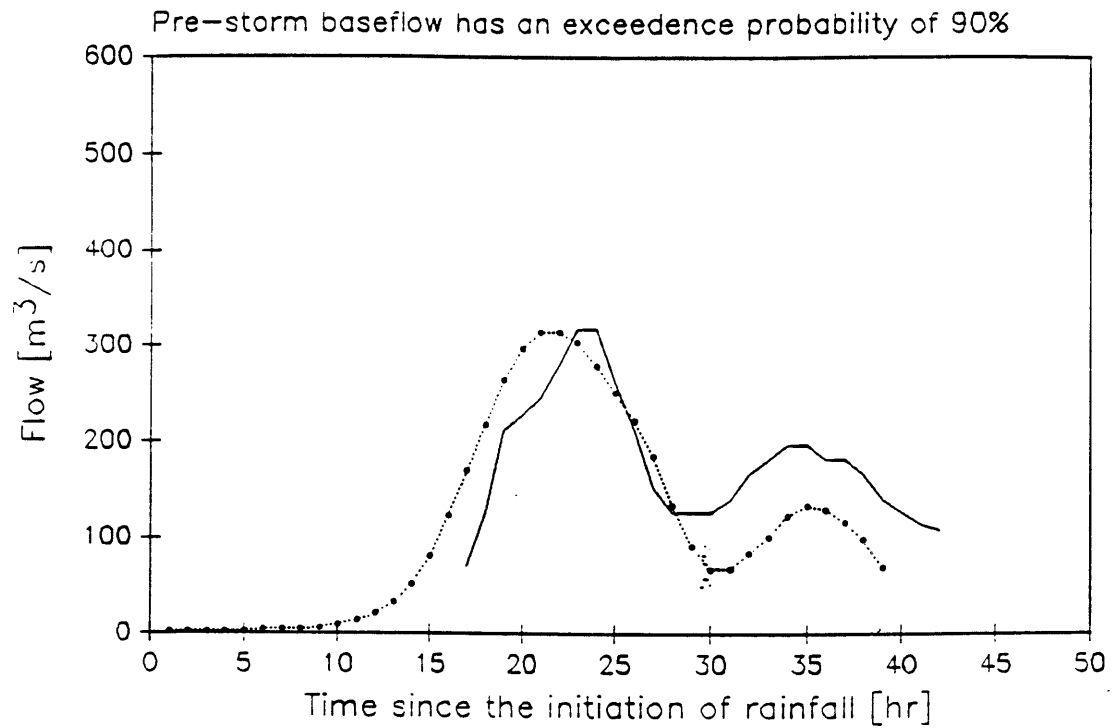
Pre—storm baseflow has an exceedence probability of 90%
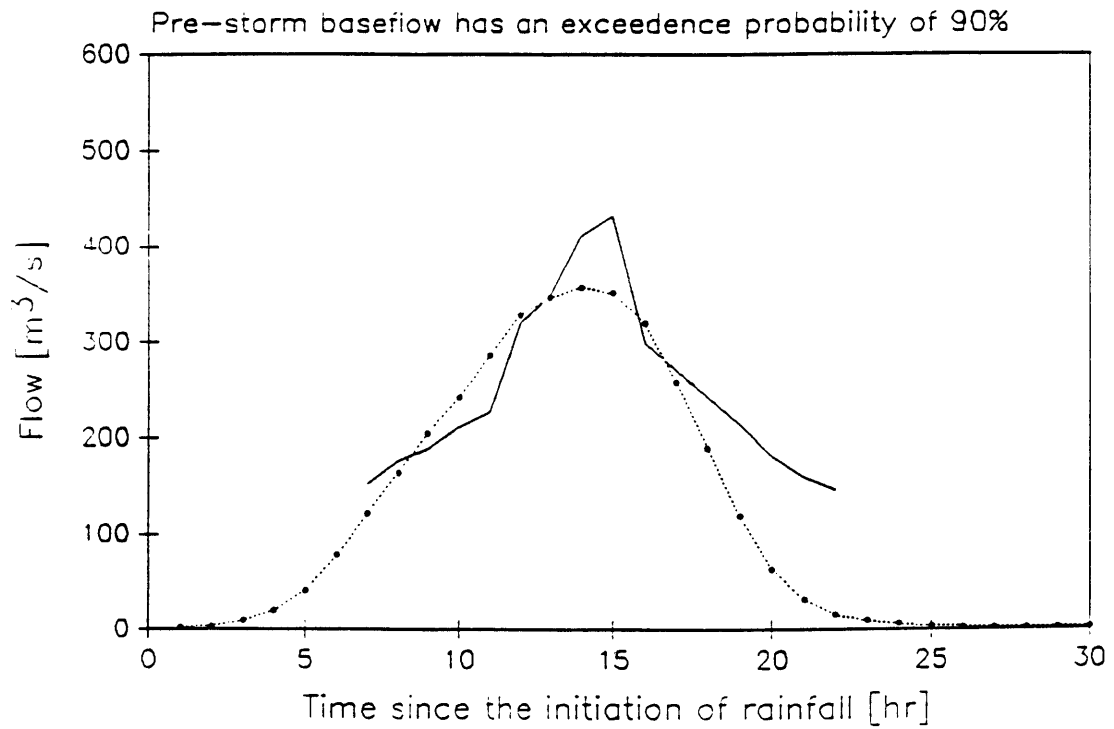
FIGURE 4.43: Observed (solid line) and predicted (dashed line) hydrographs for the storm of January, 1985. Groundwater was initialized in steady-state with the **dry recharge rate** (i. e. that has an exceedence probability of 90%) in the month of January, R_i = 0.0129 mm/hr.

Storm of January, 1985
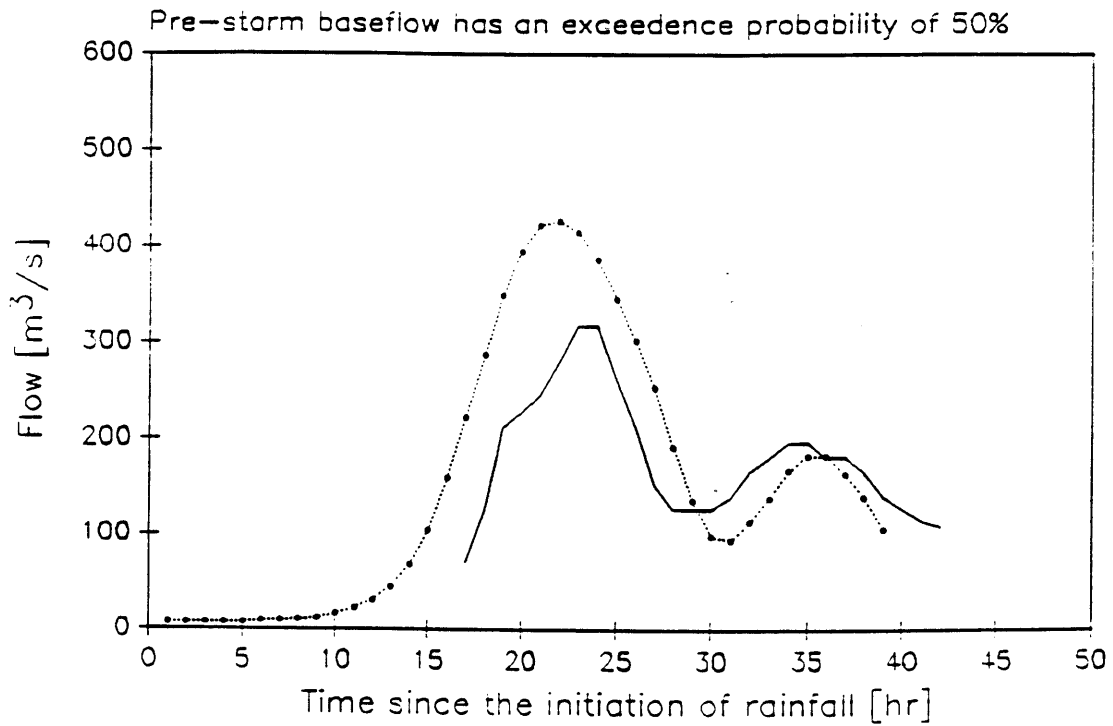
Pre—storm baseflow has an exceedence probability of 50%
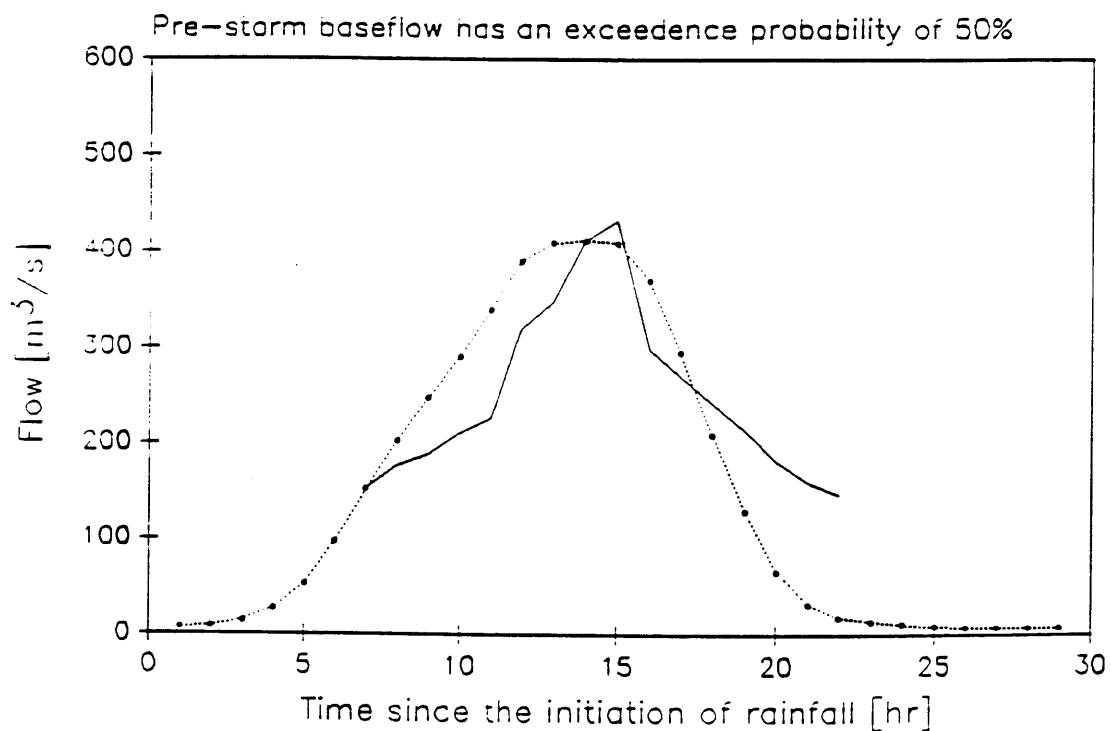
FIGURE 4.44: Observed (solid line) and predicted (dashed line) hydrographs for the storm of January, 1985. Groundwater was initialized in steady-state with the **average recharge rate** (i. e. that has an exceedence probability of 50%) in the month of January, R_i = 0.0321 mm/hr.
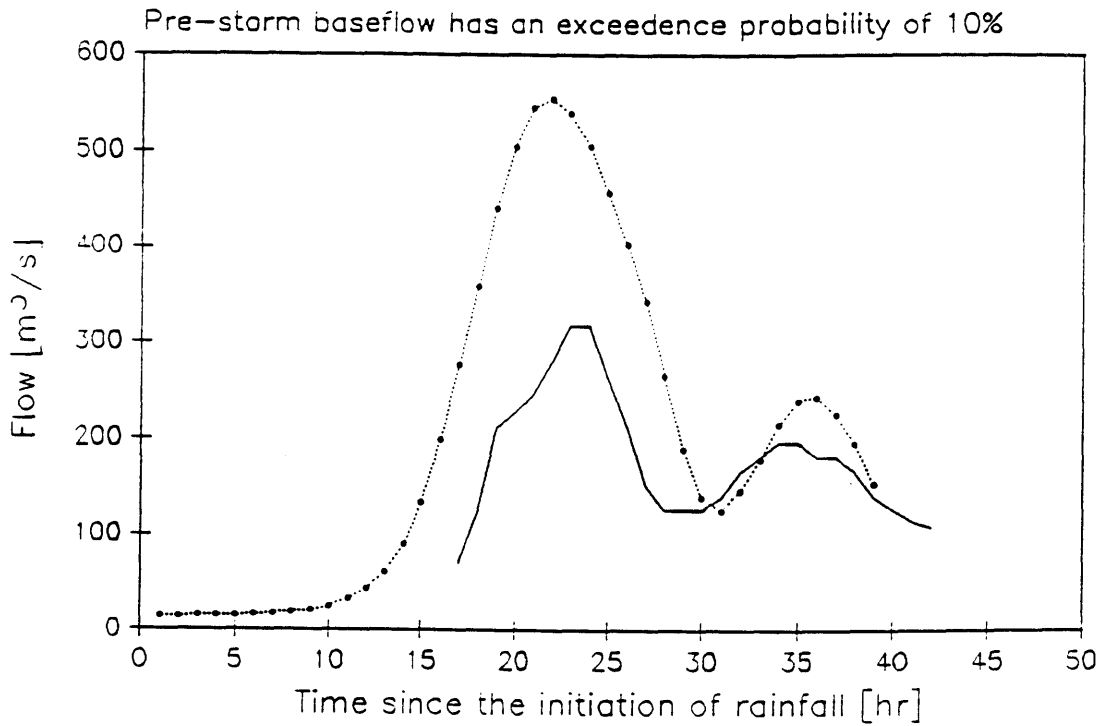
Storm of January, 1985
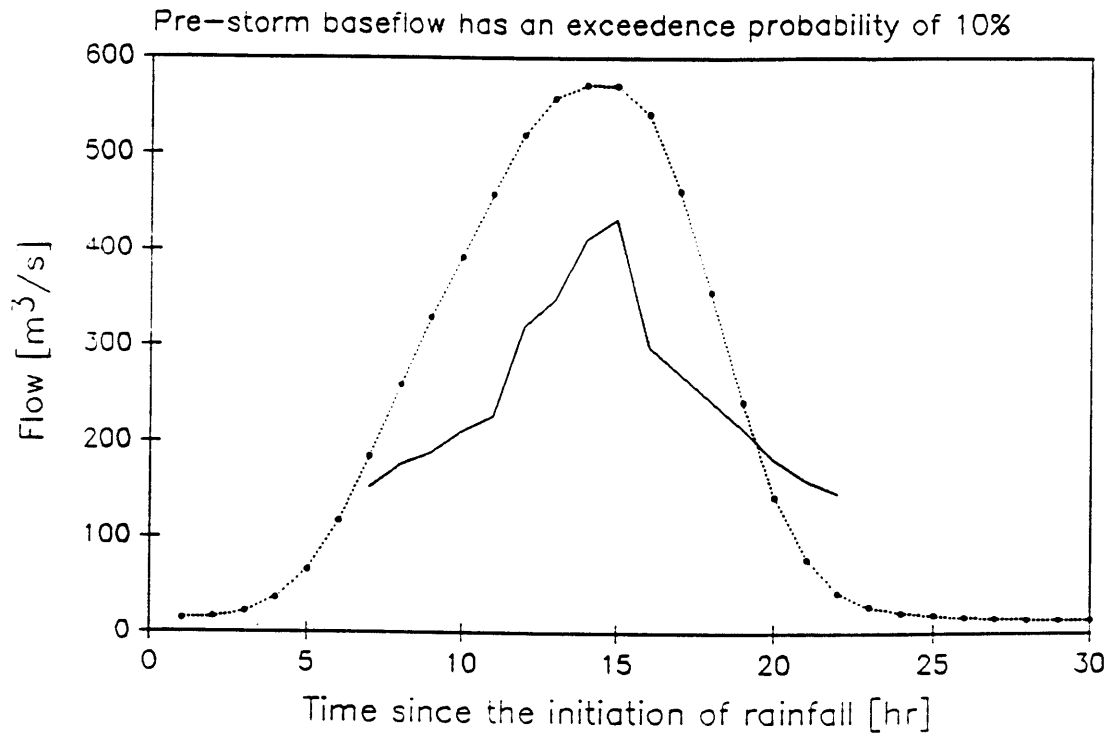
FIGURE 4.45: Observed (solid line) and predicted (dashed line) hydrographs for the storm of January, 1985. Groundwater was initialized in steady-state with the **wet recharge rate** (i. e. that has an exceedence probability of 10%) in the month of January, $R_j = 0.0643$ mm/hr.

Storm of November, 1987
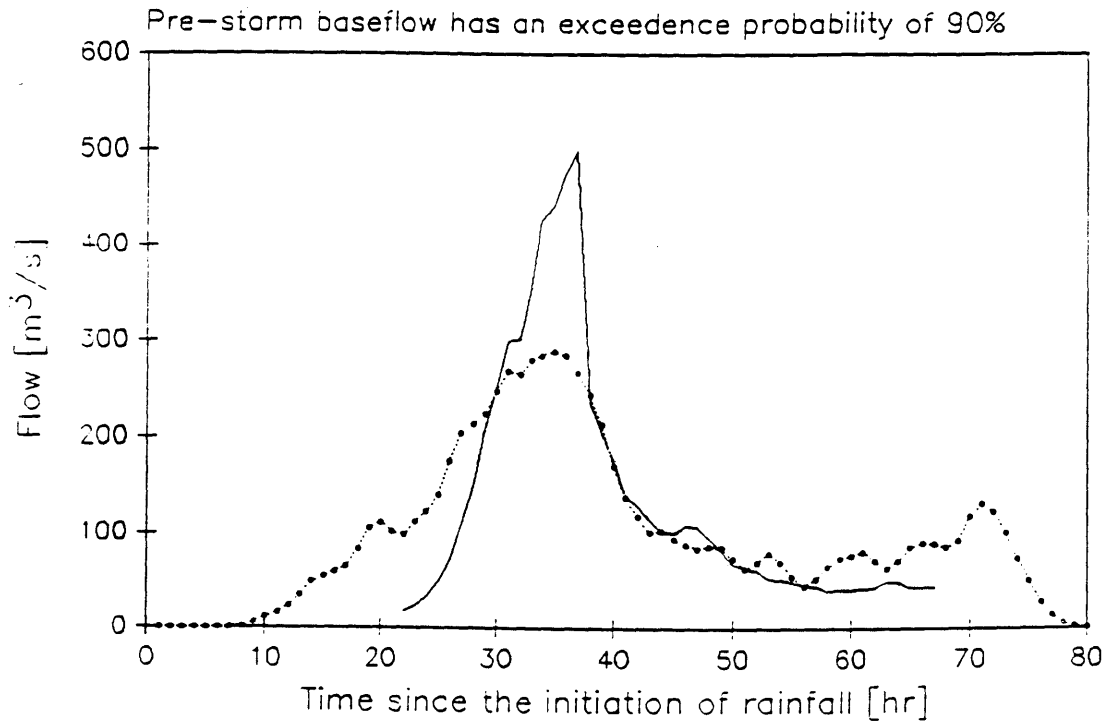
FIGURE 4.46: Observed (solid line) and predicted (dashed line) hydrographs for the storm of November, 1987. Groundwater was initialized in steady-state with the **dry recharge rate** (i. e. that has an exceedence probability of 90%) in the month of November, $R_i = 0.00428$ mm/hr.

Storm of November, 1987
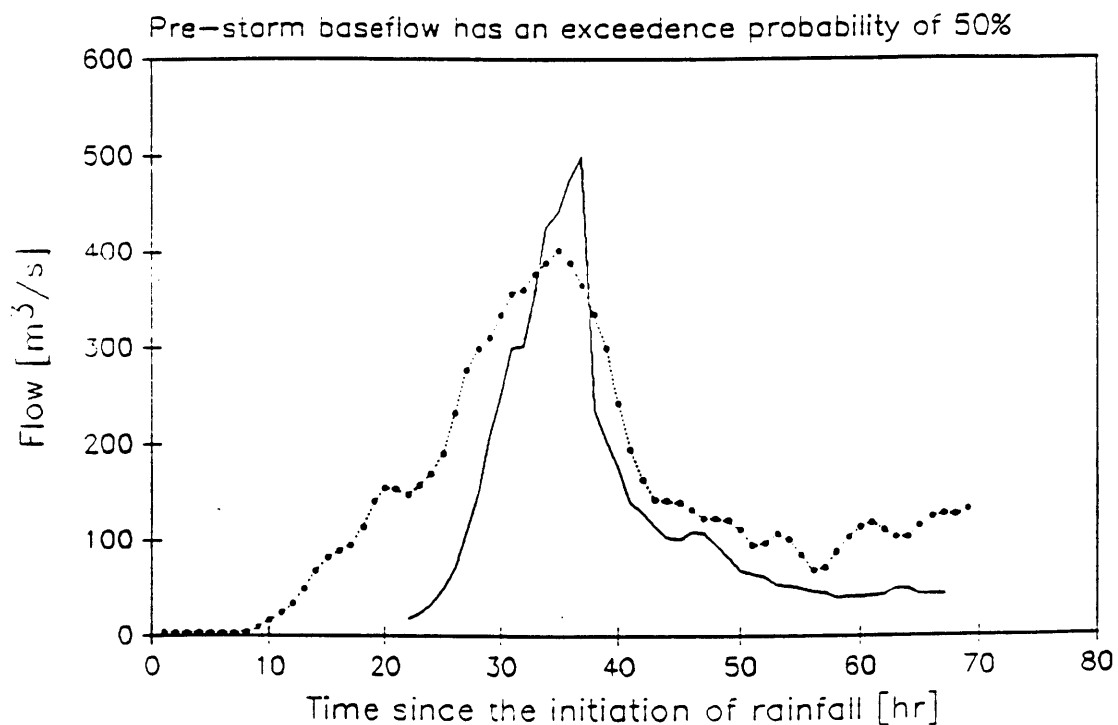
FIGURE 4.47: Observed (solid line) and predicted (dashed line) hydrographs for the storm of November, 1987. Groundwater was initialized in steady-state with the **average recharge rate** (i. e. that has an exceedence probability of 50%) in the month of November, R_i = 0.0171 mm/hr.
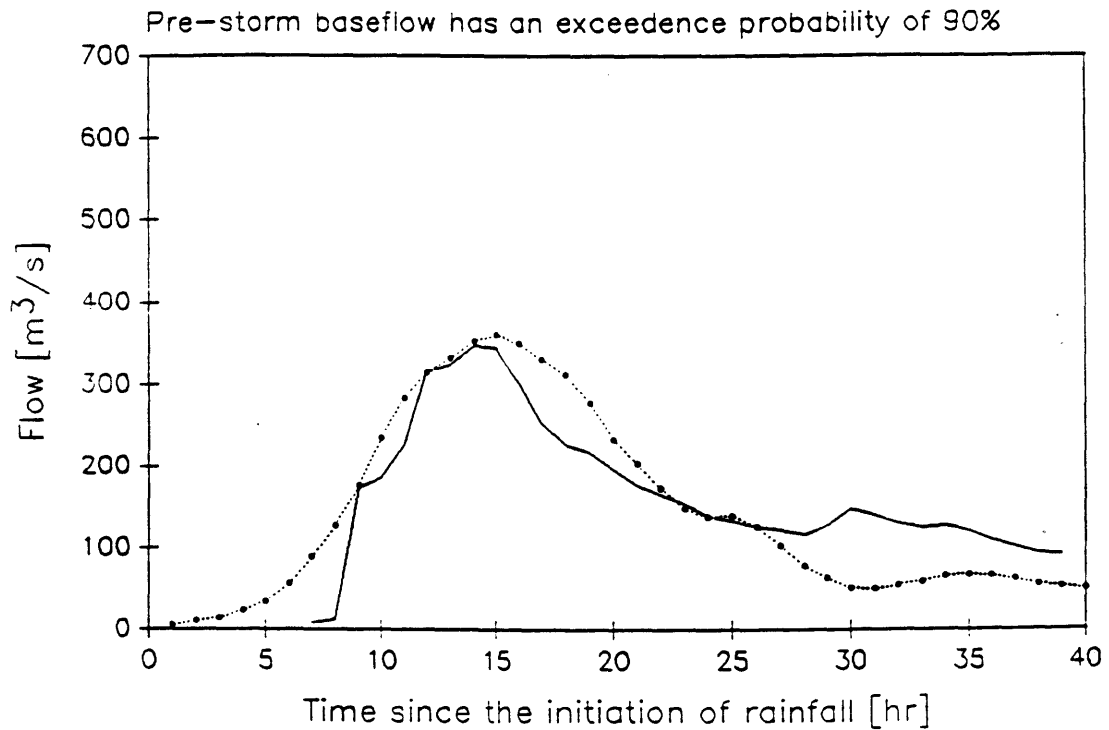
Storm of November, 1987

Pre—storm baseflow has an exceedence probability of 10%
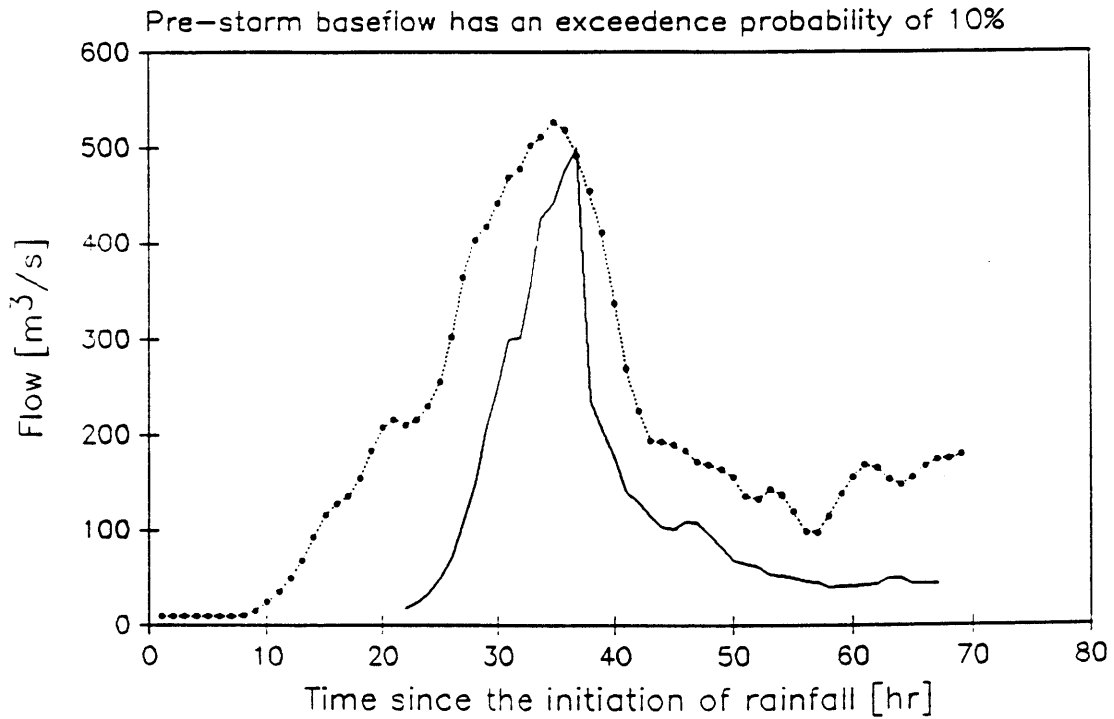
FIGURE 4.48: Observed (solid line) and predicted (dashed line) hydrographs for the storm of November, 1987. Groundwater was initialized in steady-state with the **wet recharge rate** (i. e. that has an exceedence probability of 10%) in the month of November, $R_i = 0.0428$ mm/hr.
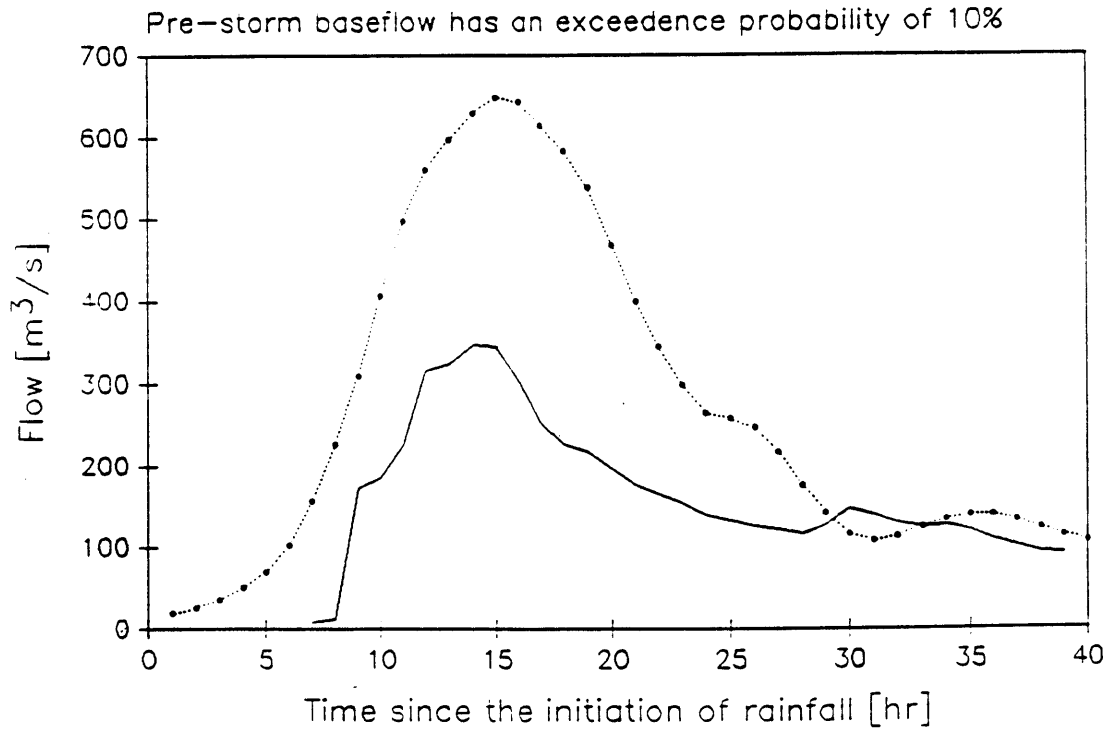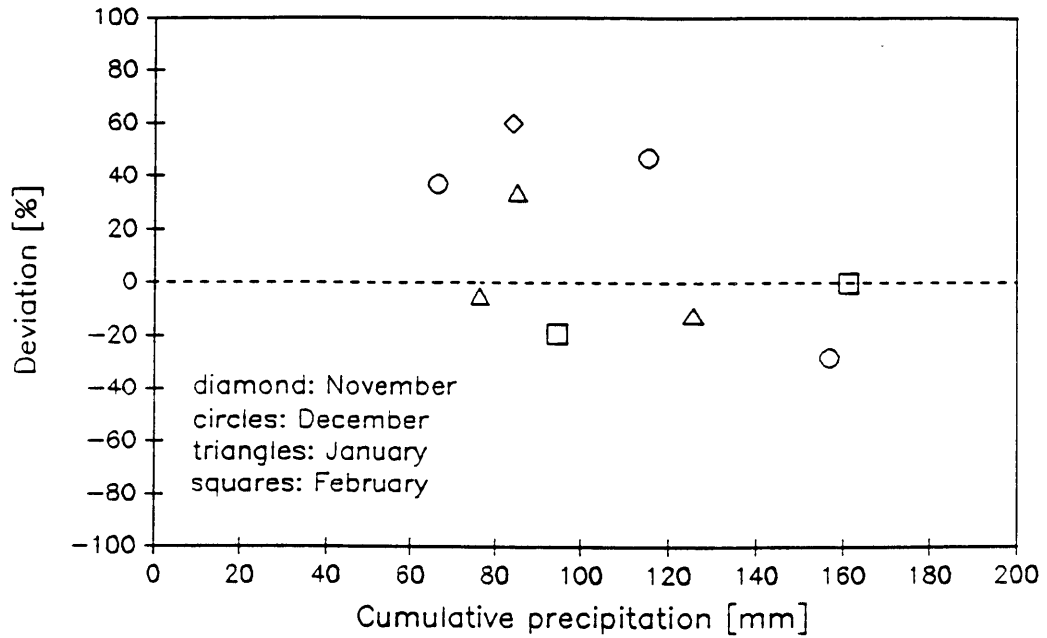
**FIGURE 4.49:** Deviation of predicted from observed peak-flow versus cumulative precipitation in the 30 days preceding the storm. An inverse tendency is suggested in the plot, but the small number of points makes it dificult to derive a definite conclusion.

Chapter 5

SUMMARY AND CONCLUSIONS

5.A SUMMARY OF RESULTS

We have presented a distributed, physically-based model of runoff generation in a catchment, for operational use in flood forecasting. The model accounts for both the infiltration-excess and saturation-excess mechanisms of runoff production, and for lateral subsurface flows. The kinematic approximation is used to model infiltration and subsurface flows. The effect of local terrain slope (obtained from the DEM of the catchment) on subsurface flows and the development of areas of saturated soils is accounted for. The model uses spatial discretization into rectangular elements which correspond to the DEM grid.

The model was applied to the Sieve catchment, in Italy, and used to predict hydrographs for 12 recorded rainfall events. For each event three different initial groundwater conditions were considered, corresponding to a typical dry, average, and wet state of the basin in the month in question. In some of the storms, the dry initial groundwater condition provided the best prediction, in other storms the average initial condition performed best, and yet in others the wet initial condition did best. A dependence of the best initial condition on the antecedent precipitation recorded in the preceding 30 days was investigated. Given the small number of storms,

the investigation was not conclusive. However, the data suggest that the hydrographs of storms with high antecedent precipitation tended to be under-predicted by the average groundwater initialization (50% exceedence probability), which storms with low antecedent precipitation tended to be over-predicted by the average initialization.

Given the data limitations, in particular regarding distributed rainfall data (approximately 75% of the basin area being covered by a single gage in most of the storms studied), and unavailability of hydrograph recession curves for calibration of parameter f, the predictions provided by the model appear to be quite satisfactory. In general, the observed hydrograph was comprehensed between the hydrographs predicted with the dry and wet (90% and 10% exceedence probabilities) initial groundwater conditions, or did not distant themselves far from these predictions.

5.B LIMITATIONS OF THE MODEL

The model presented contains limitations of two different types; those associated with the basic approximations and assumptions made, and those that result from unavailability of data required to calibrate and/or initialize the model. Both types of limitations will be summarized.

Important limitations are associated with the intialization of the moisture profile above the water-table. We recall that the initial unsaturated moisture profile above the water-table is approximated by a function $\theta(R_i, z)$ which assumes that there is a constant rate of

percolation,R_i, at all depths z above the water-table, and that capillary forces play no role in inter-storm subsurface unsaturated flows or in shaping the unsaturated moisture profile. Thus, this moisture intialization does not account for the effects of *evapotranspiration during inter-storm periods*, nor does it represent the profile of the *capillary fringe*. The importance of the capillary fringe in runoff generation has been addressed by various researchers. Abdul *et al.* (1989) have demonstrated how the proximity of the water-table to the surface results in extremely small saturation-deficits, with a very fast rise of water-table level occuring upon a very small amount of infiltration, generating both saturation-excess and fast groundwater discharge.

Sivapalan, M., *et al.* (1988) have suggested an approximation to the initial moisture profile that assumes a situation of equilibrium with the water-table position (no vertical flow). The resulting function of soil moisture with depth, $\theta(Z_{wt},z)$, has a simple form and may be incorporated into the model presented here in a most straightforward manner. The function suggested by Sivapalan *et al.* was not introduced in our model given that it requires the relation between matrix potential, ψ, and moisture content, θ, and this is general not available. However, should the relation $\psi(\theta)$ be known, incorporation of the function $\theta(Z_{wt},z)$ used by Sivapalan *et al.* would be desirable.

We have treated soil porosity, θ_s, and the residual moisture content, θ_r, to be *constant with depth*. In general, however, both these parameters may be expected to vary with depth, and to be correlated with hydraulic conductivity. Beven, *et al.* (1980) fitted analytic forms of $\theta_s(z)$ and $\theta_r(z)$ to measured parameter values, and found reasonable fitting functions. If

such functions are known, the model may benefit from their incorporation.

Finally, water-table initialization assumes water-surface elevations in the stream channels to equal the elevation of the banks. This boundary condition will generally lead to over-prediction of water-table levels and the extent of the zones of saturated soils (i. e. where the water-table is at the soil surface).

5.B SUGGESTIONS FOR FUTURE RESEARCH

Some aspects of the model which have been touched upon but not explored in detail deserve further research. The most important of these aspects is perhaps soil anisotropy. In Appendix A the infiltration model presented in Section 2.B was extended to an anisotropic soil where hydraulic conductivity is higher in the parallel than in the normal direction. Incorporation of the anisotropy ratio into the computation of water-table position involves only substitution of the lateral saturated conductivity, K_{0p}, for K_0. The effect of considering an anisotropy ratio was illustrated in Figure 4.8. However, further studies of sensitivity are required.

In the brief attention dedicated to the subject, it was shown that the ratio of anisotropy affects the rate of decay of the predicted recession curve. Inversely, we suggest that analysis of observed hydrograph recession be used to estimate the anisotropy ratio, a_r. Consideration should also be given to the possibility that a_r be a function of soil depth.

Another aspect of the model which requires improvement is the approximation made of the water-surface elevation in the stream channels by the elevation of the channel banks. While this approximation may be reasonable on a flat floodplain, it may be considerably in error in most instances. If information is not available on water-surface elevations, improved approximations are desirable that relate this variable, for example, to flow contributing area, link magnitude or Strahler order.

Finally, water-table elevations estimated by the model should be validated against observed water-table position. Ideally, field measurements should provide data on water-table depths at different times of the year, and such measurements be used in calibration of parameters f and a_r.

REFERENCES

Abbot, M.B. *et al.*, 1986a, *An introduction to the European Hydrological System - Système Hydrologique Européen, SHE, 1. History and philosophy of a physically-based, distributed model system*, in Hydrol. Sci. Bull. , 1986.

Abbot, M.B. *et al.*, 1986b, *An introduction to the European Hydrological System - Système Hydrologique Européen, SHE, 2. Structure of a physically-based, distributed modeling system*, J. Hydrology, vol.87, 1986, pp 61-77.

Abdul, A. S., and R. W. Gilham, 1984, *Laboratory studies of the effects of the capillary fringe on streamflow generation*, Water Resources Research, vol.20, n.6, pp 691-698.

Ammannati, F., and S. Grassi, 1972, *L'automazione cartografica presso L'Istituto Geografico Militare*, in Boll. Geod. Sci. Affini, vol. 41, no. 3, pp. 215-258. (in Italian)

Andah, K., F. Siccardi, and P. La Barbera, 1987, *Is a drainage network from a digital terrain model a model for the real network ?*, AGU Fall Meeting, San Francisco, December 7-11, 1987.

Anderson, M. G., and T. P. Burt, 1978, *The role of topography in controlling throughflow generation*, in Earth Surface Processes and Landforms, vol.3, pp 331-344.

Atlas, D., and C. W. Ulbrich, 1974, *The physical basis for attenuation-rainfall relationships and the measurement of rainfall parameters by combined attenuation and radar methods*, in J. de Recherche Atmosphérique, n.8, pp 275-298.

Austin, P. M., 1987, *Relation between measured radar reflectivity and surface rainfall*, in <u>Monthly Weather Review</u>, vol.15, n.6, pp 1380-1386.

Band, L. E., 1986, *Topographic partition of watersheds with digital elevation models*, in <u>Water Resources Research</u>, vol. 22, no. 1 , pp 15-24.

Barge, B. L., R. G. Humphries, S. J. Mah, and W. K. Kuhnke, 1979, *Rainfall measurements by weather radar: Applications to hydrology,* in <u>Water Resources Research</u>, vol.15, n.6, pp 1380-1386.

Bathurst, J. C., 1986a, *Physically-based distributed modelling of an upland catchment using the Système Hydrologique Européen*, <u>J. Hydrology</u>, vol.87, pp 79-102.

Bathurst, J. C., 1986b, *Sensitivity analysis of the Système Hydrologique Européen for an upland catchment*, <u>J. Hydrology</u>, vol.87, pp 103-123.

Battan, L. J., 1973, *Radar Observation of the Atmosphere,* University of Chicago Press, 1973.

Bear, J., 1972, <u>Dynamics of Fluids in Porous Media</u>, 764 pp, Dover Publications, Inc., New York.

Becchi, I., E. Caporali, G. Federici and E. Palmisano, 1989, *Un modelo distribuito per lo studio del bacino dell'Arno: analisi idrologica della Sieve,* in <u>Acqua Aria</u>, n. 10, Dec. 1989, Italy. (in Italian)

Becchi, I., F. Castelli, and G. Federici, 1989, *Data bases and geographic information systems: the river flood forecasting project,* International Conference on the Arno Project, Florence, Italy, Nov. 24-25, 1986.

Betson, R. P. 1964, *What is watershed runoff ?*, in <u>J. Geophysical Research</u>, vol. 69 , 1541-1551.

Beven, K. J., 1977, *Experiments with a finite element model of hillslope hydrology - The effect of topography*, in <u>Surface and Subsurface Hydrology</u>, edited by H. J. Morel-Seytoux *et al.*, pp 37-51, Water Resources Publications, Fort Collins, Colo., 1977.

Beven, K. J., and M. Kirkby, 1979, *A physically-based variable contributing area model of basin hydrology*, <u>Hydrol. Sci. Bull.</u>, vol.24, n.1, pp 43-69.

Beven, K. J., 1981, *Kinematic subsurface stormflow*, <u>Water Resources Research</u>, vol. 17, n.5, pp 1419-1424.

Beven, K. J., E. F. Wood, and M. Sivapalan, 1988, *Catchment morphology and catchment response*, <u>J. Hydrology</u>, vol.100, n.1/3.

Beven, K., and J. Zaoui, 1980, *SHE: Towards a methodology for physically-based distributed forecasting in Hydrology*, in "Hydrological Forecasting, Proc. Symposium International Association of Hydrological Sciences, Oxford, U.K., IAHS Publ No. 129, pp 133-137.

Bras, R. L., 1990, <u>Hydrology. An Introduction to Hydrologic Science</u>, Addison-Wesley Publ. Co., 643 pp.

Brooks, R. H., and A. T. Corey, 1964, *Hydraulic properties of porous media,* Hydrology Paper 3, Colorado State University, Fort Collins, Colo., 1964.

Busoni, E., C. Calzolari, and D. Torri, *Utilizzazione della cartografia pedologica per la stima delle caratteristiche idrologiche del suolo*, Gruppo Nazionale per la Difesa dalle Catastrofi Idrogeologiche, Rapporto 1986. (in Italian)

Canuti, P., and P. Tacconi, *Idrogeologia e risorse idriche del bacino del fiume Arno: sottobacini dei fiumi Bisenzio e Sieve*, Univ. degli Studi

di Firenze, Istituto di Geologia e Paleontologia, Italy, May 1975. (in Italian)

Caporali, E., 1988, *Analisi informatica distribuita di un bacino idrografico: i parametri idrologici della Sieve*, Civil Engineering thesis, Facoltá di Ingegneria, Firenze, Italy. (in Italian)

Carrara, A., R. Detti, G. Federici, and V. Pasqui, 1987, *Reticoli idrografici e parametri morfologici di bacino da modelli digitali del terreno*, Consiglio Nazionale delle Ricerche and Gruppo Nazionale per la Difesa dalle Catastrofi Idrogeologiche, Italy. (in Italian)

Carlá, R., A. Carrara, and G. Federici, 1987, *Generazione di modelli digitali del terreno ad alta precisione*, Univ. di Firenze, Dipartimento di Ingegneria Civile, Italy. (in Italian)

Carlá, R., A. Carrara, R. Detti, G. Federici, and V. Pasqui, 1986, *Geographical Information Systems in the assessment fo flood hazards*, International Conference on the Arno Project, Florence, Italy, Nov. 24-25.

Charbeneau, R. J., 1984, *Kinematic models for soil moisture and solute transport,* Water Resources Research, vol.20, n.6, pp 699-706.

C.N.R. Italian National Group for Prevention of Hydro-Geological Disasters, 1986, *The records of the International Conference on the Arno Project*, Florence, Italy, Nov.24-25, 1986.

Collier, C. G., 1986, *Accuracy of rainfall estimates by radar, Part 1: Callibration by telemetering raingauges*, in Journal of Hydrology, n.83, pp 207-223.

Collier, C. G., and J. M. Knowles, 1986, *Accuracy of rainfall estimates by radar, Part II: Applications for short-term flood forecasting*, in J. Hydrology, n.83, pp 237-249.

Collinge, M. and C. Kirkby, Eds., 1987, *Cost 72 and weather radar in Western Europe*, in Weather Radar and Flood Forecasting, 296 pp, John Wiley and Sons, Ltd.

Cooperative Institute for Mesoscale Meteorological Studies, 1982, Proceedings of the NEXRAD Radar Symposium/ Workshop, University of Oklahoma - NOAA, Sept., 1982.

Doviak, R. J., 1983, *A survey of radar rain measurement techniques*, in J. Climate and Applied Meteorology, vol.22, pp 832-849.

Doviak, R. J., and Dusan S. Zrnic, 1984, *Doppler radar and weather observations*, Academic Press Publications, 1984.

Dunne, T., and R. G. Black, 1970a, *Partial area contributions to storm runoff in a small New England watershed*, Water Resources Research, vol.6, n.5, pp 1297-1311.

Dunne, T., and R. G. Black, 1970b, *Experimental investigations of runoff in a small New England watershed*, Water Resources Research, vol.6, n.5, pp 1266-1311.

Entekhabi, D., 1990, *Landsurface Hydrology Parameterization for Atmospheric General Circulation Models: Subgrid Spatial Variability and Sensitivities in a Simple Climate Model*, Ph. D. Thesis, M.I.T. Dpt. Civil Engineering, January 1990.

Freeze, R. A., 1969, *The mechanism of natural groundwater recharge and discharge: 1. One-dimensional, vertical, unsteady, unsaturated flow above a recharging or discharging groundwater flow system*, Water Resources Research, vol.5, n.1, pp 153-171.

Freeze, R. A., 1971, *Three-dimensional, transient, saturated-unsaturated flow in a groundwater basin*, Water Resources Research, vol.7, n.2, pp 347-366.

Freeze, R. A., 1972a, *The role of subsurface flow in generating surface runoff, 1. Base flow contributions to channel flow*, Water Resources Research, v8, n3, pp 609-623.

Freeze, R. A., 1972b, *The role of subsurface lfow in generating surface runoff, 2. Upstream source areas*, Water Resources Research, vol.8, n.5, pp 1272-1283.

Freeze, R. A., 1980, *A stochastic-conceptual analysis of rainfall-runoff processes on a hillslope*, Water Resources Research, vol.16, n.2, pp 391-408.

Green, W. A., and G. A. Ampt, 1911, *Studies in soil physics, I. The flow of air and water through soils*, in J. Agric. Sci., vol. 4, pp 1-24.

Hillel, D., and G. M. Hornberger, 1979, *Physical model of the hydrology of sloping heterogeneous fields*, in Soil Sci. Soc. Am. J., vol.43, n.3, pp 434-439.

Hudlow, M. D., 1988, *Technological developments in real-time operational hydrologic forecasting in the United States*, J. Hydrology, vol.102, n.1/4, pp 69-94.

Hurley, D. G., and G. Pantelis, 1985, *Unsaturated and saturated flow through a thin porous layer on a hillslope*, Water Resources Research, vol. 21, no. 6, pp 821-824.

Kirkby, M., 1988, *Hillslope runoff processes and models*, J. Hydrology, vol.100, n.1/3, pp 315-340.

Kirkby, M. J., 1978, *Hillslope Hydrology*, 389 pp., Wiley-Interscience, New York.

Leopold, L. B., and T. Maddock, Jr., 1953, *The hydraulic geometry of stream channels and some physiographic implications*, U.S. Geological Survey professional paper no. 252, Washington, D. C.

Parlange, J. Y., and R. E. Smith, 1976, *Ponding time for variable rainfall rates*, in Can. J. Soil Sci., vol. 45, pp 121-123.

Philip, J. R., 1957, *Theory of infiltration, 4. Sorptivity and algebraic infiltration equations*, in, Soil Sci., vol.84, n.3, pp 257-264.

Philip, J. R., 1969, *Theory of infiltration*, in Adv. Hydrosci., vol.5, pp 216-296.

Pilgrim, D. H., 1977, *Isochrones of travel time and distribution of flood storage from a tracer study on a small watershed*, in Water Resources Research, vol. 13, no. 3, pp 587-597.

Ragan, R. M., 1968, *An experimental investigation of partial area contribution*, Int. Assoc. Sci. Hydrol., Gen. Assem., Berne, Publ. 76, vol.2, pp 241-249, 1968.

Richards, L. A., 1931, *Capillary conduction of liquids through porous media*, Physics, vol.1, pp 318-333.

Rodriguez-Iturbe, I., M. Gonzalez-Sanabria and R. L. Bras, 1982, *A geomorphoclimatic theory of the instantaneous unit hydrograph*, in Water Resources Research, vol. 18, no. 4, pp 877-886.

Rodriguez-Iturbe, I., and J. B. Valdes, 1979, *The Geomorphologic structure of hydrologic response*, in Water Resources Research, vol. 15, no. 5, pp 1409-1420.

Rogowski, A. S., E. T. Engman, and E. L. Jacoby Jr. 1974, *Transient response of a layered, sloping soil to natural rainfall in the presence of a shallow water table: experimental results,* in Agricultural Res. Serv. Res., Paper ARS-NE-30.

Sklash, M. G., and R. N. Farvolden 1979, *The role of groundwater in storm runoff,* in <u>J. Hydrology,</u> vol.43, pp 45-65.

Smith, J. A., and W. F. Krajewski, 1987, *Statistical modeling of space-time rainfall using radar and rain gage observations*, in <u>Water Resources Research</u>, vol.23, n.10, pp 1893-1900.

Smith, R. E., and R. H. B. Hebbert, 1983, *Mathematical simulation of interdependent surface and subsurface hydrologic processes,* <u>Water Resources Research</u>, vol.19, n.4 , pp 987-1001.

Smith, R. E., and J. Y. Parlange, 1978, *A parameter-efficient hydrologic infiltration model*, in <u>Water Resources Research</u>, vol.14, n.3, pp 533-538.

Smith, R. E., and D. A. Woolhiser, 1971, *Overland flow on an infiltrating surface*, in <u>Water Resources Research</u>, vol.7, n.4, pp 899-913.

Stephenson, G. R. and R. A. Freeze, 1974, *Mathematical simulation of subsurface flow contributions to snowmelt runoff, Reynolds Creek Watershed, Idaho*, <u>Water Resources Research</u>, vol.10, n2, pp 284-298.

Tarboton, 1989, *The Analysis of River Basins and Channel Networks using Digital Terrain Data*, Ph. D. Thesis, M.I.T. Dpt. Civil Engineering, September 1989.

Wilson, J. W., and Edward A. Brandes, 1979, *Radar measurement of rainfall - A summary*, in <u>Bulletin of the American Society</u>, vol.60, n.9, pp 1048-1058.

Wyss, J., E. R. Williams, and R. L. Bras, 1990, *Hydrologic modeling of New England river basins using radar rainfall data*, in <u>J. Geophysical Research</u>, vol. 95, no. D3.

Wyss, J. D., 1988, *Hydrologic Modeling of New England River Basins Using Radar Rainfall Data,* M. S. Thesis, M.I.T. Dpt. of Earth, Atmospheric and Planetary Sciences, Jan 1988.

APPENDIX A: KINEMATIC INFILTRATION IN A VERTICALLY HETEROGENEOUS, ANISOTROPIC, SLOPED SOIL

In this Appendix we expand the analysis performed in Section 2.B to an anisotropic soil. Many natural soils are anisotropic with conductivity in the direction normal to the surface less than in the parallel direction, a condition termed *lateral isotropy*. Here we consider infiltration in a soil where saturated hydraulic conductivity is higher in the *p* direction than in the *n* direction (see Figure-caption 2.2 in Section 2.B for definition of coordinate directions). The conductivity in any direction decreases exponentially with depth in the vertical direction, *z*. This condition is particularly prone to the generation of lateral subsurface flow, given that it combines two features, heterogeneity and anisotropy, capable of laterally diverting infiltration.

i) Soil parameterization and moisture initialization

Saturated hydraulic conductivity in both the parallel and normal directions decreases exponentially with depth,

$$K_{s_p}(z) = K_{0_p} \cdot e^{-f \cdot z} \tag{A.1}$$

$$K_{s_n}(z) = K_{0_n} \cdot e^{-f \cdot z} \tag{A.2}$$

where $K_{s_p}(z)$ and $K_{s_n}(z)$ are the saturated conductivities in the p and n directions at depth z; K_{0_p} and K_{0_n} are the saturated hydraulic conductivities in the p and n directions at the soil surface; and f is a parameter of dimension L^{-1}.

The saturated hydraulic conductivities in the p and n directions are related through the dimensionless anisotropy ratio, a_r, defined as

$$\frac{K_{s_p}(z)}{K_{s_n}(z)} = \frac{K_{0_p}}{K_{0_n}} = a_r > 1 \tag{A.3}$$

Assuming the same Brooks-Corey parameterization in all directions then the unsaturated hydraulic conductivities are

$$K_p(\theta,z) = K_{0_p} \cdot e^{-f \cdot z} \cdot \left(\frac{\theta - \theta_r}{\theta_s - \theta_r} \right)^\varepsilon \tag{A.4}$$

$$K_n(\theta,z) = K_{0_n} \cdot e^{-f \cdot z} \cdot \left(\frac{\theta - \theta_r}{\theta_s - \theta_r} \right)^\varepsilon \tag{A.5}$$

and we have, for unsaturated soils as well,

$$\frac{K_p(\theta,z)}{K_n(\theta,z)} = \frac{K_{0_p}}{K_{0_n}} = a_r \tag{A.6}$$

As in Section 2.B, the initial moisture condition is determined by an antecedent rate of recharge, R_i.

194

ii) Unsaturated infiltration

The wetting front is unsaturated for rainfall rates lower than the surface saturated conductivity, and for wetting front depths smaller than the critical depth $Z^*(R)$. *All equations derived under point ii) are for $z < Z_f$ with $Z_f < Z^*(R)$.* Letting $K(\theta,z)=R$ and $\theta=\theta_s$ in (A.5) and solving for z, we obtain the expression for $Z^*(R)$,

$$Z^*(R) = \frac{1}{f} \cdot \ln\left(\frac{K_{0_N}}{R}\right) \tag{A.7}$$

For an anisotropic soil sloped at an angle α, we can write the expressions for the components of unsaturated flow in the main directions of anisotropy, by considering the components of the gravitational gradient vector $J_z = 1.0$ in those directions,

$$J_p = \sin(\alpha) ; \qquad q_p = J_p \cdot K_p(\theta,z) \tag{A.8}$$

$$J_n = \cos(\alpha) ; \qquad q_n = J_n \cdot K_n(\theta,z) \tag{A.9}$$

Soil anisotropy determines that flow be at an angle, α'', with the vertical direction. Figure A.1 represents the geometrical situation from which we can write (using Equations (A.6), (A.8) and (A.9)),
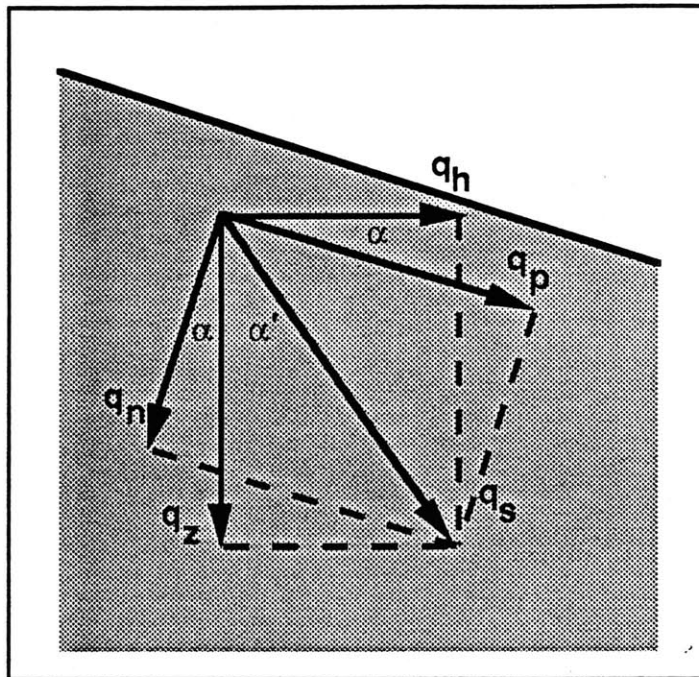
FIGURE A.1: Components of flow in the z and h, and p and n directions. Flow is in the direction indicated by *s*.

$$(\alpha+\alpha") = \tan^{-1}\left(\frac{q_p}{q_n}\right) = \tan^{-1}(a_r{\cdot}\tan(\alpha))$$

and solving for $\alpha"$,

$$\alpha" = \tan^{-1}(a_r{\cdot}\tan(\alpha)) - \alpha, \tag{A.10}$$

Angle $\alpha"$ is larger for higher anisotropy ratios and higher terrain slopes. Note that for $a_r = 1$ (A.10) gives $\alpha"$ equal to zero. That is, for an isotropic soil, the above equations give unsaturated flow in the vertical direction, as expected.

Angle $\alpha"$ is needed for computation of the unsaturated flow rate. Designating the direction of flow by s, we can derive an expression for q_s from continuity considerations. Let us consider rainfall at a rate R over a unit horizontal surface area, and its infiltration into the soil. Figure A.2 represents a cross-sectional area. From continuity, the flow per unit width perpendicular to segment a (which has unit length) must equal the flow per unit width perpendicular to segment b i.e.,

$$R \cdot 1.0 = q_s \cdot b \tag{A.11}$$

From geometrical considerations, we can write

$$b = \frac{\cos(\alpha+\alpha")}{\cos(\alpha)} \tag{A.12}$$

Substituting (A.12) into (A.11) and solving for q_s we obtain
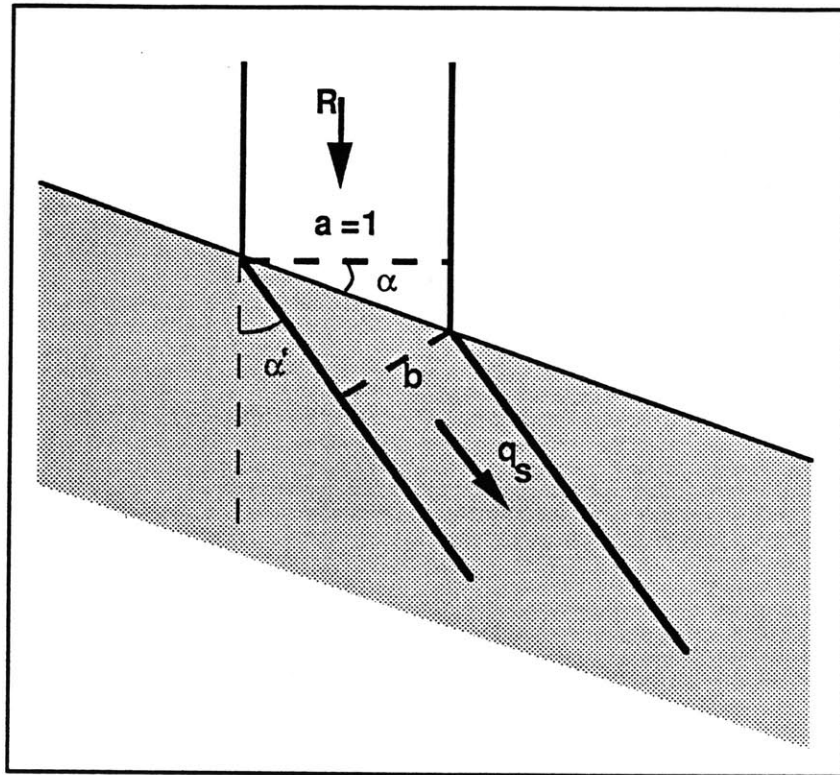
FIGURE A.2: Unsaturated infiltration in a laterally isotropic soil.

$$q_s = \frac{\cos(\alpha)}{\cos(\alpha+\alpha")} \cdot R \tag{A.13}$$

We will define

$$\xi = \frac{\cos(\alpha)}{\cos(\alpha+\alpha")} \tag{A.14}$$

($\xi > 1.0$ for $a_r > 1.0$)

and thus we can write

$$q_s = \xi \cdot R \tag{A.15}$$

From q_s we can finally derive, from geometrical considerations, the expressions for the vertical and horizontal components of flow,

$$q_z = \cos(\alpha") \cdot q_s$$

$$= \cos(\alpha") \cdot \xi \cdot R \tag{A.16}$$

$$q_h = \sin(\alpha") \cdot q_s$$

$$= \sin(\alpha") \cdot \xi \cdot R \tag{A.17}$$

The lateral component of flow increases with $\alpha"$ and thus is larger for higher slopes and higher anisotropy ratios.

We can find $\theta(R,z)$ by noting that

$$q_n = \cos(\alpha + \alpha'') \cdot q_s$$

$$= \cos(\alpha) \cdot R \tag{A.18}$$

Equating (A.18) to (A.9) we obtain $K_n(\theta, z) = R$. Letting $K_n(\theta, z) = R$ in (A.5) and solving for $\theta(R,z)$ we obtain

$$\theta(R,z) = \left(\frac{R}{K_{0_n}}\right)^{\frac{1}{\epsilon}} \cdot (\theta_s - \theta_r) \cdot e^{\frac{f}{\epsilon} \cdot z} + \theta_r \tag{A.19}$$

Note that the soil saturates at the surface ($\theta = \theta_s$) for a rainfall rate equal to the surface saturated conductivity in the normal direction, K_{0_n}.

From derivation similar to that for (A.16), we have below the wetting front (i.e., for $z > Z_f$),

$$q_z(R_i) = \cos(\alpha'') \cdot \xi \cdot R_i \tag{A.20}$$

Through a derivation analogous to that for the equation of evolution of Z_f in Section 2.B, point ii), and upon substitution of (A.16) and (A.20), we obtain

$$\frac{dZ_f}{dt} = \frac{R - R_i}{\theta(R, Z_f) - \theta(R_i, Z_f)} \tag{A.21}$$

iii) Saturated infiltration

Saturated infiltration occurs when either the rainfall rate is higher than the surface saturated conductivity; or the wetting front has penetrated beyond the critical depth $Z^*(R)$. *The equations derived under point iii) are for $Z_t \leq z \leq Z_f$*

For the reasons seen in 2.B based on continuity considerations, the normal component of flow within the saturated zone is limited by flow at the wetting front, and therefore $q_n(z)$ is a constant for $Z_t \leq z \leq Z_f$. Thus,

$$q_n(z) = q_n(Z_f) \tag{A.22}$$

At the wetting front, we have $J_z(Z_f) = 1$ and

$$J_n^{'}(Z_f) = \cos(\alpha) \cdot J_z(Z_f) = \cos(\alpha) \ ; \tag{A.23}$$

$$q_n(Z_f) = J_n(Z_f) \cdot K_{s_n}(Z_f) = \cos(\alpha) \cdot K_{0_n} \cdot e^{-f \cdot Z_f} \tag{A.24}$$

Substituting (A.24) in (A.22), we obtain

$$q_n(z) = \cos(\alpha) \cdot K_{0_n} \cdot e^{-f \cdot Z_f} \tag{A.25}$$

The potential gradient, and the flow, in the parallel direction are derived as follows,

201

$$J_p(z) \equiv -\frac{\partial \Phi(p,n)}{\partial p} = -\frac{\partial}{\partial p}\left[e(p,n) + \frac{P(n)}{\gamma} \right]$$

$$= \sin(\alpha) - \frac{dn}{dp} \cdot \frac{\partial}{\partial n} \frac{P(n)}{\gamma} = \sin(\alpha) \qquad \text{(A.26)}$$

and

$$q_p(z) = J_p(z) \cdot K_{s_p}(z) = \sin(\alpha) \cdot K_{0_p} \cdot e^{-f \cdot z} \qquad \text{(A.27)}$$

As in part ii) and using (A.25) and (A.27), we can write

$$\tan(\alpha + \alpha'(z)) = \frac{q_p(z)}{q_n(z)} = \tan(\alpha) \cdot a_r \cdot e^{f \cdot (Z_f - z)}$$

and solving for $\alpha''(z)$,

$$\alpha'(z) = \tan^{-1}\left[\tan(\alpha) \cdot a_r \cdot e^{f \cdot (Z_f - z)} \right] - \alpha , \qquad \text{(A.28)}$$

From geometrical considerations, we have

$$q_h(z) = \frac{\sin(\alpha'(z))}{\sin(\alpha + \alpha'(z))} \cdot q_p(z) \qquad \text{(A.29)}$$

Substituting (A.27) in (A.29) we obtain for $q_h(z)$

$$q_h(z) = \frac{\sin(\alpha) \cdot \sin(\alpha'(z))}{\sin(\alpha + \alpha'(z))} \cdot K_{0_p} \cdot e^{-f \cdot z} \qquad \text{(A.30)}$$

202

From geometrical considerations, we have

$$q_z(z) = \frac{\cos(\alpha'(z))}{\cos(\alpha+\alpha'(z))} \cdot q_n(z)$$

(A.31)

Substituting (A.25) in (A.32) we obtain for $q_z(z)$

$$q_z(z) = \frac{\cos(\alpha) \cdot \cos(\alpha'(z))}{\cos(\alpha+\alpha'(z))} \cdot K_{0_n} \cdot e^{-f \cdot Z_f}$$

(A.32)

At the wetting front (i.e. making $z=Z_f$), Equation (A.28) equals Equation (A.10), i.e. $\alpha'(Z_f)$ equals the angle of unsaturated flow, α'', which does not depend on z. Thus, for $z = Z_f$ (A.32) becomes

$$q_z(Z_f) = \cos(\alpha'') \cdot \xi \cdot K_{0_n} \cdot e^{-f \cdot Z_f}$$

(A.33)

A derivation analogous to that for dZ_f/dt in Section 2.B leads to the following, upon substitution of (A.33) and (A.20)

$$\frac{dZ_f}{dt} = \frac{K_{0_n} \cdot e^{-f \cdot Z_f} - R_i}{\theta_s - \theta(R_i, Z_f)}$$

(A.34)

A derivation analogous to that for dZ_t/dt in Section 2.B leads to the following, upon substitution of (A.33) and (A.16)

$$\frac{dZ_t}{dt} = \frac{K_{0_n} \cdot e^{-f \cdot Z_f} - R}{\theta_s - \theta(R_i, Z_t)}$$

(A.35)

iv) Summary of computations in one element

The general expression for the volumetric discharge from an element to the element located downslope from it is

$$Q_{out} = W \cdot \int_0^{Z_f} q_h(z) \cdot dz \tag{A.36}$$

Upon substitution of Equations (A.17) and (A.30), (A.36) becomes

$$Q_{out} = W \cdot \left[\int_0^{Z_t} \sin(\alpha'') \cdot \xi \cdot R \cdot Z_t \cdot dz + \int_{Z_t}^{Z_f} \frac{\sin(\alpha) \cdot \sin(\alpha'(z))}{\sin(\alpha + \alpha'(z))} \cdot K_{0_p} \cdot e^{-f \cdot z} \cdot dz \right] \tag{A.37}$$

Upon substitution of Equation (A.28) for $\alpha'(z)$ for $Z_t \leq z \leq Z_f$ in Equation (A.37) we derive (see derivation in Appendix B, part ii)).

$$Q_{out} = W \cdot \left[\sin(\alpha'') \cdot \xi \cdot R \cdot Z_t + \right.$$

$$\left. K_{0_p} \cdot \cos(\alpha) \cdot \sin(\alpha) \cdot e^{-f \cdot Z_f} \cdot \left[\frac{1}{f} \cdot (e^{f \cdot (Z_f - Z_t)} - 1) - (Z_f - Z_t) \right] \right] \tag{A.38}$$

Below we summarize the computations in one element. In the equations below, A designates element area. Estimation of Q_{in} is achieved through the element coupling scheme which is explained in Section 3.B.

$$\frac{dM_t}{dt} = \frac{dZ_f}{dt} \cdot \theta(R_i, Z_f) + Min(R, K_{0_n}) + \frac{Q_{in} - Q_{out}}{A}$$

$$\frac{dZ_f}{dt} = \begin{cases} \text{unsaturated: } & \dfrac{R_e - R_i}{\theta(R_e,Z_f) - \theta(R_i,Z_f)} \\[3em] \text{saturated: } & \dfrac{K_{0_n} \cdot e^{-f \cdot Z_f} - R_i}{\theta_s - \theta(R_i,Z_f)} \end{cases}$$

$$\frac{dZ_t}{dt} = \begin{cases} \text{unsaturated: } & \dfrac{dZ_f}{dt} \\[3em] \text{saturated: } & \dfrac{K_{0_n} \cdot e^{-f \cdot Z_f} - R_e}{\theta_s - \theta(R_e,Z_t)} \end{cases}$$

where

$$R_e = K_{0_n} \cdot \left(\frac{M_u - \theta_r \cdot Z_t}{(\theta_s - \theta_r) \cdot \left(\dfrac{\varepsilon}{f}\right) \cdot (e^{\frac{f}{\varepsilon} \cdot Z_t} - 1)} \right)^{\varepsilon}$$

$$M_u = M_t - \theta_s \cdot (Z_f - Z_t)$$

$$\theta(R,z) = \left(\frac{R}{K_{0_n}} \right)^{\frac{1}{\varepsilon}} \cdot (\theta_s - \theta_r) \cdot e^{\frac{f}{\varepsilon} \cdot z} + \theta_r$$

$$Q_{out} = W \cdot \left\lfloor \sin(\alpha'') \cdot \xi \cdot R \cdot Z_t + \right.$$

$$\left. K_{0_p} \cdot \cos(\alpha) \cdot \sin(\alpha) \cdot e^{-f \cdot Z_f} \cdot \left[\frac{1}{f} \cdot (e^{f \cdot (Z_f - Z_t)} - 1) - (Z_f - Z_t) \right] \right]$$

$$\alpha'' = \tan^{-1}(a_r \cdot \tan(\alpha)) - \alpha$$

APPENDIX B: SOLUTIONS OF THE INTEGRALS IN THE EXPRESSION FOR LATERAL DISCHARGE FROM AN ELEMENT

In this Appendix we present the solution of the integrals in Equations (3.3) and (A.37) leading to Equations (3.3) and (A.38), respectively.

i) Solution of the integral in Equation (3.3) for lateral discharge from an isotropic element

Equation (3.3) is repeated here as (B.1),

$$Q_{out} = W \cdot \int_{Z_t}^{Z_f} \frac{\tan(\alpha) \cdot \tan(\alpha'(z))}{\tan(\alpha) + \tan(\alpha'(z))} \cdot K_0 \cdot e^{-f \cdot z} \cdot dz \qquad (B.1)$$

The expression for the tangent of the sum of two angles, α and β, (see e.g. Simmons, 1985) is

$$\tan(\alpha + \beta) = \frac{\tan(\alpha) + \tan(\beta)}{1 - \tan(\alpha) \cdot \tan(\beta)} \qquad (B.2)$$

From (B.2), we can write

$$\tan(\alpha + \alpha'(z)) = \frac{\tan(\alpha) + \tan(\alpha'(z))}{1 - \tan(\alpha) \cdot \tan(\alpha'(z))} \qquad (B.3)$$

From (B.3), the ratio in (B.1) can be written in the following form,

$$\frac{\tan(\alpha)\cdot\tan(\alpha'(z))}{\tan(\alpha)+\tan(\alpha'(z))} = \frac{1}{\tan(\alpha)+\tan(\alpha'(z))} - \frac{1}{\tan(\alpha+\alpha'(z))} \tag{B.4}$$

and Equation (B.1) becomes

$$Q_{out} = W\cdot\int_{Z_t}^{Z_f}\left[\frac{1}{\tan(\alpha)+\tan(\alpha'(z))} - \frac{1}{\tan(\alpha+\alpha'(z))}\right]\cdot K_0\cdot e^{-f\cdot z}\cdot dz$$

or

$$Q_{out} = W\cdot K_0\cdot\left[\int_{Z_t}^{Z_f}\frac{1}{\tan(\alpha)+\tan(\alpha'(z))}\cdot e^{-f\cdot z}\cdot dz\right.$$

$$\left.+\int_{Z_t}^{Z_f}\frac{1}{\tan(\alpha+\alpha'(z))}\cdot e^{-f\cdot z}\cdot dz\right] \tag{B.5}$$

To solve the <u>first integral in (B.5)</u> we must substitute an expression for $\tan(\alpha'(z))$. Substituting Equation (2.25) for $\alpha'(z)$, we have

$$\tan(\alpha'(z)) = \tan[\tan^{-1}(e^{f\cdot(Z_f-z)}\cdot\tan(\alpha)) - 1] \tag{B.6}$$

From expression (B.2) for the tangent of the sum of two angles, (B.6) becomes

$$\tan(\alpha'(z)) = \frac{e^{f\cdot(Z_f-z)}\cdot\tan(\alpha) - \tan(\alpha)}{1 + e^{f\cdot(Z_f-z)}\cdot\tan^2(\alpha)} \tag{B.7}$$

207

Upon substitution of (B.7), the first integral in (B.5) becomes

$$\int_{Z_t}^{Z_f} \frac{1}{\tan(\alpha) + \dfrac{e^{f \cdot (Z_f - z)} \cdot \tan(\alpha) - \tan(\alpha)}{1 + e^{f \cdot (Z_f - z)} \cdot \tan^2(\alpha)}} \cdot e^{-f \cdot z} \cdot dz$$

Upon simplification of the integrand expression and final integration,

$$\int_{Z_t}^{Z_f} \frac{1 + e^{f \cdot (Z_f - z)} \cdot \tan^2(\alpha)}{\tan(\alpha) \cdot e^{f \cdot Z_f} \cdot (\tan^2(\alpha) + 1)} \cdot dz$$

$$= \frac{(Z_f - Z_t) + \tan^2(\alpha) \cdot \dfrac{1}{f} \cdot (e^{f \cdot (Z_f - Z_t)} - 1)}{\tan(\alpha) \cdot e^{f \cdot Z_f} \cdot (\tan^2(\alpha) + 1)} \quad\quad\quad (B.8)$$

Solving Equation (2.25) for $(\alpha + \alpha'(z))$, we obtain

$$\tan(\alpha + \alpha'(z)) = e^{f \cdot (Z_f - z)} \cdot \tan(\alpha)$$

To solve the <u>second integral in (B.5)</u> we must substitute the expression for $\tan(\alpha + \alpha'(z))$. Substituting the above expression for $\tan(\alpha + \alpha'(z))$ in (B.5), the integral becomes

$$\int_{Z_t}^{Z_f} \frac{1}{e^{f \cdot (Z_f - z)} \cdot \tan(\alpha)} \cdot e^{-f \cdot z} \cdot dz \quad\quad\quad (B.9)$$

208

Upon simplification of the integrand expression and final integration,

$$\int_{Z_t}^{Z_f} \frac{1}{e^{f \cdot Z_f} \cdot \tan(\alpha)} \cdot dz$$

$$= \frac{Z_f - Z_t}{e^{f \cdot Z_f} \cdot \tan(\alpha)} \tag{B.10}$$

Substituting (B.8) and (B.10) for the two integrals in (B.5), and upon simplification, we obtain the final expression, which was presented also as Equation (3.3)

$$Q_{out} = W \cdot K_0 \cdot \frac{\tan(\alpha)}{\tan^2(\alpha) + 1} \cdot e^{-f \cdot Z_f} \left[\frac{1}{f} \cdot (e^{f \cdot (Z_f - Z_t)} - 1) - (Z_f - Z_t) \right]$$

and given that we have $\tan^2(\alpha) + 1 = \dfrac{1}{\cos^2(\alpha)}$, the above equation becomes

$$Q_{out} = W \cdot K_0 \cdot \cos(\alpha) \cdot \sin(\alpha) \cdot e^{-f \cdot Z_f} \left[\frac{1}{f} \cdot (e^{f \cdot (Z_f - Z_t)} - 1) - (Z_f - Z_t) \right] \tag{B.11}$$

ii) Solution of the integral in Equation (A.37) for lateral discharge from an anisotropic element

Equation (A.37) is repeated here as (B.12)

$$Q_{out} = W \cdot \left[\int_0^{Z_t} \sin(\alpha'') \cdot \xi \cdot R \cdot dz + \int_{Z_f}^{Z_t} \frac{\sin(\alpha) \cdot \sin(\alpha'(z))}{\sin(\alpha + \alpha'(z))} \cdot K_{0_p} \cdot e^{-f \cdot z} \cdot dz \right] \tag{B.12}$$

The ratio in the second integral of (B.12) is in fact equal to the ratio in the integral of (B.1), as shown next. Upon substitution of the formula for the sine of the sum of two angles and dividing numerator and denominator by $(\cos(\alpha) \cdot \cos(\alpha'))$,

$$\frac{\sin(\alpha) \cdot \sin(\alpha'(z))}{\sin(\alpha + \alpha'(z))} = \frac{\sin(\alpha) \cdot \sin(\alpha'(z))}{\sin(\alpha) \cdot \cos(\alpha'(z)) + \cos(\alpha) \cdot \sin(\alpha'(z))}$$

$$= \frac{\tan(\alpha) \cdot \tan(\alpha'(z))}{\tan(\alpha) + \tan(\alpha'(z))} \tag{B.13}$$

Given the similarity between the second integral in (B.12) and the integral in (B.1), their solution is alike and we obtain (B.14), which was given as Equation (A.38),

$$Q_{out} = W \cdot [\ \sin(\alpha") \cdot \xi \cdot R \cdot Z_t +$$

$$K_{Q_p} \cdot \cos(\alpha) \cdot \sin(\alpha) \cdot e^{-f \cdot Z_f} \cdot \left[\frac{1}{f} \cdot (e^{f \cdot (Z_f - Z_t)} - 1) - (Z_f - Z_t) \right] \tag{B.14}$$

APPENDIX C: DERIVATION OF THE LIMITS OF POTENTIAL GRADIENTS AND LATERAL DISCHARGE

In this Appendix we derive the limits of the potential gradients in the vertical and horizontal directions, $J_z(z)$ and $J_h(z)$, and in the direction of flow, $J_s(z)$. We also derive the limit for the lateral discharge, Q_{out}.

The equations for $\alpha'(z)$ and $J_z(z)$ and $J_h(z)$ were given in Equations (2.25), (2.32) and (2.30), respectively. Here we write these three equations for $z=Z_t$, i. e. for the top of the zone of perched saturation.

$$\alpha'(Z_t) = \tan^{-1}[e^{f \cdot (Z_f - Z_t)} \cdot \tan(\alpha)] - \alpha \tag{C.1}$$

$$J_z(Z_t) = \frac{\tan(\alpha)}{\tan(\alpha) + \tan(\alpha'(Z_t))} \tag{C.2}$$

$$J_h(Z_t) = (1 - J_z(z)) \cdot \tan(\alpha) \tag{C.}$$

Under a constant rainfall rate R, Z_t decreases as Z_f increases with time, and Z_t will eventually reach the soil surface. As the difference $(Z_f - Z_t)$ increases, angle $\alpha'(Z_t)$ increases. For very large f and $(Z_f - Z_t)$, Equation (C.1) approaches $(90^\circ - \alpha)$, i. e. flow is nearly parallel to the terrain surface.

$$f \cdot (Z_f - Z_t) \to \infty; \qquad \alpha'(Z_t) \to (90^\circ - \alpha) \tag{C.4}$$

From trigonometry, we have that

$$\tan(90^{\circ} - \alpha) = \frac{1}{\tan(\alpha)}$$

<div align="right">(C.5)</div>

Using (C.4) and (C.5), (C.2) becomes,

$$J_z(Z_t) \rightarrow \frac{\tan(\alpha)}{\tan(\alpha) + \dfrac{1}{\tan(\alpha)}}$$

Multiplying numerator and denominator by $\tan(\alpha)$ and upon simplification we obtain,

$$f \cdot (Z_f - Z_t) \rightarrow \infty; \qquad J_z(Z_t) \rightarrow \sin^2(\alpha)$$

<div align="right">(C.6)</div>

Substituting (C.6) in (C.3) and upon simplification we obtain,

$$f \cdot (Z_f - Z_t) \rightarrow \infty; \qquad J_h(Z_t) \rightarrow \cos(\alpha) \cdot \sin(\alpha)$$

<div align="right">(C.7)</div>

For $J_s(Z_t)$ we have, from geometrical considerations,

$$J_s(Z_t) = \sqrt{J_h(Z_t)^2 + J_z(Z_t)^2}$$

<div align="right">(C.8)</div>

Substituting (C.6) and (C.7) in (C.8) we obtain,

$$f \cdot (Z_f - Z_t) \rightarrow \infty; \qquad J_s(Z_t) \rightarrow \sqrt{\sin^4(\alpha) + \cos^2(\alpha) \cdot \sin^2(\alpha)}$$

which upon simplification becomes,

<div align="center">212</div>

$$f \cdot (Z_f - Z_t) \to \infty; \qquad J_s(Z_t) \to \sin(\alpha) \qquad\qquad\qquad (C.9)$$

The lateral subsurface discharge (for an isotropic soil) was given in Equation (58), repeated here as (C.10),

$$Q_{out} = W \cdot K_0 \cdot \cos(\alpha) \cdot \sin(\alpha) \cdot e^{-f \cdot Z_f} \cdot \left[\frac{1}{f} \cdot (e^{f \cdot (Z_f - Z_t)} - 1) - (Z_f - Z_t) \right] \qquad (C.10)$$

Equation (C.10) can be written as,

$$Q_{out} = W \cdot K_0 \cdot \cos(\alpha) \cdot \sin(\alpha) \cdot \left[\frac{1}{f} \cdot (e^{-f \cdot Z_t} - e^{-f \cdot Z_f}) - \cdot e^{-f \cdot Z_f} \cdot (Z_f - Z_t) \right] \qquad (C.11)$$

For large Z_f and small Z_t, Equation (C.11) tends to,

$$Z_f \to \infty, Z_t \to 0 ; \qquad Q_{out} \to W \cdot \frac{K_0}{f} \cdot \cos(\alpha) \cdot \sin(\alpha) \qquad\qquad (C.12)$$

We saw in Section III.D that total transmissivity is approximated by K_0/f for large soil depths. Equation (C.7) gives the limit for the lateral hydraulic gradient to be $(\cos(\alpha) \cdot \sin(\alpha))$. Therefore, Equation (C.12) equals the limit of the product of total transmissivity and lateral gradient, multiplied by the width of flow, W.

```
C------------------------------------------------------------------C
C                        PROGRAM "kin.f"                           C
C------------------------------------------------------------------C

C------------------------------------------------------------------C
C                   VARIABLES AND PARAMETERS                       C
C------------------------------------------------------------------C

      PARAMETER(DX=400., DY=400., NROW=92, NCOL=114, N=3, NW=3,
     &      NCLASS=17, iIN=10, iRAIN=11, iORDER=12, iHYDRO=13,
     &      iDIR=14, iDISTS=15, iDISTG=16, iSLOPE=17, iGAGE=18,
     &      iSC=19)
      REAL CLASS(NROW,NCOL), ZWTm(NROW,NCOL), SLOPE(NROW,NCOL),
     &      ZF(NROW,NCOL), ZT(NROW,NCOL), NSTOm(NROW,NCOL),
     &      RQINm(NROW,NCOL), TIMEG(NROW,NCOL), HYDRO(240),
     &      K0dat(NCLASS), THSdat(NCLASS), THRdat(NCLASS), Edat(NCLASS),
     &      Y(N), YT(N), V(NW), WK(87), SS(NW), LENGTH(8), WIDTH(8),
     &      E, F, RR, Ri, RRF, RAINRATE, RQIN, QOUT
     &      HR, HI, HRF, AHR, AHRF, NSTO, NSTOold,
     &      T, DT, STEP, RAINSTEP, TEND, Told, K, S, W, WXY,
     &      ERROR, HMIN, TOL
      INTEGER DISTS(NROW,NCOL), DISTG(NROW,NCOL), DIR(NROW,NCOL),
     &      GAGE(NROW,NCOL), PI(8), PJ(8), IND, IER, ORDER, SC
      CHARACTER*80 DIRfile, SLOPEfile, DISTSfile, DISTGfile,
     &      SCfile, ORDERfile, GAGEfile, RAINfile, HYDROfile,
     &      ZWTfile, HEADER
      COMMON/REAL/RAIN(20), nGAGE, K0, F, E, THS, THR, Ri, RR,
     &      NSTOold, W, S, RQIN, T0, RAINRATE, iTYPE1, ZWT, TRIGO
      EXTERNAL MAINFCN, ReFCN, THFCN, RAINFCN
      DATA PI/0,1,1,1,0,-1,-1,-1/
      DATA PJ/-1,-1,0,1,1,1,0,-1/
      DATA K0dat/ 21.5 , 3.6 , 0.25 , 0.25 , 45. , 25.5 , 3.6 , 5.1 ,
     &      16.6 , 21.8 , 20.6 , 20.6 , 20.6 , 20.6 , 21.8 , 21.8 , 40./
      DATA THSdat/ 0.53 , 0.52 , 0.48 , 0.48 , 0.56 , 0.56 , 0.53 ,
     &      0.49 , 0.52 , 0.48 , 0.52 , 0.52 , 0.52 , 0.50 ,
     &      0.49 , 0.48 , 0.25 /
      DATA THRdat/ 0.02 , 0.036 , 0.09 , 0.09 , 0.109 , 0.09 , 0.109 ,
     &      0.109 , 0.064 , 0.036 , 0.072 , 0.072 , 0.072 , 0.07 ,
     &      0.03 , 0.041 , 0.02 /
      DATA Edat/ 3.6 , 3.6 , 7.5 , 7.5 , 3.6 , 7.5 , 3.6 , 3.6 , 3.5 ,
     &      3.4 , 3.6 , 3.6 , 3.6 , 3.6 , 3.5 , 3.6 , 3.4 /

C------------------------------------------------------------------C
C                        READ INPUT                               C
C------------------------------------------------------------------C

      OPEN(UNIT=iIN,FILE='kin.in',STATUS='OLD')
      READ(iIN,10)SCfile, DIRfile, SLOPEfile, DISTSfile, DISTGfile,
     &      ORDERfile, GAGEfile, RAINfile, ZWTfile, HYDROfile
10    FORMAT(9(A80/)A80)
      READ(iIN,*)F, Ri, Vo, Vs, iTYPE, nGAGE, RAINRATE, STEP,
     &           RAINSTEP, HMIN, TOL, TEND
      CLOSE(iIN)
      iTYPE1 = iTYPE

      OPEN(UNIT=iSC,FILE=SCfile,STATUS='OLD',READONLY)
      OPEN(UNIT=iDIR,FILE=DIRfile,STATUS='OLD',READONLY)
      OPEN(UNIT=iDISTS,FILE=DISTSfile,STATUS='OLD',READONLY)
      OPEN(UNIT=iDISTG,FILE=DISTGfile,STATUS='OLD',READONLY)
      OPEN(UNIT=iSLOPE,FILE=SLOPEfile,STATUS='OLD',READONLY)
      OPEN(UNIT=iZWT,FILE=ZWTfile,STATUS='OLD',READONLY)

      READ(iSC,20)HEADER
      READ(iDIR,20)HEADER
      READ(iDISTS,20)HEADER
      READ(iDISTG,20)HEADER
```

214

```
           READ(iSLOPE,20)HEADER
           READ(iZWT,20)HEADER
 20        FORMAT(A80)
           DO 30 I=1,NROW
              READ(iSC,*)(CLASS(I,J),J=1,NCOL)
              READ(iDIR,*)(DIR(I,J),J=1,NCOL)
              READ(iDISTS,*)(DISTS(I,J),J=1,NCOL)
              READ(iDISTG,*)(DISTG(I,J),J=1,NCOL)
              READ(iSLOPE,*)(SLOPE(I,J),J=1,NCOL)
              READ(iZWT,*)(ZWTm(I,J),J=1,NCOL)
 30        CONTINUE

           CLOSE(iSC)
           CLOSE(iDIR)
           CLOSE(iDISTS)
           CLOSE(iDISTG)
           CLOSE(iSLOPE)
           CLOSE(iZWT)

C----------------------------------------------------------------------C
C                      PRELIMINARY COMPUTATIONS                        C
C----------------------------------------------------------------------C


C----------------
C WIDTH OF FLOW
C----------------

           WXY = (DX*DY) / SQRT(DX**2+DY**2)
           WIDTH(1)=DY
           WIDTH(2)=WXY
           WIDTH(3)=DX
           WIDTH(4)=WXY
           WIDTH(5)=DY
           WIDTH(6)=WXY
           WIDTH(7)=DX
           WIDTH(8)=WXY
           DLXY = SQRT(DX**2+DY**2)
           LENGTH(1)=DX
           LENGTH(2)=DLXY
           LENGTH(3)=DY
           LENGTH(4)=DLXY
           LENGTH(5)=DX
           LENGTH(6)=DLXY
           LENGTH(7)=DY
           LENGTH(8)=DLXY

C-------------------------------
C TIME OF TRAVEL TO STREAMGAGE
C-------------------------------

           DO 40 I=1,NROW
           DO 40 J=1,NCOL
 40          TIMEG(I,J) = float(DISTS(I,J))/Vo + float(DISTG(I,J))/Vs

C----------------------------------------------------------------------C
C                       OPEN INPUT FILES                               C
C----------------------------------------------------------------------C

           IF(iTYPE.EQ.2)THEN
             OPEN(UNIT=iGAGE,FILE=GAGEfile,STATUS='OLD',READONLY)
             READ(iGAGE,*)NX, NY, DDX, DDY
             DO 50 I=1,NROW
             READ(iGAGE,*)(GAGE(I,J),J=1,NCOL)
 50          CONTINUE
             CLOSE(iGAGE)
```

```
        OPEN(UNIT=iRAIN,FILE=RAINfile,STATUS='OLD',READONLY)
      ENDIF

C-----------------------------------------------------------------C
C                         TIME LOOP (9999)                        C
C-----------------------------------------------------------------C

      nSTEPS = INT(TEND/STEP)

      DO 9999 iT = 1,nSTEPS
      T0 = (iT-1)*STEP

      IF(ABS(INT(T0/RAINSTEP)-T0/RAINSTEP).LT.1E-3)THEN
      CALL RAINFCN(iTYPE)
      ENDIF

C-----------------------------------------------------------------C
C                   HILLSLOPE PIXELS LOOP (8888)                  C
C-----------------------------------------------------------------C

      OPEN(UNIT=iORDER,FILE=ORDERfile,STATUS='OLD')
      READ(iORDER,*)nHPIXELS,nSPIXELS
      nPIXELS = nHPIXELS+nSPIXELS

      DO 8888 IP=1,nHPIXELS
      READ(iORDER,*)I,J

      IF(iTYPE.EQ.2)RR = AMAX1(RAIN(GAGE(I,J)),Ri)

C---------------------
C INITIALIZE VARIABLES
C---------------------

      Y(1)  = ZF(I,J)
      Y(2)  = ZT(I,J)
      Y(3)  = 0.
      SS(1) = Y(1)
      SS(2) = Y(2)
      SS(3) = Y(3)
      SC = CLASS(I,J)
      K0 = K0dat(SC)
      THS = THSdat(SC)
      THR = THRdat(SC)
      E = Edat(SC)
      S = SLOPE(I,J)
      W = WIDTH(DIR(I,J))
      ZWT = ZWTm(I,J)
      NSTOold = NSTOm(I,J)
      RQIN = RQINm(I,J)
      T = T0
      DT = STEP
      alfa = ATAND(S)
      TRIGO = SIND(alfa)*COSD(alfa)

C------------------
C UPDATE VARIABLES
C------------------

      IF(ZWT.EQ.0.)THEN
      T = T0+STEP
      HR = RR*STEP
      HRF = HR
      AHR = AHR + HR/nPIXELS
      AHRF = AHRF + HR/nPIXELS
      VRF = HRF*(DX*DY)/1000.
      iHOUR = MAX(NINT(T0+(STEP/2)+TIMEG(I,J)),1)
```

216

```
       HYDRO(iHOUR) = HYDRO(iHOUR) + VRF / 3600.
        GOTO 60
       ENDIF

70     CONTINUE

       CALL DREBS(MAINFCN,Y,T,N,6,1,0,DT,HMIN,TOL,V,SS,WK,IER)

       IF(IER.NE.0)WRITE(*,*)'ERROR',  IER,(V(IV),IV=1,NW)
       IF(T.LT.(T0+STEP-HMIN))THEN
           DT = T0+STEP-T
           GOTO 70
       ENDIF

       Y(1)  = AMIN1(Y(1),ZWT)
       Y(2)  = AMIN1(Y(2),Y(1))
       Y(2)  = AMAX1(Y(2),0.)

       NSTO = AMIN1(  (NSTOold+(AMIN1(RR,K0)+RQIN-Ri)*STEP-Y(3)),
      &        ((THS-THR)*Y(1)-(Ri/K0)**(1/E)*(THS-THR)*(E/F)*
      &        (EXP(F/E*Y(1))-1.)))

       HI = NSTO - NSTOold + Y(3) + (Ri-RQIN)*STEP
       HR = RR*STEP
       HRF = HR - HI
       RRF = HRF/STEP
       RI = AMAX1(HI,0.)/STEP

       VRF = HRF*(DX*DY)/1000.
       AHRF = AHRF + HRF/nPIXELS
       AHR = AHR + HR/nPIXELS
       AHI = AHI + HI/nPIXELS

       iHOUR = MAX(NINT(T0+(STEP/2)+TIMEG(I,J)),1)
       HYDRO(iHOUR) = HYDRO(iHOUR) + VRF / 3600.

C---------------
C STORE RESULTS
C---------------

       ZF(I,J)  = Y(1)
       ZT(I,J)  = Y(2)
       NSTOm(I,J) = NSTO
       RQOUT = Y(3)/STEP

       ID = DIR(I,J)
       II = I - PI(ID)
       JJ = J - PJ(ID)
       RQINm(II,JJ) = RQINm(II,JJ) + RQOUT

60     CONTINUE

       RQINm(I,J) = 0.

C--------------------------------8888----------------------------------C
8888   CONTINUE

C--------------------------------------------------------------------C
C                     STREAM PIXELS LOOP (7777)                       C
C--------------------------------------------------------------------C

       DO 7777 iSP = 1,nSPIXELS
       READ(iORDER,*)I,J

       IF(iTYPE.EQ.2)RR = RAIN(GAGE(I,J))
```

```
C-----------------------
C INITIALIZE VARIABLES
C-----------------------

        RQIN = RQINm(I,J)
        T = T0

C------------------
C UPDATE VARIABLES
C------------------

        HR  = RR*STEP
        RRF = RR + RQIN
        HRF = RRF * STEP
        VRF = HRF*(DX*DY)/1000.
        AHR = AHR + HR/nPIXELS
        AHRF = AHRF + HRF/nPIXELS

        iHOUR = MAX(NINT(T0+(STEP/2)+TIMEG(I,J)),1)
        HYDRO(iHOUR) = HYDRO(iHOUR) + VRF / 3600.

        RQINm(I,J) = 0

C---------------------------------7777------------------------------------C
7777    CONTINUE

        CLOSE(iORDER)

C---------------------------------9999------------------------------------C
9999    CONTINUE

        CLOSE(iRAIN)

C------------------------------------------------------------------------C
C                              WRITE RESULTS                              C
C------------------------------------------------------------------------C

        OPEN(UNIT=iHYDRO,FILE=HYDROfile,STATUS='NEW')
        WRITE(iHYDRO,*)'END TIME [hr] =',T
        WRITE(iHYDRO,*)'CUM RAIN [mm]=',AHR,' CUM INFILT [mm]=',AHI,
     &  ' CUM RUNOFF [mm]=',AHRF
        do 80 iT=1,T0+24
80      WRITE(iHYDRO,90)iT*RAINSTEP, HYDRO(iT)
90      FORMAT(I4,F9.2)

        CLOSE(iHYDRO)

      END

C------------------------------------------------------------------------C
C                         SUBROUTINE "MAINFCN"                           C
C------------------------------------------------------------------------C

      SUBROUTINE MAINFCN(N,T,Y,YT)
      PARAMETER(DX=400., DY=400.)
      REAL Y(N), YT(N)
      REAL K0, F, E, THS, THR, Ri, RR, RRF, TOL, HMIN,
     &     T, STEP, TEND, HI, NSTOold, AHR, HU, HS,
     &     T0, AHRF, HRF,
     &     W, S , V
      COMMON/REAL/RAIN(20), nGAGE, K0, F, E, THS, THR, Ri, RR,
     &     NSTOold, W, S, RQIN, T0, RAINRATE, iTYPE1, ZWT, TRIGO

      Re = ReFCN(Y(1),Y(2),Y(3),T)
      THi = THFCN(Ri,Y(1))
      TH1 = THFCN(Re,Y(1))
```

218

```fortran
      TH2 = THFCN(Re,Y(2))
      Ks = K0*EXP(-F*Y(1))
```

```
C-------------------
C SATURATION-EXCESS
C-------------------
      IF(Y(1).GE.ZWT)THEN
      YT(1) = 0.
      YT(2) = - Re / (THS-TH2)
      ELSE
C-------------------
C UNSATURATED FRONT
C-------------------
      IF((Y(1)-Y(2)).LT.1E-3.AND.Ks.GT.Re)THEN
       YT(1) = (Re-Ri) / (TH1-THi)
       YT(2) = YT(1)
      ELSE
C-------------------
C SATURATED FRONT
C-------------------
       YT(1) = (Ks-Ri) / (THS-THi)
       IF(THS-TH2.GT.1E-3)THEN
       YT(2) = ( Ks + RLS - Re ) / (THS-TH2)
       ELSE
          IF(Ks.GT.Re)THEN
          SIGN = 1.
          ELSE
          SIGN = -1.
          ENDIF
        YT(2) = SIGN * E/(THS-THR) * Re
       ENDIF

      ENDIF

      ENDIF

      YT(3) =  K0*TRIGO*( (EXP(F*(Y(1) - AMAX1(Y(2),0))) - 1.)
     &          /F-Y(1)+AMAX1(Y(2),0.) )
     &      / (EXP(F*Y(1))*400000.)

      END
```

```
C----------------------------------------------------------------C
C                    FUNCTION "ReFCN"                            C
C----------------------------------------------------------------C

      REAL FUNCTION ReFCN(X1,X2,X3,X4)
C     X1:=Y(1)=ZF, X2=Y(2)=ZT, X3=Y(3)=QOUT, X4=T
      REAL X1,X2,X3,X4,
     &     K0,F,E,THS,THR,Ri,RR,RQIN,NSTOold,T0
      COMMON/REAL/RAIN(20), nGAGE, K0, F, E, THS, THR, Ri, RR,
     &     NSTOold, W, S, RQIN, T0, RAINRATE, iTYPE1, ZWT, TRIGO

      IF(iTYPE1.EQ.1)THEN
      ReFCN = RR
      ELSE

      IF((F/E*X2).LT.1E-4)THEN
      ReFCN = RR      ! good assumption if ZT is very small!
      ELSE

      ReFCN = K0*( ( NSTOold + (RR+RQIN)*(X4-T0) - X3
     &       + (Ri/K0)**(1/E)*(THS-THR)*(E/F)*(EXP(F/E*X1)-1.)
     &       - (THS-THR)*(X1-X2) ) /
     &       ( (THS-THR)*(E/F)*(EXP(F/E*X2)-1.) ) )**E

      ENDIF
```

219

```fortran
      ENDIF

      END

C------------------------------------------------------------------------C
C                                                                        C
C                          FUNCTION "THFCN"                              C
C------------------------------------------------------------------------C

      REAL FUNCTION THFCN(X1,X2)
C     X1=Re, X2=ZF or ZT
      REAL X1,X2,
     &      K0,F,E,THS,THR,Ri,RR,RQIN,NSTOold,T0
      COMMON/REAL/RAIN(20), nGAGE, K0, F, E, THS, THR, Ri, RR,
     &      NSTOold, W, S, RQIN, T0, RAINRATE, iTYPE1, ZWT, TRIGO

      THFCN = AMIN1( ( (X1/K0)**(1/E)*EXP(F/E*X2)*(THS-THR)+THR ),
     &                     THS )

      END

C------------------------------------------------------------------------C
C                                                                        C
C                        SUBROUTINE "RAINFCN"                            C
C------------------------------------------------------------------------C

      SUBROUTINE RAINFCN(iTYPE)
      COMMON/REAL/RAIN(20), nGAGE, K0, F, E, THS, THR, Ri, RR,
     &      NSTOold, W, S, RQIN, T0, RAINRATE, iTYPE1, ZWT, TRIGO

      GOTO(1,2)iTYPE

C-------------------
C UNIFORM RAINFALL
C-------------------
1     CONTINUE
      RR = RAINRATE
      RETURN
C--------------------
C OBSERVED RAINFALL
C--------------------
2     CONTINUE
      READ(11,*)(RAIN(iG),iG=1,nGAGE)
      RETURN

      END
```